J. Fluid Mech. (2013), *vol.* 725, *pp.* 611–663. © Cambridge University Press 2013
doi:10.1017/jfm.2013.197

Emulsion flow through a packed bed with multiple drop breakup

Alexander Z. Zinchenko† and Robert H. Davis

Department of Chemical and Biological Engineering, University of Colorado, Boulder, CO 80309-0424, USA

(Received 2 November 2012; revised 7 February 2013; accepted 12 April 2013; first published online 22 May 2013)

Pressure-driven squeezing of a concentrated emulsion of deformable drops through a randomly packed granular material is studied by rigorous three-dimensional multidrop–multiparticle simulations at low Reynolds numbers. The drops are comparable in size with granular particles, so the drop phase and the carrier fluid have different permeabilities, and the emulsion cannot be treated as single phase. Squeezing requires significant drop deformation and can meet much resistance, depending on the capillary number $\boldsymbol{Ca}$. The granular material is modelled as a random loose packing (RLP) of many highly-frictional rigid monodisperse spheres in a periodic cell in mechanical equilibrium. Flow simulations for many drops squeezing through the network of solid spheres are performed by an extension of the multipole-accelerated boundary-integral (BI) algorithm of Zinchenko & Davis (*J. Comput. Phys.*, vol. 227, 2008, pp. 7841–7888). A major improvement is robust mesh control on drop surfaces combined with a novel fragmentation algorithm, now allowing for long-time simulations with intricate drop shapes and multiple breakups. A major challenge is that up to $O(10^5)$ time steps are required in a simulation for time averaging, and $O(10^4)$ boundary elements per surface to sufficiently resolve lubrication and breakups. Such simulations are feasible due to multipole acceleration, with two orders-of-magnitude gain over the standard BI coding. For initial drop-to-particle size ratio 0.51–0.52, emulsion concentration 41–42 % in the available space, and matching viscosities, time- and ensemble-averaged permeabilities of the drop phase and the continuous phase are studied versus $\boldsymbol{Ca}$ for systems of different size (up to 36 particles and 100 drops in a periodic cell). An avalanche of drop breakups observed at sufficiently large $\boldsymbol{Ca}$ does not preclude the permeabilities from reaching a statistical steady state in a feasible simulation time. The critical, system-size-independent $\boldsymbol{Ca}$, when the drop-phase flow effectively stops due to blockage in the pores by capillary forces, is estimated from simulations. For a sample RLP configuration, deep distinctions are found between the flow of concentrated emulsions and single-drop motion.

Key words: drops and bubbles, emulsions, porous media

1. Introduction

Flow of concentrated emulsions of deformable drops through a porous medium is relevant to many processes in nature and engineering, in particular oil filtration

† Email address for correspondence: alexander.zinchenko@colorado.edu

https://doi.org/10.1017/jfm.2013.197 Published online by Cambridge University Press

through underground reservoirs and crude recovery. When drops are smaller than the pores, the emulsion can be treated as single phase with complex rheology, and of basic interest is the flow rate–pressure gradient relationship, which no longer obeys the classical linear Darcy law. The task of formulating a suitable constitutive equation for the emulsion is highly non-trivial, though a number of simplified approaches have been offered (e.g. Chhabra & Srinivas 1991; Zhu & Satish 1992; Jaiswal, Sundararajan & Chhabra 1993; Kozicki 2001). Moreover, in practice the emulsion drops are often larger (in non-deformed state) than the pores, which invalidates the single-phase description; one should deal, instead, with two distinct velocities for the drop phase and the continuous phase. At sufficiently small pressure gradients, the drop phase is trapped in the pore throats by capillary forces; larger gradients result in multiple drop breakups. Fundamental understanding of these very complex processes is impossible without rigorous microstructural modelling. As a prototype model, Graham & Higdon (2000*a*,*b*) considered tight squeezing of a single deformable drop through a round capillary constriction (with periodic replication). Unlike in prior work, these authors were able to address the near-contact drop–wall interaction and estimate the critical forcing level for squeezing through the full Navier–Stokes finite-element solution. Their results also indicate that the inertial effects do not manifest themselves in the squeezing process until the Reynolds number on the pore scale is relatively large; Stokes flow is therefore a good approximation in a broad range of conditions for emulsion flow through a porous medium. Motivated by strong interest from petroleum engineering, a simplified approach called network modelling (see Romero & Carvalho 2011 and references therein) remains popular. This approach seeks to incorporate the flow information from the single-constriction level into a large network of 'nodes' (pores) and connecting 'bonds' (pore throats), in order to predict macroscopic permeabilities from the flow balance equations at each node. This approach, though, is not based on fundamental analysis and meets challenges when one tries to match an idealized capillary network to tomographic images from real samples; it is unclear, for example, which parts of the pore space must be assigned to nodes and bonds. Even for single-phase flows through a porous body with well-defined microstructure, the solutions on a single-throat level cannot avoid arbitrary assumptions (see below). Network modelling has been least satisfactory for two- (and three-) phase flows, with quite *ad hoc* assumptions about conductances of individual phases through a throat (e.g. Piri & Blunt 2005). As a better alternative, Romero & Carvalho (2011) incorporated experimental results (Cobos, Carvalho & Alvarado 2009) on drop motion through a mildly constricted round capillary tube into network modelling; still, it is problematic to relate the aspect ratio (degree of constriction) of such tubes to the microstructure of real samples. In addition, if a drop is trapped in a realistic 3D constriction, the carrier fluid is still able to flow around the drop in the corners. This feature is lost in the round capillary model.

In the present work, we consider Stokes flow of a concentrated emulsion through a porous medium from first principles, by rigorous three-dimensional multidrop/multiparticle simulations. To make this task feasible, a particular, reasonably well-defined model of the porous material is assumed; namely, the material skeleton is a random packing of many monodisperse spherical particles in mechanical equilibrium under the action of compressive contact forces. Although this model is less relevant to flows through rock formations, it is quite realistic for filtration through sand packs and was preferred in experiments (Guillen, Carvalho & Alvarado 2012). It is well-known that a collection of balls having been poured into a large vessel normally produces an arrangement between the limits of random loose and random close packings (RCPs)

https://doi.org/10.1017/jfm.2013.197 Published online by Cambridge University Press

(Scott & Kilgour 1969; Onoda & Liniger 1990); the volume fraction and coordination number are mostly affected by the dry friction coefficient. Network modelling for packed beds (Thompson & Fogler 1997) associates pores with Delaunay tetrahedra, and throats with triangular faces between neighbouring tetrahedra (excluding the space portion taken by the solid phase). Owing to the finite aspect ratio of the constrictions, even the single-phase flow problem (no drops) cannot be well-formulated on a single-constriction level, and has to be treated in a rather *ad hoc* manner, assuming parallel flow in a throat with heuristic correction for the converging–diverging character of the constriction around it. In contrast to these uncertainties with network modelling, multipole methods are well-suited for precise treatment of single-phase Newtonian flow through an array of solid spheres. Sangani & Acrivos (1982) and Zick & Homsy (1982) considered flow through period lattices; Chapman & Higdon (1992) even included the case of substantial sphere overlap using multipole collocation. Ladd (1990) and Mo & Sangani (1994) computed permeability of random multiparticle systems (with periodic boundaries); the latter work included the case of densely packed solid spheres in mechanical equilibrium. The multipole tools from these studies later evolved into the hydrodynamical fast multipole method (FMM), allowing for much larger arrays of spheres to be considered, in this and other problems (Sangani & Mo 1996).

On the other hand, in the absence of solid particles, the free-space three-dimensional Stokes flows of many interacting deformable drops have been also extensively studied in more recent works. Loewenberg & Hinch (1996) and Loewenberg (1998) offered the first shear flow simulations with up to 12 drops (in a periodic cell) and up to 30 % drop volume fractions, using direct boundary-integral (BI) coding (with quadratic scaling both in the number N of drops and the number N_Δ of boundary elements per drop). The necessarily more complex, multipole-accelerated BI algorithm (Zinchenko & Davis 2000) and subsequent improvements have made possible systematic long-time shear-flow simulations with contrast viscosities, up to 55 % drop volume fraction, $N = 100$–200, $N_\Delta = 1000$–1500 and up to $\sim 10^4$ time steps to study viscometric functions of concentrated emulsions (Zinchenko & Davis 2002). This algorithm was also applied to extensively study the long-time Koch–Shaqfeh instability of sedimenting emulsions, with resolutions $N_\Delta \sim 1000$, and the number N of drops reaching 1200 for the homoviscous case (Zinchenko & Davis 2003). For finite Reynolds numbers, when the BI approach would not apply, multibubble interactions were addressed by the front-tracking method (Unverdi & Tryggvason 1992; Tryggvason *et al.* 2001; Seo, Lele & Tryggvason 2010). In confined geometries, also relevant is the general geometry Ewald-like method (Hernández-Ortiz, de Pablo & Graham 2007); in combination with immersed boundary techniques, it was recently used to study the Stokes flow of many elastic capsules between two parallel walls (Pranay, Henríquez-Rivera & Graham 2012). Recent lattice–Boltzmann (LB) simulations for many deformable red blood cells in shearing motion were also reported (Dupin *et al.* 2007; MacMeccan *et al.* 2009). The LB method may be technically simpler than other approaches. Judging by the benchmarks, though, in Dupin *et al.* (2007), the LB simulations therein at 30 % cell volume fraction with parallel coding still do not approach the efficiency of earlier, single-processor shear flow simulations for many drops (Zinchenko & Davis 2002).

Compared with purely multidrop simulations in free space (Zinchenko & Davis 2000, 2002, 2003), the problem of concentrated emulsion flow through a randomly packed bed presents a much greater challenge, when the emulsion drops are comparable in size with the bed particles (and, hence, much larger than the pore

https://doi.org/10.1017/jfm.2013.197 Published online by Cambridge University Press

throats). To the best of the authors' knowledge, no attempts have been made to address this problem by multidrop–multiparticle dynamical simulations prior to the work of (Zinchenko & Davis 2008*a*; hereafter referred to as paper I). The algorithm of paper I, much different from those for purely multidrop simulations, employs Hebeker's (1986) representation for solid–particle contribution, resulting in a well-behaved system of second-kind integral equations that is suitable even for tight squeezing. Special desingularizations (especially the high-order singularity subtraction in the solid-to-drop contribution) greatly reduce the numerical trend for surface overlapping; still, resolution requirements remain very high, $N_\Delta \geqslant O(10^4)$ elements per surface. In this class of applications, our multipole acceleration scheme, with two levels of mesh-node decomposition into 'patches' and the entire surfaces, has significant technical and conceptual advantages over the general FMM logic, as discussed in paper I. Still, the resolution requirements limit the dynamical simulations to systems of small-to-moderate size. A few examples in paper I demonstrated long-time emulsion squeezing through a dense random array of solid spheres, with $\sim 10^4$ time steps, 9–14 particles and 25–40 drops in a periodic cell; particles and drops together take 70 % of the entire space. However, limitations on the drop mesh control algorithm therein did not allow us to study drop breakup in this process. Nor could we simulate, for the same reason, tight squeezing conditions (requiring even longer runs, with $O(10^5)$ time steps, for time averaging) or estimate the critical forcing level for drop-phase squeezing to occur. Ensemble averaging over many realizations of the granular material (very important, as it turns out, for meaningful results) was not addressed at all in paper I. Nor was the effect of emulsion concentration on the squeezing process. For the special case of a periodic emulsion squeezing through a dense periodic lattice of spheres (one particle and one drop per periodic cell), the algorithm of paper I was applied to obtain many more results (Zinchenko & Davis 2008*b*); however, such a geometry is restrictive.

In the present work, we seek to remove these limitations through significant code improvements and much more systematic simulations. In § 2.1, the BI formulation is briefly discussed. The present work is for matching viscosities ($\lambda = 1$) only, to expedite the runs several fold (but BI iterations are still required at each time step). However, the drop/particle systems herein are up to four times larger than the $\lambda = 4$ system in paper I. Other basic features of the algorithm (surface discretization and BI desingularizations, multipole acceleration and economical truncation of multipole expansions) are also outlined in § 2. Improvements include a new robust integration scheme over a solid sphere with unstructured triangulation (§ 2.2 and appendix A) to speed up convergence for the continuous-phase velocity, and an accelerated scheme (§ 2.2) for crucial high-order, near-singularity subtraction in the solid-to-drop contributions.

The drop-surface mesh control scheme in § 3, a major improvement over paper I, is a combination of: (i) 'passive mesh stabilization' (used in various forms in our prior multidrop work); (ii) active node redistribution through minimization of the mesh 'potential energy' (Cristini, Bławzdziewicz & Loewenberg 2001); and (iii) mesh topology transformations (also used in the front-tracking method of Unverdi & Tryggvason (1992) and Tryggvason *et al.* (2001)). The combined power of methods (i) and (ii), with the new forms herein for the 'kinetic' and potential mesh energy functions, moderately adaptive to local curvature, limits (iii) to simple node reconnections. This mesh control was robust in all long-time simulations of the present work, including very intricate drop shapes observed near breakup.

An addition of the novel fragmentation algorithm (§ 4), another major improvement over paper I, allows simulations to be continued after each breakup. Our algorithm,

https://doi.org/10.1017/jfm.2013.197 Published online by Cambridge University Press

based on 'swelling', is entirely different from the mesh splicing developed by Cristini *et al.* (2001) for free-space drop breakup simulations in linear flows (where the drops are mostly stretched in one direction, compared with more complex, but also more compact shapes herein). Our approach provides flexible on-demand control of fragment resolutions, and was used for a total of several hundred primary and secondary breakups in the present runs.

Miscellaneous details of the methodology (§ 5) include improved control of surface overlapping, improved generalized minimal residual (GMRES) iterations, generation of particle configurations and initial drop positions inside the material. For particle arrangements, we use a new and simple random loose packing (RLP) algorithm (announced, but not described in paper I), corresponding to the limit of high interparticle friction; details are provided in appendix B. This algorithm is efficient for small-to-moderate systems only (which was sufficient for the present paper), but it has no arbitrary parameters and, upon extrapolation to infinite size, yields results in very good agreement with experiments of Onoda & Liniger (1990). The reference problem of single-phase flow through dense cubic arrays of spheres is also included in § 5, to test the improved scheme of integration over solid boundaries.

In § 6, we discuss the simulation results for emulsion flow through RLPs, with drop-to-particle size ratio about 0.5, and the emulsion concentration (in the available space) over 40 %. The analysis includes time- and ensemble-averaged drop-phase and continuous-phase velocities in a broad range of capillary numbers, estimation of the critical capillary number for squeezing to occur, the effects of surface discretization, initial conditions and the system size; the largest systems include 36 particles and (initially) 100 drops in a periodic cell. An intriguing effect of massive drop breakup is also explored.

In § 7, we simulate single-drop motion through a RLP at finite size ratios, to clarify deep distinctions between the flows of concentrated and dilute emulsions.

To study how resolution requirements in the flow simulations with strong drop–solid lubrication can be relaxed, Thomas, Esmaeeli & Tryggvason (2010) considered a model two-dimensional problem of a deformable drop sliding along an inclined wall in near-contact at finite Reynolds numbers. They have, indeed, shown that incorporating a semi-analytical model for the thin film into the front-tracking code greatly reduces the necessary resolution. It would be highly desirable to have a similar methodology incorporated into the present simulations. However, it would be a very non-trivial task not attempted here; one difficulty is the extremely complex character of the three-dimensional pore space.

No attempt has been made either to parallelize the present code, and the efficiency of parallelization is unclear. Owing to the absence of long-range correlations in the granular material and to periodic boundaries, it is highly unlikely that the present problem would require very large arrays of particles and drops. We have opted, instead, to perform a large number of runs as single core with 100 % efficiency, for medium-size systems with ensemble averaging. The fastest core used in the calculations was Intel i7 965 (3.2 GHz).

2. Multipole-accelerated BI algorithm

Consider a three-dimensional, pressure-driven flow of an emulsion of immiscible, deformable drops through a randomly packed granular material (figure 1). The material skeleton is modelled as an arrangement of $\widehat{N} \gg 1$ solid particles with surface centroids $\widehat{\boldsymbol{x}}_1^c, \ldots, \widehat{\boldsymbol{x}}_{\widehat{N}}^c$ in a periodic cell $[0, L)^3$ and triply periodic continuation into the whole

https://doi.org/10.1017/jfm.2013.197 Published online by Cambridge University Press

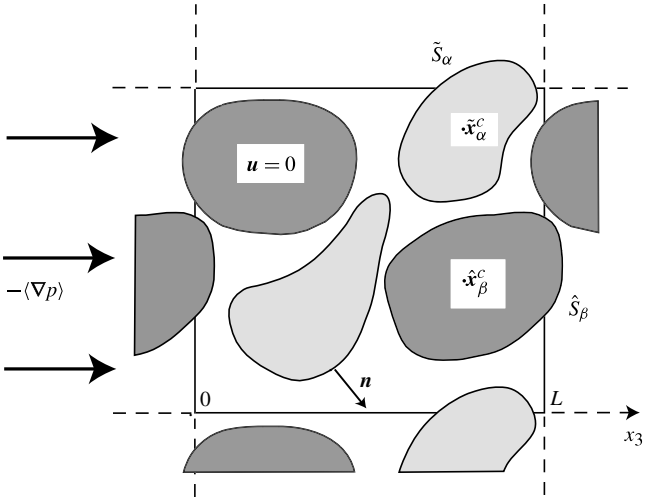


FIGURE 1. Schematic for the flow of deformable drops (light shading) through a random fixed array of solid particles (dark shading) in a periodic box $[0, L)^3$ under a pressure gradient, not to scale. In actual three-dimensional simulations, the solid particles are in mechanical equilibrium under the action of contact forces.

space. The particles are rigidly held in mechanical equilibrium under the action of realistic frictional contact forces; the RLP algorithm for preparing such particle arrangements is discussed in § 5. The drop phase is formed by $\widetilde{N} \gg 1$ deformable surfaces $\widetilde{S}_1, \ldots, \widetilde{S}_{\widetilde{N}}$ with centroids $\tilde{\boldsymbol{x}}^c_1, \ldots, \tilde{\boldsymbol{x}}^c_{\widetilde{N}} \in [0, L)^3$ and triply periodic continuation. The drops are Newtonian, free from surfactants, have a constant interfacial tension σ, and are freely suspended in a Newtonian continuous phase. As is typical in applications of emulsion flow through packed beds, the microscale Reynolds number is assumed small and so the Stokes equations apply. The multipole-accelerated BI algorithm of paper I developed and tested for this problem is for arbitrary drop-to-medium viscosity ratios $\lambda = \mu^{int}/\mu^e$. However, in the present work with many more systematic calculations, we have to make a simplifying assumption $\mu^{int} = \mu^e = \mu$, to expedite the runs several fold and facilitate long-time and ensemble averaging of the results.

As in paper I, the problem is solved in the constant pressure-gradient formulation. The local pressure is represented as $p(\boldsymbol{x}) = \langle\nabla p\rangle\cdot\boldsymbol{x}$ plus a triply periodic function, with a given average pressure gradient $\langle\nabla p\rangle$ over the entire space (regardless of how $p(\boldsymbol{x})$ is continued inside the solid phase). A convenient form of the average pressure-gradient condition is

$$\sum_{\beta=1}^{\widehat{N}} \boldsymbol{\mathcal{F}}_\beta = -\langle\nabla p\rangle V, \tag{2.1}$$

where the left-hand side is the total hydrodynamic force acting on the solid surfaces $\widehat{S}_1, \ldots, \widehat{S}_{\widehat{N}}$, and $V = L^3$ is the cell volume. Condition (2.1) makes the Stokes problem for each drop-particle configuration uniquely solvable. An alternative could be to solve the problem in the constant flow-rate formulation for the emulsion. However,

https://doi.org/10.1017/jfm.2013.197 Published online by Cambridge University Press

the form (2.1) is computationally much more efficient for $\lambda = 1$ (see below); the difference between the two formulations must disappear for large systems ($\widehat{N}$, $\widetilde{N} \gg 1$).

2.1. *BI formulation*

The BI formulation outlined below is the $\lambda = 1$ simplification of the equations from paper I. These equations are made non-dimensional using $|\langle \boldsymbol{\nabla} p \rangle| \widehat{a}^2/\mu$ and L as the velocity and length scales, respectively, where $\widehat{a}$ is the characteristic radius of solid particles. The direction of $\langle \boldsymbol{\nabla} p \rangle$ relative to Cartesian coordinate axes x_1, x_2, x_3 becomes insignificant for $\widehat{N}$, $\widetilde{N} \gg 1$; for simplicity, $\langle \boldsymbol{\nabla} p \rangle$ is assumed to be along the negative x_3-axis. The triply periodic fluid velocity $\boldsymbol{u}$ outside the particles and drops is represented as

$$\boldsymbol{u}(\boldsymbol{y}) = \boldsymbol{u}_o(\boldsymbol{y}) + \boldsymbol{C}, \tag{2.2}$$

where $\boldsymbol{C}$ is an additive constant (to be determined), and

$$\boldsymbol{u}_o(\boldsymbol{y}) = \boldsymbol{F}(\boldsymbol{y}) + \sum_{\beta=1}^{\widehat{N}} \int_{\widehat{S}_\beta} \boldsymbol{Q}(\boldsymbol{x}) \cdot [\eta \boldsymbol{G}(\boldsymbol{r}) + 2\breve{\boldsymbol{\tau}}(\boldsymbol{r}) \cdot \boldsymbol{n}(\boldsymbol{x})] \, \mathrm{d}S_x$$

$$+ \sum_{\beta=1}^{\widehat{N}} \int_{\widehat{S}_\beta} \boldsymbol{q}'(\boldsymbol{x}) \cdot [\eta \boldsymbol{G}(\boldsymbol{r}) + 2\breve{\boldsymbol{\tau}}(\boldsymbol{r}) \cdot \boldsymbol{n}(\boldsymbol{x})] \, \mathrm{d}S_x. \tag{2.3}$$

Here, the drop single-layer contribution is

$$\boldsymbol{F}(\boldsymbol{y}) = \frac{2\sigma}{|\langle \boldsymbol{\nabla} p \rangle| \widehat{a}^2} \sum_{\beta=1}^{\widetilde{N}} \int_{\widetilde{S}_\beta} k(\boldsymbol{x}) \boldsymbol{n}(\boldsymbol{x}) \cdot \boldsymbol{G}(\boldsymbol{r}) \, \mathrm{d}S_x, \tag{2.4}$$

$k(\boldsymbol{x}) = (k_1 + k_2)/2$ is the local mean of the principal curvatures k_1, k_2 at $\boldsymbol{x} \in \widetilde{S}_\beta$, $\boldsymbol{n}(\boldsymbol{x})$ is the unit outward normal to the drop surface, $\boldsymbol{r} = \boldsymbol{x} - \boldsymbol{y}$, and $\boldsymbol{G} = \{G_{ij}\}$ is Hasimoto's (1959) periodic Green tensor. This tensor $\boldsymbol{G}(\boldsymbol{r})$ is symmetric, has minimal unit periods along the coordinate axes x_1, x_2, x_3, and is singular at integer lattice points $\boldsymbol{m} = (m_1, m_2, m_3)$:

$$\boldsymbol{G}(\boldsymbol{r}) \simeq \boldsymbol{G}_o(\boldsymbol{r} - \boldsymbol{m}), \quad \boldsymbol{G}_o(\boldsymbol{r}) = -\frac{1}{8\pi} \left(\frac{\boldsymbol{I}}{r} + \frac{\boldsymbol{r}\boldsymbol{r}}{r^3} \right), \tag{2.5}$$

where $\boldsymbol{G}_o(\boldsymbol{r})$ is the standard free-space Stokeslet for a unit-viscosity fluid. Besides, it is essential for the present methodology to choose the additive constant in $\boldsymbol{G}$ so that the average of $\boldsymbol{G}$ over the periodic cell is zero. Other relevant properties of Hasimoto's tensor $\boldsymbol{G}$ are discussed in Zinchenko & Davis (2000) and in paper I.

The stress tensors $\boldsymbol{\tau}^{(k)}$ for Green vectors $\boldsymbol{G}^{(k)} = \{G_{k1}, G_{k2}, G_{k3}\}$ are not periodic, since they contain linearly growing parts from the pressures $\mathscr{P}^{(k)}$. Instead, we work with the periodic kernels

$$\breve{\boldsymbol{\tau}}^{(k)}(\boldsymbol{r}) = \boldsymbol{\tau}^{(k)}(\boldsymbol{r}) - r_k \boldsymbol{I}. \tag{2.6}$$

The third-rank tensor $\breve{\boldsymbol{\tau}} = \{\breve{\tau}_{ij}^{(k)}\}$ appearing in (2.3) is symmetric in all three indices, but has a non-zero divergence. Hebeker's (1986) approach (properly generalized for periodic boundary conditions) is used in our equation (2.3) to represent the solid-particle contribution (SPC) through a combination of single-layer and double-layer potentials, with a proportionality factor $\eta > 0$ (see below). On each solid surface $\widehat{S}_\beta$,

https://doi.org/10.1017/jfm.2013.197 Published online by Cambridge University Press

the Hebeker density $\boldsymbol{q}(\boldsymbol{x})$ is split as $\boldsymbol{q}'(\boldsymbol{x}) + \boldsymbol{Q}(\boldsymbol{x})$, where $\boldsymbol{q}'(\boldsymbol{x})$ is the projection of $\boldsymbol{q}(\boldsymbol{x})$ on the space of rigid-body motions, thus giving rise to two sets of boundary integrals in (2.3); this splitting greatly improves computational efficiency (see below). Flow representations (2.2)–(2.3) and no-slip boundary conditions $\boldsymbol{u} = \boldsymbol{0}$ on solid boundaries yield a system of second-kind integral equations for the Hebeker density $\boldsymbol{q}(\boldsymbol{x})$:

$$\boldsymbol{q}(\boldsymbol{y}) = (\boldsymbol{u}_o)_S(\boldsymbol{y}) + \boldsymbol{C}, \quad \boldsymbol{y} \in \widehat{S}_\alpha, \tag{2.7}$$

where the subscript S denotes direct values on the surface. The force balance (2.1) is recast in the form

$$\eta \sum_{\beta=1}^{\widehat{N}} \int_{\widehat{S}_\beta} \boldsymbol{q}(\boldsymbol{x})\, \mathrm{d}S = \left(\frac{L}{\widehat{a}}\right)^2 \boldsymbol{e}_3. \tag{2.8}$$

Substituting (2.7) into (2.8) allows us to express the constant $\boldsymbol{C}$ through the Hebeker density $\boldsymbol{q}(\boldsymbol{x})$, and formulate (2.7) and (2.8) as a system $\boldsymbol{q} = \boldsymbol{A}\boldsymbol{q} + \boldsymbol{B}$ to be solved iteratively for $\boldsymbol{q}$ only on the solid boundaries $\widehat{S}_\alpha$. The drop contribution term (2.4) only needs to be calculated (for all $\boldsymbol{y} \in \widehat{S}_\alpha$, $\widetilde{S}_\beta$) before the iterations. Once the solution $\boldsymbol{q}(\boldsymbol{x})$ is obtained on $\widehat{S}_\alpha$, solid-to-drop BI contributions are added to $\boldsymbol{F}(\boldsymbol{y})$ to calculate the interfacial velocity $\boldsymbol{u}(\boldsymbol{y})$ on the drop surfaces, according to (2.2) and (2.3).

For purely (multi)drop systems, without solid boundaries, the homoviscous case $\lambda = 1$ is known to greatly simplify the solutions, since the interfacial velocity in this case is explicitly given by a boundary integral over all drop surfaces, without iterations. In the present problem with a mixture of particles and drops, iterative solutions on solid boundaries cannot be avoided. However, $\lambda = 1$ still simplifies the problem, in that drop–solid BI interactions are taken out of iterations (such simplification would not be possible in the constant flow-rate formulation). In the present work with $\widetilde{N} > 2.77\widehat{N}$, the advantage over the general case $\lambda \neq 1$ (considered in paper I) is, at least, several fold, and has allowed for many more systematic calculations.

The main quantities of interest from the solution are the non-dimensional instantaneous drop phase ($\boldsymbol{U}_D$) and continuous phase ($\boldsymbol{U}_C$) velocities (with subsequent time averaging). These velocities are defined as volume averages of the fluid velocity $\boldsymbol{u}$ over the drop and continuous phases, respectively. Calculation of $\boldsymbol{U}_D$ is immediately reduced to surface integrals over $\widetilde{S}_\alpha$ through the Gauss theorem,

$$\boldsymbol{U}_D = \frac{1}{c_d} \sum_{\alpha=1}^{\widetilde{N}} \int_{\widetilde{S}_\alpha} (\boldsymbol{u} \cdot \boldsymbol{n})(\boldsymbol{x} - \widetilde{\boldsymbol{x}}_\alpha^c)\, \mathrm{d}S, \tag{2.9}$$

where c_d is the drop volume fraction in the entire space. Less obvious, it was also shown in paper I how to reduce the calculation of $\boldsymbol{U}_C$ to surface integrals over the phase boundaries. With the chosen additive constant in the Green function $\boldsymbol{G}$ (see above), we have, for $\lambda = 1$,

$$\boldsymbol{U}_C = \boldsymbol{C} - \frac{1}{1 - c_s - c_d} \left\{ \sum_{\alpha=1}^{\widetilde{N}} \int_{\widetilde{S}_\alpha} (\boldsymbol{u}_o \cdot \boldsymbol{n})(\boldsymbol{x} - \widetilde{\boldsymbol{x}}_\alpha^c)\, \mathrm{d}S \right.$$
$$\left. + \sum_{\alpha=1}^{\widehat{N}} \int_{\widehat{S}_\alpha} \{[(\boldsymbol{u}_o)_S + \boldsymbol{q}] \cdot \boldsymbol{n}\}(\boldsymbol{x} - \widehat{\boldsymbol{x}}_\alpha^c)\, \mathrm{d}S \right\}, \tag{2.10}$$

with c_s being the solid volume fraction in the entire space.

https://doi.org/10.1017/jfm.2013.197 Published online by Cambridge University Press

The BI formulation (2.1)–(2.10) is suitable for solid particles of arbitrary shapes. In what follows, however, we assume spherical shapes of the same radius $\widehat{a}$. For such simple shapes (also including spheroids and three-dimensional ellipsoids), the splitting $\boldsymbol{q} = \boldsymbol{q}' + \boldsymbol{Q}$ of the Hebeker density is very beneficial at high solid volume fractions (typical of a packed granular material): due to low permeability, $\boldsymbol{q}(\boldsymbol{x})$ attains large values, and subtracting the rigid-body projection $\boldsymbol{q}'$ from $\boldsymbol{q}$ greatly reduces the numerical error in the integrals (the first line of (2.3)); the added-back terms with $\boldsymbol{q}'$ (the second line of (2.3)) allow the precise semi-analytical treatment (paper I).

For simulations with spherical particle shapes, it could be tempting to avoid particle meshing altogether and represent their contribution to the flow by multipoles, leaving BI representations and surface meshing for deformable drops only. In the absence of drops, such purely multipole solutions are well known for flows through periodic and random fixed beds of spheres in the whole range of volume fractions (Sangani & Acrivos 1982; Zick & Homsy 1982; Ladd 1990; Chapman & Higdon 1992; Mo & Sangani 1994), with superior rates of convergence. However, in the test problem for a single deformable drop squeezing through a tight free-space cluster of three spheres, we found (paper I) that a purely multipole representation for flow contribution from solid boundaries is far from a viable approach and does not succeed beyond the very initial stage of squeezing. Presumably, the BI approach, with singularity distributions over a surface and subsequent integral desingularizations (see the next subsection), provides a much better control of the local error than when the singularities are in particle centres. As in paper I, multipoles are used herein to dramatically accelerate the performance, but the BI is the starting point, with necessary meshing for both drops and particles.

Some benefits of the Hebeker representation and the choice of parameter $\eta > 0$ also merit discussion. A double-layer representation ($\eta = 0$) for the SPC could not accommodate non-zero hydrodynamical forces acting on solids. An alternative, single-layer representation for SPC yields ill-conditioned, first-kind integral equations and a poor three-dimensional algorithm not capable of proceeding beyond the initial stage of tight squeezing, as was observed in our tests (Zinchenko & Davis 2006) for a drop between three solid spheres. Although the results with the Hebeker representation are independent of $\eta > 0$ in the limit of fine surface discretizations, there is the optimal range of η for accuracy and convergence of iterations; $\eta = 3/\widehat{a}$ was fixed in the present work.

Another alternative to Hebeker representation for SPC could be using the double-layer potential complemented by Stokeslet and Rotlet contributions from the particle centres (Power & Miranda's 1987 representation). This technique was observed (Zinchenko & Davis 2006; paper I) to be less robust in tight squeezing problems than the Hebeker form, again, because the singularities (Stokeslet and Rotlet) are not distributed.

2.2. *Surface discretization and BI desingularizations*

For the drops (initially spherical in the sense that will be clarified in § 5) and solid particles, we use an unstructured mesh of surface triangles with vertices $\boldsymbol{x}^i$. Methods for unstructured, nearly uniform triangulations of a spherical surface are well known. We start either from a regular icosahedron (Kim & Karilla 1991) or triangulated dodecahedron (Zinchenko, Rother & Davis 1997) inscribed into the sphere, followed by recursive refinement of each face into m^2 smaller triangles (Loewenberg & Hinch 1996), with typically $m = 2$ and always $m \leqslant 5$ (to keep meshing nearly uniform). Each new mesh vertex once appearing in this process is radially projected onto

https://doi.org/10.1017/jfm.2013.197 Published online by Cambridge University Press

the sphere from the centre. In particular, this algorithm yields tessellations with $N_\Delta = 2160$, 3840, 5120, 6000, 8640, 11 520 or 15 360 triangular elements relevant to the present calculations. Initially, all drops (assumed monodisperse) are triangulated with the same number $\widetilde{N}_\Delta$ of elements per surface. As the drops move and deform, the mesh topology occasionally changes due to node reconnections, and the number of triangles may change due to drop breakup. Thus, in general, every drop surface $\widetilde{S}_\alpha$ has its own number of elements $\widetilde{N}_\Delta^\alpha$ at $t > 0$. The algorithms for drop mesh control in dynamical simulations and breakup, with moderate adaptation to local curvature, are discussed in §§ 3 and 4. In contrast, for solid particles, we use the initial, fixed non-adaptive meshes with the same number $\widehat{N}_\Delta$ of elements per surface throughout the whole simulation. No advantages of adaptive solid surface triangulations were found in paper I; obviously, for multidrop–multiparticle configurations in the present problem, it is difficult to have meshing well-adaptive to both near-contact areas between the solids, and lubrication areas between the solids and drops.

On the drop surfaces, all boundary integrals (after regularization, when necessary) are calculated by the simplest second-order trapezoidal rule, with reassignment of the triangle contributions to vertices (Rallison 1981)

$$\int_S \varphi(\boldsymbol{x})\,\mathrm{d}S \approx \sum_{\boldsymbol{x}^j \in S} \varphi(\boldsymbol{x}^j)\Delta S_j, \tag{2.11}$$

where ΔS_j is 1/3 of the sum of flat triangle areas sharing node $\boldsymbol{x}^j$. The economical rule (2.11) was used in much of prior BI work and is much preferable to more expensive high-order integrations for flows of concentrated emulsions (Zinchenko & Davis 2000, 2002, 2003; paper I; Zinchenko & Davis 2008*b*). In paper I, the same rule was used for integrals over the solid surfaces. In the present work, though, we use a vastly improved scheme of integration over solid boundaries with unstructured triangulation, considering the mesh triangles as curved and taking full advantage of the spherical shape. Namely, within each spherical mesh triangle Δ, based on the values of $\varphi(\boldsymbol{x}^i)$ in the triangle vertices, $\varphi(\boldsymbol{x})$ is approximated as a linear function of the local Cartesian coordinates x', y' in the tangential plane at the triangle centre; this linear form is then integrated exactly over the spherical triangle. The total integral over S can still be written in the economic form (2.11), although the calculation of the area elements ΔS_j is now more complex; details are given in appendix A. This integration rule is still $O(1/N_\Delta)$-accurate, but the numerical coefficient is typically an order-of-magnitude smaller than for the trapezoidal rule. Remarkably, the new integration rule has the same compact support, in that a triangle contribution depends on $\varphi(\boldsymbol{x})$ in its vertices only. We also extended this approach to high-order integration (appendix A), approximating $\varphi(\boldsymbol{x})$ as a quadratic function of x', y' within Δ (based on the values in the triangle vertices and three more mesh nodes around Δ). This quadrature, with superb accuracy for generic smooth integrands $\varphi(\boldsymbol{x})$, was however at a disadvantage in the present calculations (where the solution is not smooth enough), obviously because it is less local. In particular, the high-order integration (with formal $O(N_\Delta^{-2})$ convergence) greatly increases the numerical trend of drop–solid overlap and the dispersion of the results in long-time simulations for tight squeezing. The chosen integration scheme, with linear local approximation of the integrand, represents the balance between robustness and overall accuracy; its significant advantage over the simplest trapezoidal rule will be demonstrated in § 5.

For successful numerical solution, singular ($\boldsymbol{x} = \boldsymbol{y}$) and near-singular ($\boldsymbol{x} \approx \boldsymbol{y}$) behaviour of the integrands in (2.3)–(2.4) must be alleviated. The integrals for drop-to-

https://doi.org/10.1017/jfm.2013.197 Published online by Cambridge University Press

solid, drop-to-drop and solid-to-solid contributions are discretized as described in § 3 of paper I, with additional terms appearing due to (near) singularity subtraction. In the economical form of paper I, these terms contain 'barrier functions' and are in effect only for close interactions, with efficient point-to-point calculation. In the limit of fine triangulations, these additional terms disappear altogether, but they greatly accelerate the convergence.

In the absence of drop double-layer contributions (only relevant for $\lambda \neq 1$), the most important aspect of these desingularization techniques is the high-order, near-singularity subtraction in the solid-to-drop double-layer contribution employed in paper I and the present work. For each periodic image $\boldsymbol{y} - \boldsymbol{m}$ of a mesh node $\boldsymbol{y} \in \widetilde{S}_\alpha$ on a drop surface, we consider the mesh node $\boldsymbol{x}^{i^*}$ on a solid integration surface $\widehat{S}_\beta$ that is nearest to $\boldsymbol{y} - \boldsymbol{m}$, and construct a linear approximation

$$\boldsymbol{Q}(\boldsymbol{x}^{i^*}) + \sum_{j \in \mathscr{A}_i^*} [\boldsymbol{c}_{j,i^*} \cdot (\boldsymbol{x} - \boldsymbol{x}^{i^*})][\boldsymbol{Q}(\boldsymbol{x}^j) - \boldsymbol{Q}(\boldsymbol{x}^{i^*})] \tag{2.12}$$

to $\boldsymbol{Q}(\boldsymbol{x})$ near $\boldsymbol{x}^{i^*}$ on $\widehat{S}_\beta$. The vector coefficients $\boldsymbol{c}_{j,i}$ depend only on the mesh geometry near $\boldsymbol{x}^i$ and are given by Zinchenko & Davis (2006); the summation in (2.12) is over the set of mesh nodes $\boldsymbol{x}^j$ directly connected to $\boldsymbol{x}^{i^*}$. Accordingly, each integral (2.3) with $\boldsymbol{Q}(\boldsymbol{x})$ is approximated as (paper I)

$$\sum_{\boldsymbol{x}^j \in \widehat{S}_\beta} \boldsymbol{Q}(\boldsymbol{x}^j) \cdot [\eta \boldsymbol{G}(\boldsymbol{x}^j - \boldsymbol{y}) + 2\breve{\boldsymbol{\tau}}(\boldsymbol{x}^j - \boldsymbol{y}) \cdot \boldsymbol{n}(\boldsymbol{x}^j)] \Delta S_j + \sum_{\boldsymbol{m}} \Theta_3 \Big\{ \boldsymbol{Q}^* \cdot \boldsymbol{\Pi}(\boldsymbol{y} - \boldsymbol{m}, \beta)$$

$$+ \sum_{j \in \mathscr{A}_{i^*}} \boldsymbol{c}_{j,i^*} \cdot \boldsymbol{\Gamma}(\boldsymbol{y} - \boldsymbol{m}, \beta) \cdot [\boldsymbol{Q}(\boldsymbol{x}^j) - \boldsymbol{Q}(\boldsymbol{x}^{i^*})] \Big\} \tag{2.13}$$

(using new surface elements ΔS_j). Here,

$$\boldsymbol{Q}^* = \boldsymbol{Q}(\boldsymbol{x}^{i^*}) + \sum_{j \in \mathscr{A}_i^*} [\boldsymbol{c}_{j,i^*} \cdot (\boldsymbol{y} - \boldsymbol{m} - \boldsymbol{x}^{i^*})][\boldsymbol{Q}(\boldsymbol{x}^j) - \boldsymbol{Q}(\boldsymbol{x}^{i^*})] \tag{2.14}$$

is the interpolation of $\boldsymbol{Q}(\boldsymbol{x})$ to the point on the surface $\widehat{S}_\beta$ closest to $\boldsymbol{y} - \boldsymbol{m}$. The barrier function $\Theta_3(\alpha, \beta, \boldsymbol{m})$ is defined in paper I, with gradual transition from 1, when the drop surface $\widetilde{S}_\alpha$ nearly touches the periodic shift $\widehat{S}_\beta + \boldsymbol{m}$ of the integration surface $\widehat{S}_\beta$, to zero when the node-to-surface distance between $\widetilde{S}_\alpha$ and $\widehat{S}_\beta + \boldsymbol{m}$ exceeds $0.25\hat{a}$. The additional second- and third-rank tensors are

$$\boldsymbol{\Pi}(\boldsymbol{y}, \beta) = -\sum_{\boldsymbol{x}^j \in \widehat{S}_\beta} [\eta \boldsymbol{G}_o(\boldsymbol{r}^j) + 2\boldsymbol{\tau}_o(\boldsymbol{r}^j) \cdot \boldsymbol{n}(\boldsymbol{x}^j)] \Delta S_j + \eta \int_{\widehat{S}_\beta} \boldsymbol{G}_o(\boldsymbol{r})\, \mathrm{d}S_x \tag{2.15}$$

and

$$\boldsymbol{\Gamma}(\boldsymbol{y}, \beta) = \frac{3}{2\pi} \left[-\sum_{\boldsymbol{x}^j \in \widehat{S}_\beta} \frac{[\boldsymbol{r}^j \cdot \boldsymbol{n}(\boldsymbol{x}^j)] \boldsymbol{r}^j \boldsymbol{r}^j \boldsymbol{r}^j}{|\boldsymbol{r}^j|^5} \Delta S_j + \int_{\widehat{S}_\beta} \frac{[\boldsymbol{r} \cdot \boldsymbol{n}(\boldsymbol{x})] \boldsymbol{r}\boldsymbol{r}\boldsymbol{r}}{|\boldsymbol{r}|^5} \mathrm{d}S_x \right], \tag{2.16}$$

where $\boldsymbol{r}^j = \boldsymbol{x}^j - \boldsymbol{y}$, $\boldsymbol{r} = \boldsymbol{x} - \boldsymbol{y}$ and $\boldsymbol{\tau}_o(\boldsymbol{\xi}) = 3\boldsymbol{\xi}\boldsymbol{\xi}\boldsymbol{\xi}/(4\pi\xi^5)$ is the free-space stresslet; the added-back integrals in (2.15) and (2.16) are calculated analytically.

We have found absolutely necessary to retain both $\boldsymbol{\Pi}$ and $\boldsymbol{\Gamma}$ terms in the subtraction scheme (2.13), providing full desingularization of the integrand and greatly

https://doi.org/10.1017/jfm.2013.197 Published online by Cambridge University Press

reducing the numerical trend for drop–solid overlap. With $\boldsymbol{\Gamma} = \mathbf{0}$ (and $\boldsymbol{Q}^*$ provided by (2.14) or simply $\boldsymbol{Q}^* = \boldsymbol{Q}(\boldsymbol{x}^{i^*})$, as slightly different versions of the leading-order subtraction), our attempts of drop squeezing simulations could never succeed beyond the early stage, even when the artificial geometric barrier (§ 5) was imposed to prevent such overlapping. Namely, due to numerical errors in the lubrication areas, artificially high surface curvatures, with prohibitive time step limitations, and a large number of BI iterations were observed in this case. It should be noted, however, that the idea of the leading-order, near-singularity subtraction in the double-layer potential was successful in other, less-demanding emulsion flow simulations (Loewenberg & Hinch 1996; Loewenberg 1998; Zinchenko & Davis 2000).

The precalculation of tensors $\boldsymbol{\Pi}$ and (especially) $\boldsymbol{\Gamma}$ for all relevant combinations $\boldsymbol{y}$, $\boldsymbol{m}$, β (with $\Theta_3 \neq 0$), even though it is taken out of iterations, can be computationally expensive. To lessen this burden, paper I suggested: (i) using direct summations (2.15)–(2.16) only for $\boldsymbol{y} - \boldsymbol{m}$ in near-contact with the sphere $\widehat{S}_\beta$; (ii) using more economical multipole expansions for the discrete parts of $\boldsymbol{\Pi}$ and $\boldsymbol{\Gamma}$ in inverse powers of $\|\boldsymbol{y} - \boldsymbol{m} - \widehat{\boldsymbol{x}}_\beta^c\|$, when $\boldsymbol{y} - \boldsymbol{m}$ is well-separated from $\widehat{S}_\beta$; and (iii) interpolating $\boldsymbol{\Gamma}$ from an auxiliary table in the intermediate range of $\|\boldsymbol{y} - \boldsymbol{m} - \widehat{\boldsymbol{x}}_\beta^c\|/\widehat{a}$. Since all solid particles have identical meshes, to within translation, the same table is used for all $\widehat{S}_\beta$. However, even with these improvements, calculation of $\boldsymbol{\Pi}$ and $\boldsymbol{\Gamma}$ can take a substantial portion of the overall computational cost.

In the present work, a further significant acceleration of $\boldsymbol{\Pi}$- and $\boldsymbol{\Gamma}$-calculations is found, based on the symmetry properties of the solid particle meshing. Obviously, the central symmetry of a regular icosahedron (dodecahedron) about the centre $\widehat{\boldsymbol{x}}_\beta^c$ of the circumscribed sphere is inherited by all mesh refinement operations discussed earlier in this subsection, so for every mesh vertex $\boldsymbol{x}^j$ of the ultimate mesh on $\widehat{S}_\beta$ there is a centrally symmetric mesh vertex $2\widehat{\boldsymbol{x}}_\beta^c - \boldsymbol{x}^j$. As a consequence, only about half of the multipole coefficients for $\boldsymbol{\Pi}$ and $\boldsymbol{\Gamma}$ are non-zero, with two-fold gain in multipole-based calculation of these tensors. In pointwise computations of $\boldsymbol{\Pi}$ and $\boldsymbol{\Gamma}$ for $\boldsymbol{y} - \boldsymbol{m}$ near $\widehat{S}_\beta$, significant acceleration is also achieved by joining contributions from centrally symmetric nodes $\boldsymbol{x}^j$. After all optimizations, the relative cost of $\boldsymbol{\Pi}$- and $\boldsymbol{\Gamma}$-calculations in the whole solution of the BI problem is about 20 %, for typical drop-particle arrangements ($\widetilde{N} \approx 2.8\widehat{N}$), resolutions $\widetilde{N}_\Delta = 6000$, $\widehat{N}_\Delta = 8600$ and seven iterations on solid boundaries.

2.3. *Multipole acceleration of BI iterations*

It is most crucial to use a multipole-accelerated scheme for calculation of the first sum in (2.13), where now the observation mesh node $\boldsymbol{y}$ can be either on a solid surface (to iterate the Hebeker density $\boldsymbol{q}$) or on a drop surface (for post-iterative calculation of the interfacial velocity $\boldsymbol{u}$). The simplest point-to-point summation, with quadratic scaling in the total number of mesh nodes, would be far too prohibitive in dynamical simulations, since we have to work with $\widehat{N} + \widetilde{N} = O(10^2)$ surfaces and $O(10^4)$ triangular elements per surface. The present multipole acceleration scheme follows paper I, with some simplifications due to $\lambda = 1$, and is briefly outlined below for this specific case; the full description and comprehensive testing of this highly efficient, but lengthy scheme may be found in paper I.

Prior to dynamical simulation, the mesh nodes $\boldsymbol{x}^j$ on each solid surface $\widehat{S}_\beta$ are grouped into a large number $\widehat{M}_\Delta$ of compact non-overlapping sets $\mathscr{B}_\gamma$ called 'patches', of roughly a hexagonal or pentagonal shape; it is optimal to have 200–400 nodes $\boldsymbol{x}^j$

https://doi.org/10.1017/jfm.2013.197 Published online by Cambridge University Press

per patch. A minimal spherical shell $\mathscr{D}_\gamma$ with centre $\boldsymbol{x}^o_\gamma \in \widehat{S}_\beta$ and radius d^o_γ is constructed around each $\mathscr{B}_\gamma$ with sufficient accuracy. Minimal spherical shells $\mathscr{D}_\alpha$ with centres $\boldsymbol{x}^o_\alpha$ and radii d^o_α around the whole surfaces S_α (drop or solid) are also used in the algorithm; $\mathscr{D}_\alpha = \widehat{S}_\alpha$, $\boldsymbol{x}^o_\alpha = \widehat{\boldsymbol{x}}^c_\alpha$, and $d^o_\alpha = \widehat{a}$ for a sphere $\widehat{S}_\alpha$. To avoid confusion, symbols δ, γ are reserved for patches, while α, β are used for the entire drop and solid surfaces; in what follows, S_α stands for $\widetilde{S}_\alpha$ or $\widehat{S}_\alpha$.

The periodic Green function $\boldsymbol{G}$ and the corresponding stresslet $\breve{\boldsymbol{\tau}}$ are split into the 'far-field' ($\boldsymbol{G}_1$, $\boldsymbol{\tau}_1$) and 'near-field' parts:

$$\boldsymbol{G}(\boldsymbol{r}) = \sum_{|m_i|\leqslant 2} \boldsymbol{G}_o(\boldsymbol{r}+\boldsymbol{m}) + \boldsymbol{G}_1(\boldsymbol{r}), \quad \breve{\boldsymbol{\tau}}(\boldsymbol{r}) = \sum_{|m_i|\leqslant 2} \boldsymbol{\tau}_o(\boldsymbol{r}+\boldsymbol{m}) + \boldsymbol{\tau}_1(\boldsymbol{r}), \tag{2.17}$$

with integer vectors $\boldsymbol{m}$; the purpose of partition (2.17) is to move singularities of $\boldsymbol{G}_1$ and $\boldsymbol{\tau}_1$ far away from the origin. For drop/particle systems of larger size than those in the present calculations, it would be beneficial to include fewer free-space contributions $\boldsymbol{G}_o(\boldsymbol{r}+\boldsymbol{m})$, $\boldsymbol{\tau}_o(\boldsymbol{r}+\boldsymbol{m})$ into the near-field parts (Zinchenko & Davis 2000, 2002, 2003).

The free-space contribution of each patch $\mathscr{B}_\gamma$ to the summation (2.13) (i.e. with $\boldsymbol{\tau}_o(\boldsymbol{x}^j - \boldsymbol{y})$ in place of $\breve{\boldsymbol{\tau}}(\boldsymbol{x}^j - \boldsymbol{y})$) is expanded in Lamb's singular series about the patch centre $\boldsymbol{x}^o_\gamma$ using the special, most-economical algorithm of paper I for patches on a spherical surface. Lamb's singular series for the whole-surface contribution from $\widehat{S}_\beta$ to (2.13) is also constructed, by translating the patch expansions for all $\mathscr{B}_\gamma \in \widehat{S}_\beta$ to the sphere centre $\widehat{\boldsymbol{x}}^c_\beta$; this operation is greatly sped up by rotational transformations of spherical harmonics.

Now, to calculate the contribution of a single surface $\widehat{S}_\beta$ to the first sum (2.13) for $\boldsymbol{y} \in S_\alpha$, we consider instead a periodically shifted surface $\widehat{S}^{min}_\beta = \widehat{S}_\beta + \boldsymbol{m}_{\alpha\beta}$, which has the minimum centre-to-centre distance $\|\boldsymbol{x}^{o,min}_\beta - \boldsymbol{x}^o_\alpha\|$ (with $\boldsymbol{x}^{o,min}_\beta = \boldsymbol{x}^o_\beta + \boldsymbol{m}_{\alpha\beta}$) from S_α. In what follows, index *min* will supplement quantities related to $\widehat{S}^{min}_\beta$. According to (2.17) and periodicity of the kernels $\boldsymbol{G}$ and $\breve{\boldsymbol{\tau}}$, the contribution of surface $\widehat{S}_\beta$ to the first sum (2.13) can be written as the sum of 125 free-space contributions from $\widehat{S}^{min}_\beta + \boldsymbol{m}$ (with $|m_i| \leqslant 2$) plus the far-field contribution. The far-field part is calculated by a special form of Taylor double series for $\boldsymbol{\tau}_1(\boldsymbol{x}-\boldsymbol{y})$ and $\boldsymbol{G}_1(\boldsymbol{x}-\boldsymbol{y})$ in powers of $\boldsymbol{x} - \boldsymbol{x}^{o,min}_\beta$ and $\boldsymbol{y} - \boldsymbol{x}^o_\alpha$, based on a large, precalculated table for $\boldsymbol{G}_1(\boldsymbol{r})$, the related pressure $\mathscr{P}_1(\boldsymbol{r})$ and their high-order derivatives. Since the distance from the origin to the nearest singularities of $\boldsymbol{G}_1(\boldsymbol{r})$ and $\boldsymbol{\tau}_1(\boldsymbol{r})$ is much larger than the half-size of the periodic box, the Taylor double series are fast convergent, and just a few terms suffice.

If the shell $\mathscr{D}^{min}_\beta + \boldsymbol{m}$ around $\widehat{S}^{min}_\beta + \boldsymbol{m}$ and shell $\mathscr{D}_\alpha$ have 'enough clearance' (see below), the free-space contribution from $S^{min}_\beta + \boldsymbol{m}$ to (2.13) is evaluated at $\boldsymbol{y} \in S_\alpha$ by first re-expanding Lamb's singular series for the whole surface $\widehat{S}_\beta$ (see above) as Lamb's regular series near $\boldsymbol{x}^o_\alpha - \boldsymbol{m}_{\alpha\beta} - \boldsymbol{m}$. All such re-expansions are again greatly accelerated (Zinchenko & Davis 2000; paper I) by rotational transformations of spherical harmonics, and the cumulative Lamb's regular series from all surfaces $\widehat{S}^{min}_\beta + \boldsymbol{m}$ 'sufficiently separated' from S_α is then efficiently evaluated at all nodes $\boldsymbol{y} \in S_\alpha$.

For 'self-interactions' ($S_\alpha = \widehat{S}_\beta = \widehat{S}^{min}_\beta$ and $\boldsymbol{m} = 0$), the free-space contribution of $S^{min}_\beta + \boldsymbol{m}$ to (2.13) is calculated using the second level of mesh-node decomposition (into patches). Namely, Lamb's singular expansions for all patches $\mathscr{B}_\gamma \subset S_\alpha$

https://doi.org/10.1017/jfm.2013.197 Published online by Cambridge University Press

'sufficiently separated' from a given patch $B_\delta \subset S_\alpha$ are re-expanded into Lamb's regular forms near $\boldsymbol{x}_\delta^o$ (via a rotation-based algorithm to expedite this operation), and the resulting cumulative regular Lamb's series is evaluated at all mesh nodes $\boldsymbol{y} \in \mathscr{B}_\delta$. If a patch $\mathscr{B}_\gamma$ is not 'sufficiently separated' from $\mathscr{B}_\delta$, then the contribution of $\mathscr{B}_\gamma$ to (2.13) for $\boldsymbol{y} \in \mathscr{B}_\delta$ is computed either by: (i) Lamb's singular series around $\boldsymbol{x}_\gamma^o$; or (ii) by direct summation. The first strategy is chosen when the observation node $\boldsymbol{y}$ is 'well outside' the spherical shell $\mathscr{D}_\gamma$, so that Lamb's singular series has enough convergence to be more efficient than direct summation.

Another scheme is used to compute the free-space contribution from $\widehat{S}_\beta^{min} + \boldsymbol{m}$, when this surface is different, but not 'sufficiently separated' from $S_\alpha \ni \boldsymbol{y}$. Lamb's singular series for the entire surface $S_\beta^{min} + \boldsymbol{m}$ is used if $\boldsymbol{y}$ is outside the shell $\mathscr{D}_\beta^{min} + \boldsymbol{m}$ and the order of multipoles in the series required for convergence does not exceed a given threshold k_o (chosen from efficiency considerations, see below). Otherwise, we consider the free-space contribution from $\widehat{S}_\beta^{min} + \boldsymbol{m}$ to (2.13) as a sum from individual patches and employ for each patch either Lamb's singular series (only if the order of multipoles necessary for convergence is within k_o) or direct summation, depending on which is more optimal.

The purpose of using two levels of mesh nodes decomposition for solid particles (into patches and the entire surfaces) is to retain efficiency for the very fine triangulations ($\widehat{N}_\Delta \sim 10^4$ boundary elements per particle) inevitable in the present simulations. Our experience with two-body interactions (Zinchenko & Davis 2005) suggests that even superhigh surface resolution ($N_\Delta \sim 10^5$) in BI calculations does not require additional, finer levels of node decomposition.

The inhomogeneous term $\boldsymbol{F}(\boldsymbol{y})$ in (2.4) also requires multipole-accelerated calculation. However, since $\boldsymbol{F}(\boldsymbol{y})$ is taken out of iterations, and because drop surfaces require somewhat less resolution than solid particles do, we use for $\boldsymbol{F}(\boldsymbol{y})$ a simplified calculation scheme, without drop-surface partitioning into patches, which almost parallels our initial algorithm (Zinchenko & Davis 2000) for drop–drop interactions; details are provided in paper I.

2.4. *Economical truncation of multipole expansions*

As in our previous multidrop algorithms (Zinchenko & Davis 2000, 2002, 2003), a very essential feature of the present code is the 'economical truncation' of multipole expansions/re-expansions depending on a single precision parameter $\varepsilon \ll 1$ and a threshold $k_o \gg 1$. This truncation takes into account, in a nearly optimal fashion, that the convergence rate for Lamb's singular series around a patch $\mathscr{B}_\gamma$ or around a whole surface S_β strongly depends on the ratio ($d_\gamma^o/\|\boldsymbol{y} - \boldsymbol{x}_\gamma^o\|$ or $d_\beta^o/\|\boldsymbol{y} - \boldsymbol{x}_\beta^o\|$) of the minimal shell radius around $\mathscr{B}_\gamma$ or S_β to the distance from the expansion centre. Likewise, the convergence rate for re-expansion from Lamb's singular to regular series depends strongly on the clearance between the minimal shells $\mathscr{D}_\gamma$, $\mathscr{D}_\delta$ (or $\mathscr{D}_\beta$, $\mathscr{D}_\alpha$) around the corresponding patches or entire surfaces. Details of construction of economical truncation bounds for near-field and far-field interactions are given in paper I. Although the intuitive parameter ε is not a deviation of the solution from the non-multipole solution (by standard summations), it does correlate with this deviation. As $\varepsilon \to 0$, all multipoles are eventually included, which guarantees the convergence to the (much slower) non-multipole solution. For efficiency, the threshold k_o limits the use of multipoles; if a truncation bound for a particular operation exceeds k_o, direct summations are invoked instead. An optimum range for k_o (30–40 in the present work) depends slightly on surface resolution.

https://doi.org/10.1017/jfm.2013.197 Published online by Cambridge University Press

3. Mesh control on drop surfaces

It is well-known in BI and front-tracking simulations for deformable objects that simply advecting the surface mesh nodes with the interfacial (or normal) velocity results in severe mesh degradation in a short simulation time; internode distances become highly irregular, with 'skinny', almost degenerate mesh triangles. A traditional remedy is to restructure the mesh as needed, by nodes addition/subtraction/reconnection (Unverdi & Tryggvason 1992; Tryggvason *et al.* 2001). In free-space breakup simulations for single drops (Cristini *et al.* 2003), a more elaborate version (Cristini, Bławzdziewicz & Loewenberg 1998; Cristini *et al.* 2001) was widely used, with additional adaptive mesh-node redistribution to minimize a potential, spring-like mesh energy.

An alternative approach, 'passive mesh stabilization', originated in Zinchenko *et al.* (1997) and used, in various forms, in multidrop simulations (Zinchenko & Davis 2000, 2002, 2003) seeks to prevent mesh degradation not through topological changes, but by adding a tangential field to the normal velocity, found globally (but independently) for each surface to minimize a 'kinetic energy' of disordered mesh motion. This technique, with soft stability limitations on the time step, is able to greatly slow down mesh degradation, but does not eliminate it completely. For this reason, in squeezing simulations of paper I, this approach was combined with (very rare) 'active' mesh restructuring through minimization of some form of 'potential energy'. This strategy, however, was insufficient for the present systematic simulations performed in much longer time intervals for averaging, and for drops closely approaching breakup. A vastly improved mesh control scheme described below uses new forms of 'kinetic' and 'potential' mesh energy functions combined with the simplest topological mesh transformations. This very robust scheme maintains the quality of curvature-adaptive surface triangulations for drop shapes of virtually any complexity encountered in long-time simulations of the emulsion flow through a granular material.

3.1. *Method 1: passive mesh stabilization*

In this part of the mesh-control algorithm, at any instant of time, the mesh-vertex velocities $\boldsymbol{V}_i = \mathrm{d}\boldsymbol{x}^i/\mathrm{d}t$ on $\widetilde{S}_\alpha$ to be used in the drop-shape update are required to minimize a 'kinetic energy' function

$$F = \sum_{\boldsymbol{x}_{ij}} \left[\frac{\mathrm{d}}{\mathrm{d}t} \left(\frac{\boldsymbol{x}_{ij}^2}{h_{ij}^2} + \frac{h_{ij}^2}{\boldsymbol{x}_{ij}^2} \right) \right]^2 + 0.4 \sum_{\Delta} \frac{1}{C_\Delta^2} \left(\frac{\mathrm{d}C_\Delta}{\mathrm{d}t} \right)^2 \tag{3.1}$$

under the constraints $\boldsymbol{V}_i \cdot \boldsymbol{n}(\boldsymbol{x}^i) = \boldsymbol{u}(\boldsymbol{x}^i) \cdot \boldsymbol{n}(\boldsymbol{x}^i)$, where the interfacial velocities $\boldsymbol{u}(\boldsymbol{x}^i)$ are provided by the BI solution.

The second sum in (3.1), which resists mesh triangle collapse, has the same form as in paper I (to within a factor). It contains summation over all mesh triangles Δ on $\widetilde{S}_\alpha$, with $C_\Delta = S_\Delta/(a^2 + b^2 + c^2)$ being the 'compactness' of triangle Δ with (flat) area S_Δ and sides a, b, c. Expressing S_Δ in terms of the vertex coordinates allows us to write this sum as a quadratic function of the node velocities $\boldsymbol{V}_i$.

The first sum (3.1), substantially different from that in paper I, contains summation over all mesh edges $\boldsymbol{x}_{ij} = \boldsymbol{x}^j - \boldsymbol{x}^i$ (with $i < j$) between directly connected nodes on $\widetilde{S}_\alpha$. This term works to prevent significant deviation of internode distances $\|\boldsymbol{x}_{ij}\|$ from local

https://doi.org/10.1017/jfm.2013.197 Published online by Cambridge University Press

'target' values h_{ij}, defined as

$$h_{ij}^2 = \frac{1}{2}(h_i^2 + h_j^2), \quad h_i^2 = K\Lambda^{-\gamma}(\boldsymbol{x}^i), \tag{3.2}$$

$$\Lambda(\boldsymbol{x}) = k_1^2(\boldsymbol{x}) + k_2^2(\boldsymbol{x}) + 0.004/\widetilde{a}_\alpha^2, \tag{3.3}$$

$$K = \frac{4}{\sqrt{3}\widetilde{N}_\Delta^\alpha} \sum_{\boldsymbol{x}^j \in \widetilde{S}_\alpha} \Lambda^\gamma(\boldsymbol{x}^j)\Delta S_j, \tag{3.4}$$

with area elements ΔS_j discussed in § 2.2. As in the rest of the code, local principal curvatures k_1, k_2 are calculated in the mesh vertices by the best paraboloid-spline method of Zinchenko & Davis (2000), together with the normal vectors $\boldsymbol{n}(\boldsymbol{x}^i)$. An artificial term $0.004/\widetilde{a}_\alpha^2$ in $\Lambda(\boldsymbol{x})$ (with $\widetilde{a}_\alpha$ being the non-deformed drop radius) is typically small, but added for stability, should there be nearly flat spots on the drop surface with k_1, $k_2 \approx 0$. According to (3.2), the local 'target' scale for the mesh spacing is roughly proportional to $|k(\boldsymbol{x})|^{-\gamma}$, with γ being the adaptivity exponent; still, $(k_1^2 + k_2^2)^{1/2}$ is a better measure for the local curvature than $k = (k_1 + k_2)/2$, since k_1 and k_2 may partially cancel each other. Only moderate adaptivity was found useful in the present calculations, and γ was set to 0.25. Finally, the expression (3.4) for the factor K corresponds to an idealized case, when all $\widetilde{N}_\Delta^\alpha \gg 1$ mesh triangles on $\widetilde{S}_\alpha$ are approximately equilateral, with sides $(K\Lambda^{-\gamma})^{1/2}$ slowly varying along the surface. The coefficients 0.4 and 0.004 (precise values are unimportant) in (3.1) and (3.3) were set to provide good mesh quality in several test runs with $\widetilde{N}_\Delta^\alpha = 3840$. Once convergence with respect to triangulations is reached (§ 6), these artificial mesh parameters do not affect the results.

Since h_{ij}^2 is a non-trivial function of the mesh-node positions, including h_{ij}^2 in the time-differentiation in (3.1) would severely complicate the algorithm. Fortunately, this was found to be unnecessary, since variation of the internode distances $\|\boldsymbol{x}_{ij}\|$ is far more important; so, h_{ij}^2 is regarded as time-independent in the operation (3.1). With this simplification, the whole kinetic energy (3.1) is handily written as a quadratic function of the velocities $\boldsymbol{V}_i$ and minimized by conjugate-gradient (CG) iterations (as in the original passive mesh stabilization version, (Zinchenko *et al.* 1997). With typically 50–70 iterations, the relative cost of passive mesh stabilization is negligible.

3.2. *Method 2: active mesh restructuring*

An alternative way to maintain the quality of our adaptive drop surface triangulation on $\widetilde{S}_\alpha$ (without topological changes to the mesh) is through active mesh-node redistribution, which seeks to minimize the 'potential energy'

$$E = \sum_{\boldsymbol{x}_{ij}} \left[\frac{1}{2}\left(\frac{\boldsymbol{x}_{ij}^2}{h_{ij}^2} + \frac{h_{ij}^2}{\boldsymbol{x}_{ij}^2}\right)\right]^p + \sum_\Delta \left(\frac{C_\Delta^{et}}{C_\Delta}\right)^r, \tag{3.5}$$

with chosen numerical constants $p = 50$ and $r = 100$. Again, the first sum is over all mesh edges $\boldsymbol{x}_{ij}$, and the second sum is over all mesh triangles Δ on $\widetilde{S}_\alpha$, with the same target scales h_{ij} as defined by (3.2)–(3.4); $C_\Delta^{et} = \sqrt{3}/12$ is the compactness of an equilateral triangle. The first sum in (3.5) is designed to increase without bound when $\|\boldsymbol{x}_{ij}\| \to 0$, thus helping us avoid mesh-node crowding. This form was observed to perform significantly better in the present simulations when drops squeeze with large deformations, compared with the simplest, physically motivated 'spring-like' form of

https://doi.org/10.1017/jfm.2013.197 Published online by Cambridge University Press

the potential energy; the choice of parameters p, r (provided $p \sim r$) has less effect. Even more beneficial was to include the second sum in (3.5), to prevent mesh-triangle collapse during minimizations of E.

Let $\boldsymbol{x}_o^i$ be mesh-node positions on $\widetilde{S}_\alpha$ prior to redistribution. For each $\boldsymbol{x}_o^i$, a best paraboloid $z'(x', y')$ locally fitting $\widetilde{S}_\alpha$ near $\boldsymbol{x}_o^i$ is constructed (Zinchenko *et al.* 1997), with z' being along the normal $\boldsymbol{n}(\boldsymbol{x}_o^i)$, and x', y' in the tangential plane at $\boldsymbol{x}_i^o$. In addition (with the constant (3.4) calculated via the mesh of $\boldsymbol{x}_o^j$), local quadratic approximations for $h(\boldsymbol{x}) = (K\Lambda^{-\gamma})^{1/2}$ in terms of x', y' are constructed near each node $\boldsymbol{x}_i^o$. With these prerequisites to speed up calculations, steepest-descent iterations are organized:

$$\boldsymbol{x}_{new}^i = \boldsymbol{x}^i - \delta \frac{\partial E}{\partial \boldsymbol{x}^i}, \quad \delta = 0.01 \min_i \left(\frac{\Delta x_i}{\|\partial E/\partial \boldsymbol{x}^i\|} \right), \tag{3.6}$$

where the minimum is over all mesh nodes $\boldsymbol{x}^i$, and Δx_i is the shortest distance from $\boldsymbol{x}^i$ to the nodes directly connected to it; the numerical coefficient 0.01 (larger than 0.001 used in paper I) still provides smooth mesh transition between iterations. Again, to avoid severe complications, the scales h_{ij} are treated as constants in differentiations (3.6) (see below). After the iteration (3.6), $\boldsymbol{x}_{new}^i$ is placed on the best paraboloid for the nearest node $\boldsymbol{x}_o^j \in \widetilde{S}_\alpha$. Likewise, $h(\boldsymbol{x})$ is quadratically interpolated to the new nodes $\boldsymbol{x}_{new}^i$, to continue the iterations (3.6); this h-interpolation compensates for incomplete differentiations in $\partial E/\partial \boldsymbol{x}^i$. Neither local quadratic approximations for $\widetilde{S}_\alpha$, $h(\boldsymbol{x})$, nor the constant (3.4) is updated. Note that we avoid interpolating $h^2(\boldsymbol{x})$, with sharper variation, since it can make the method unreliable. A standard way of expediting the search for the nearest node $\boldsymbol{x}_o^j$ would be through node assignment to cubic cells and using chaining mesh-linked list structure (Hockney & Eastwood 1981); here we use node-partitioning into 'patches' employed in paper I for this purpose.

On each νth iteration (3.6), the scatter of the mesh edges $\|\boldsymbol{x}_{ij}\|$ around the target values h_{ij}, and the lowest quality of mesh triangles are monitored:

$$\boldsymbol{Sc}(\nu) = \max_{\boldsymbol{x}_{ij}} \left(\frac{\|\boldsymbol{x}_{ij}\|}{h_{ij}} \right) \Big/ \min_{\boldsymbol{x}_{ij}} \left(\frac{\|\boldsymbol{x}_{ij}\|}{h_{ij}} \right), \quad C_\Delta^{min}(\nu) = \min_\Delta C_\Delta. \tag{3.7}$$

If no significant improvement in reducing $\boldsymbol{Sc}$ or increasing C_Δ^{min} is seen within 100 iterations, then all mesh changes (3.6) are undone. Namely, the mesh restructuring attempt for surface $\widetilde{S}_\alpha$ is abandoned, if $\boldsymbol{Sc}(\nu) > 0.75\,\boldsymbol{Sc}(0)$ and $C_\Delta^{min}(\nu) < 1.15\ C_\Delta^{min}(0)$ for all $\nu \leqslant 100$. Otherwise, 900 additional iterations (3.6) are performed to complete mesh restructuring for surface $\widetilde{S}_\alpha$; on average, these iterations are still inexpensive compared with the BI solution.

We do not attempt here, either in method 1 or 2, to adapt the mesh in regions of small surface clearance (drop–solid or drop–drop), and such adaptation is not viewed as a prospective approach in the present simulations. In addition to the complexity of such adaptation for multidrop–multiparticle configurations, eliminating *all* drop–drop and drop–solid overlaps through an adaptive mesh would still require impractically high resolution; there is a better way to control these overlaps with negligible effect on global dynamics (see § 5). Curvature-adaptive meshes still help to reduce the numerical trend for surface overlapping, since the transition regions (most prone to overlapping) to the thin films have higher curvature. Most important, however, is curvature-adaptivity in breakup simulations. Full resolution of near-contact interactions

https://doi.org/10.1017/jfm.2013.197 Published online by Cambridge University Press

would be most crucial for nearly non-deformed drops (Zinchenko & Davis 2005) but this case is not considered herein.

3.3. *Method 3: node reconnection (edge swapping)*

In this, standard part of our mesh control, a search is made through all mesh edges $[\boldsymbol{x}^i, \boldsymbol{x}^j]$ on $\widetilde{S}_\alpha$, with adjacent mesh triangles $[\boldsymbol{x}^i, \boldsymbol{x}^j, \boldsymbol{x}^k]$ and $[\boldsymbol{x}^i, \boldsymbol{x}^j, \boldsymbol{x}^m]$. The edge $[\boldsymbol{x}^i, \boldsymbol{x}^j]$ is replaced with $[\boldsymbol{x}^k, \boldsymbol{x}^m]$, if: (i) after this operation each of the nodes $\boldsymbol{x}^i$ and $\boldsymbol{x}^j$ would still have at least five neighbours; and (ii)

$$|\boldsymbol{x}^k - \boldsymbol{x}^m|^2 < |(\boldsymbol{x}^k - \boldsymbol{O}_k) \cdot (\boldsymbol{x}^m - \boldsymbol{x}^k)| + |(\boldsymbol{x}^m - \boldsymbol{O}_m) \cdot (\boldsymbol{x}^m - \boldsymbol{x}^k)|, \tag{3.8}$$

where $\boldsymbol{O}_k$, $\boldsymbol{O}_m$ are the circumcentres for the triangles $[\boldsymbol{x}^i, \boldsymbol{x}^j, \boldsymbol{x}^k]$ and $[\boldsymbol{x}^i, \boldsymbol{x}^j, \boldsymbol{x}^m]$, respectively. Requirement (i) is essential for the local-parabolic surface approximation (Zinchenko *et al.* 1997), while (3.8) is equivalent to Delaunay triangulation (considering the surface as locally flat). Criteria (i) and (ii) were also used by Cristini *et al.* (2001). To obtain good mesh quality for drops closely approaching breakup, it is important to do edge swapping iteratively. Namely, once the first edge $[\boldsymbol{x}^i, \boldsymbol{x}^j]$ to be swapped is found on $\widetilde{S}_\alpha$, the mesh topology is updated and the search is made again over mesh edges around $[\boldsymbol{x}^i, \boldsymbol{x}^j]$ (or over all edges, for simplicity) to find the next edge to be swapped and so on, until there are no node pairs to be reconnected.

3.4. *Combined mesh-control scheme*

Our combined mesh-control strategy works as follows. Before each cycle of 100 time steps, method 2 is applied to all drops (the probability of actual mesh restructuring being typically 20–50 %). At each time step of the cycle, the mesh nodes on all drops are first advanced by method 1. Then, each surface $\widetilde{S}_\alpha$ is tested/restructured by method 3. If at least one edge swapping has occurred for $\widetilde{S}_\alpha$, then method 2 is called for this surface, but no more often than every five time steps for each surface $\widetilde{S}_\alpha$.

Owing to strong mesh control provided by methods 1 and 2, with new energy functions, it was sufficient in the present work to complement them with relatively simple node reconnections, thus avoiding more complex mesh operations (node addition/subtraction) altogether. In long-time calculations of § 6, all three components of mesh control were essential. For example, if passive mesh stabilization is replaced by simply advecting the nodes with interfacial or normal velocity, then mesh restructuring by methods 2 and 3 has to be used much more often, leading to much larger number of BI iterations and much slower calculations overall.

4. A novel fragmentation algorithm in drop breakup simulations

Drops occasionally break in the present simulations, and the drop shapes can be very complex at breakup (see § 6). An example in figure 2 demonstrates evolution of a drop to breakup into two fragments. Geometrical constraints imposed by solid particles tend to limit drop elongation somewhat, and they create characteristic dimples on drop surfaces. Continuing the simulation after each breakup requires a robust fragmentation algorithm. A mesh splicing technique originated by Cristini *et al.* (2001) starts from identifying two sets (contours) of splicing nodes (some distance away from the narrowest neck location), which are then repositioned to lie in the splicing planes. This repositioning is achieved by globally restructuring the whole mesh. The next step is to generate two spherical caps approximately matching the drop surface at the splicing contours; this operation requires cap triangulation combined with node

https://doi.org/10.1017/jfm.2013.197 Published online by Cambridge University Press

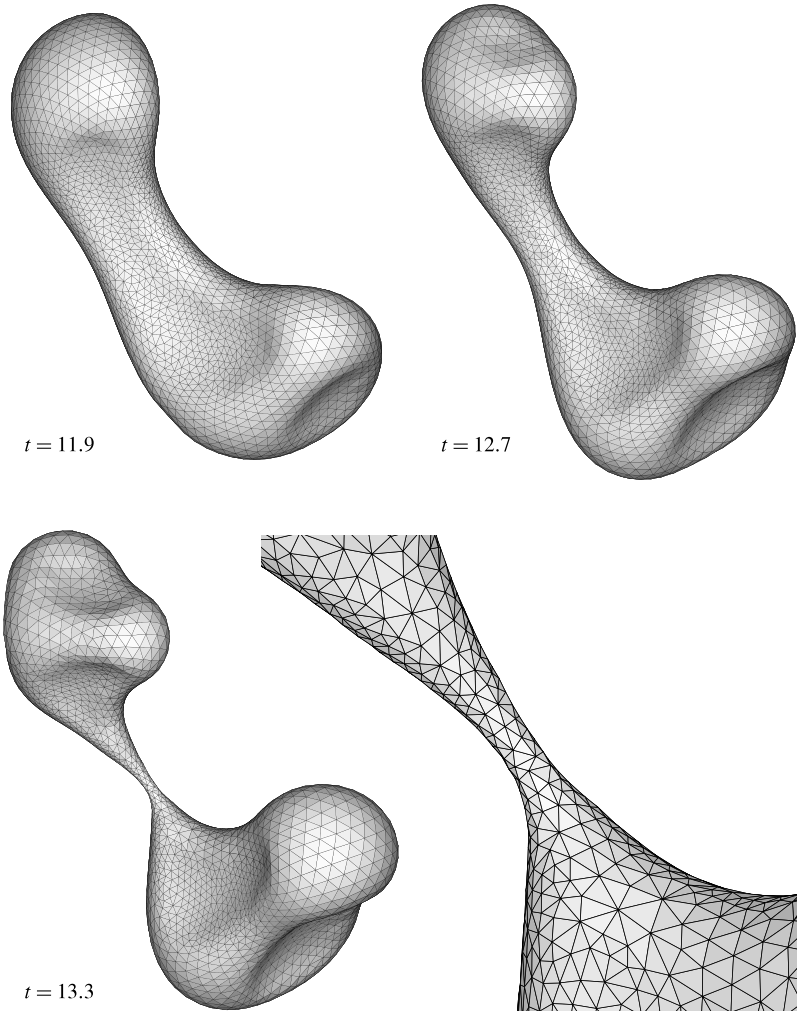


FIGURE 2. An example of drop shape evolution to primary breakup in an emulsion flow though a packed granular material, with 6000 triangular elements on a drop surface. Time is scaled as defined in § 6. The close-up shows the neck region at $t = 13.3$.

addition/subtraction to achieve one-to-one correspondence with the nodes on the splicing contours. The procedure is completed by global mesh relaxation to smooth the transition between the new drop surfaces and the added caps. Bazhlekov, Anderson & Meijer (2004) used the same or a similar mesh-splicing technique. Another similar algorithm, 'mesh separation' (Quan & Schmidt 2007; Quan, Lou & Schmidt 2009*a*; Quan *et al.* 2009*b*) uses a combination of tetrahedral volume meshing with triangular surface meshing to fragment a breaking drop in moving-mesh, interface-tracking simulations. All of these techniques appear to be non-trivial, and little detail is provided on how to use them in a general case, for most complex drop shapes. In particular, it is not clear to us how to automatically choose the splicing contours, and the location/orientation of the splicing planes. All of the numerical examples in the literature are for highly stretched shapes, with very thin almost circular necks, when

https://doi.org/10.1017/jfm.2013.197 Published online by Cambridge University Press

such choices are easier to make. It would be wasteful to proceed to very thin necks in the present multidrop–multiparticle simulations due to prohibitively small time step at ultimate pinch-off, and it is not necessary at all for accurate tracking of the global dynamics of the drop phase. A restriction on the existing mesh splicing techniques is that the fragments necessarily inherit the global resolution from the parent drop. To avoid numerical difficulties, though, it is generally desirable in our simulations to have higher resolution on the fragments, since they are subject to subsequent close interaction with other drops and solids, and often to secondary breakup.

For these reasons, we have taken a novel, and entirely different approach to drop fragmentation in the present work. A parent drop $\widetilde{S}_\alpha$ is fragmented once the local curvature $\max(|k_1|, |k_2|)$ reaches (27–30) $\widetilde{a}_\alpha$. The first step is to enclose $\widetilde{S}_\alpha$ by a rectangular box (shown schematically in figure 3*a*), preferably (but not necessarily) with tight fit. One side of the box is chosen along the line of maximum elongation (which maximizes the internode distances $\|\boldsymbol{x}^j - \boldsymbol{x}^i\|$ on $\widetilde{S}_\alpha$). For all points $\boldsymbol{y}$ of a Cartesian mesh (typically 40^3 or 50^3) covering the box, the indicator function

$$I(\boldsymbol{y}) = \frac{1}{4\pi} \int_{\widetilde{S}_\alpha} \frac{\boldsymbol{r} \cdot \boldsymbol{n}(\boldsymbol{x})}{r^3} \, \mathrm{d}S_x, \quad \boldsymbol{r} = \boldsymbol{x} - \boldsymbol{y} \tag{4.1}$$

is calculated; $I(\boldsymbol{y}) = 1$ for $\boldsymbol{y}$ inside $\widetilde{S}_\alpha$ and $I(\boldsymbol{y}) = 0$ otherwise. Assuming flat triangulation of $\widetilde{S}_\alpha$, the integral (4.1) is handled analytically, since the contribution of each mesh triangle $\Delta \in \widetilde{S}_\alpha$ is simply $\pm$ the area of the spherical triangle formed by projecting Δ onto the unit sphere centred at $\boldsymbol{y}$. For each point $\boldsymbol{y}$ with $I(\boldsymbol{y}) = 1$, the minimum distance $d(\boldsymbol{y}, \widetilde{S}_\alpha)$ from $\boldsymbol{y}$ to the enclosing triangulated surface $\widetilde{S}_\alpha$ is calculated; to this end, a simple lower estimate of the point-to-triangle distances suffices. A point $\boldsymbol{y} = \boldsymbol{y}_1$ with maximum $d(\boldsymbol{y}, \widetilde{S}_\alpha)$ determines (approximately) the centre of the largest sphere of radius $R_1 = d(\boldsymbol{y}_1, \widetilde{S}_\alpha)$, which can be inscribed into the drop $\widetilde{S}_\alpha$. To construct the second sphere inside $\widetilde{S}_\alpha$ (figure 3*a*), the whole procedure is repeated, with the restriction that the test point $\boldsymbol{y}$ does not belong to the same bulb of $\widetilde{S}_\alpha$ as $\boldsymbol{y}_1$. The simplest way to enforce this restriction is by excluding points $\boldsymbol{y}$ with $\|\boldsymbol{y} - \boldsymbol{y}_1\| < fR_1$. A quick look at the three-dimensional graphical image of $\widetilde{S}_\alpha$ suggests appropriate values of f (typically $f = 2.5$–4.5). In extremely rare cases, with a drop $\widetilde{S}_\alpha$ of very crooked shape, the newly found centre $\boldsymbol{y} = \boldsymbol{y}_2$ may still be in the same bulb as $\boldsymbol{y}_1$; in such instances, it was sufficient to repeat the procedure one more time, excluding the areas around $\boldsymbol{y}_1$ and $\boldsymbol{y}_2$ for the test points $\boldsymbol{y}$.

The spherical surfaces S_1, S_2 constructed inside $\widetilde{S}_\alpha$ (figure 3*a*) are slightly shrunk (by 2 %) about their centres, and triangulated into N_Δ^1 and N_Δ^2 elements, respectively, using the simple methods discussed in § 2.2. Note that N_Δ^1 and N_Δ^2 are unrelated to the parent drop triangulation, and can be chosen at will within a broad range. The surfaces S_1 and S_2 are then subject to 'swelling' (expansion) with deformation, until $S_1 \cup S_2$ closely fits the parent surface $\widetilde{S}_\alpha$. At each expansion step, the normal surface advancement in a mesh node $\boldsymbol{x}^i \in S_\beta (\beta = 1, 2)$ is empirically calculated as

$$0.1 \frac{D(\boldsymbol{x}^i)}{\max D(\boldsymbol{x}^j)} \min \left[\frac{\Delta x_j}{R_\beta \max(|k_1(\boldsymbol{x}^j)|, |k_2(\boldsymbol{x}^j)|)} \right]. \tag{4.2}$$

https://doi.org/10.1017/jfm.2013.197 Published online by Cambridge University Press

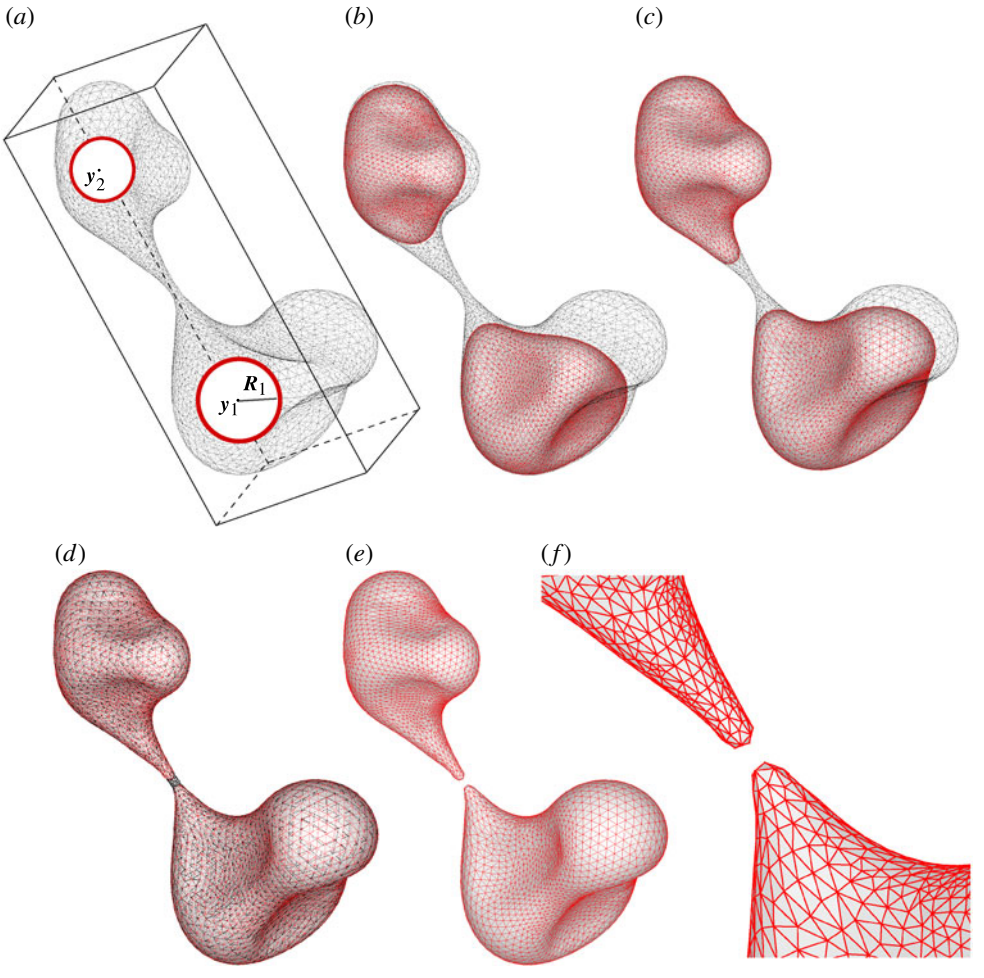


FIGURE 3. Fragmentation of the drop shape from figure 2 at $t = 13.3$ by the swelling technique; 5120 elements on each fragment (with red-coloured meshing). The mesh on the parent drop (black) is made transparent. (*a*) Initially spherical fragments inside the parent drop, with the bounding box (not to scale). (*b–d*) Swelling of the fragments inside the parent drop until close fit. (*e*) Same as (*d*), but without the parent drop surface. (*f*) Close-up of the fragments from (*e*) in the pinch-off region.

Here, max and min are over all mesh nodes $\boldsymbol{x}^j$ on S_β, and

$$D(\boldsymbol{y}) = \frac{\delta(\boldsymbol{y})}{1 + c_{exp}[k_1^2(\boldsymbol{y}) + k_2^2(\boldsymbol{y})]\delta(\boldsymbol{y})}. \tag{4.3}$$

Consider a ray $\mathscr{R}(\boldsymbol{y}) = \{\boldsymbol{x} : \boldsymbol{x} = \boldsymbol{y} + \nu\boldsymbol{n}(\boldsymbol{y}), \nu > 0\}$ emanating from $\boldsymbol{y} \in S_\beta$ $(\beta = 1, 2)$ in the direction of the outward normal $\boldsymbol{n}(\boldsymbol{y})$ to S_β. Clearance $\delta(\boldsymbol{y})$ is defined as the distance from $\boldsymbol{y}$ along $\mathscr{R}(\boldsymbol{y})$ to the nearest intersection point of $\mathscr{R}(\boldsymbol{y})$ with the parent surface; the coefficient c_{exp} has a weak effect and set to $0.125\widehat{a}$. In (4.2), Δx_j is the shortest distance from $\boldsymbol{x}^j$ to the nodes directly connected to it; R_β is the equivalent spherical radius of S_β. The proportionality of the displacements (4.2) to the mesh size on S_β is in line with Courant stability limitations. To calculate $\delta(\boldsymbol{y})$, the nearest flat-

https://doi.org/10.1017/jfm.2013.197 Published online by Cambridge University Press

mesh triangle Δ intersecting $\mathscr{R}(\boldsymbol{y})$ is first found on the parent surface $\widetilde{S}_\alpha$. Intersection of $\mathscr{R}(\boldsymbol{y})$ with the best paraboloid, which locally approximates $\widetilde{S}_\alpha$ around one of the vertices of Δ, is then used to refine $\delta(\boldsymbol{y})$.

Smoothing of normal displacements (4.2) is usually necessary by adding the Laplacian term, with a small coefficient ($\epsilon \sim 10^{-3}$–10^{-4}) and zero mean over S_β, as described in § 5.2 of Zinchenko & Davis (2000). The combined mesh-control scheme of § 3 is used with these modified normal displacements, to advance the new surfaces S_1, S_2 and maintain the quality of adaptive triangulations for the entire swelling process; a slightly higher adaptivity parameter ($\gamma = 0.35$) than in the BI simulations is used herein. As an optional, but considerable speed-up of the algorithm, the mesh nodes on S_1, S_2 closely approaching the parent surface $\widetilde{S}_\alpha$ are gradually excluded from the further expansion process, the criterion being

$$\delta(\boldsymbol{y}) < 0.25(\widetilde{S}_\alpha)^{1/2}/\widetilde{N}^\alpha_\Delta, \tag{4.4}$$

and $\delta(\boldsymbol{y})$ is then set to zero for these nodes. However, whenever a surface S_β is restructured (by method 2 of § 3), all nodes on S_β are included again, with $\delta(\boldsymbol{y})$ recalculated and (4.4) rechecked.

The two surfaces S_1, S_2 swell independently; the surface-to-surface distance $\delta(S_1, S_2)$ is calculated infrequently for control purposes only. Once the maximum of principal curvatures on S_β approaches that of the parent drop $\widetilde{S}_\alpha$, it is the indication that S_β closely fits one bulb of $\widetilde{S}_\alpha$, and so this fragment S_β is excluded from further expansion to expedite the algorithm. The whole process is terminated once: (i) the surfaces S_1, S_2 nearly touch ($\delta(S_1,\ S_2) \sim 0.01\widehat{a}$); or (ii) the maximum principal curvature on each fragment is $(27\text{–}30)R_\beta$. The procedure, as described, is very reliable and has been used to handle a total of several hundred fragmentations with complex shapes in the present work. Close fit of $S_1 \cup S_2$ to the parent surface $\widetilde{S}_\alpha$ is obtained, with the volume discrepancy about 0.01–0.1 %. In one instance only did we see that the swelling fragments S_1, S_2 may touch well before closely fitting the parent surface $\widetilde{S}_\alpha$. A universal remedy is to include intersections of the ray $\mathscr{R}(\boldsymbol{y})$ with another fragment and redefine clearance $\delta(\boldsymbol{y})$ accordingly. Such modification, though, significantly slows down the algorithm. Instead, we have preferred, in this exclusive case, to simply adjust the expansion rates for S_1, S_2 to avoid the difficulty.

The mesh-control scheme, borrowed from dynamical BI simulations (§ 3), does not introduce any new complexity; the rest of our fragmentation algorithm is logically simple, compared with mesh splicing. In particular, there is no need to construct splicing contours, splicing planes or matching triangulated caps. A unique feature of the present algorithm is flexible (and simple), on-demand control of fragment resolution, since the meshes on fragments are built from scratch, with no relation to the parent drop meshing. Figure 3(*b–e*) show the fragment construction by expansion for the parent drop shape from figure 2, while figure 3(*f*) presents the mesh closeup from figure 3(*e*). Each fragment has 5120 triangular elements. Such a simulation typically takes a few minutes to generate the initial spheres S_1, S_2 (figure 3*a*), followed by 12–13 min of CPU time for the expansion, on a PC. In our earlier runs for this work, the number of triangular elements on each fragment was set to be the same as for the parent drop. In more recent runs, we preferred to choose the number of elements on a fragment to be between that for the parent drop and the value suggested by mesh splicing. The latter is easily estimated from the number of nodes in each bulb: excluding high-curvature nodes, the rest fall into two distinct connected sets.

https://doi.org/10.1017/jfm.2013.197 Published online by Cambridge University Press

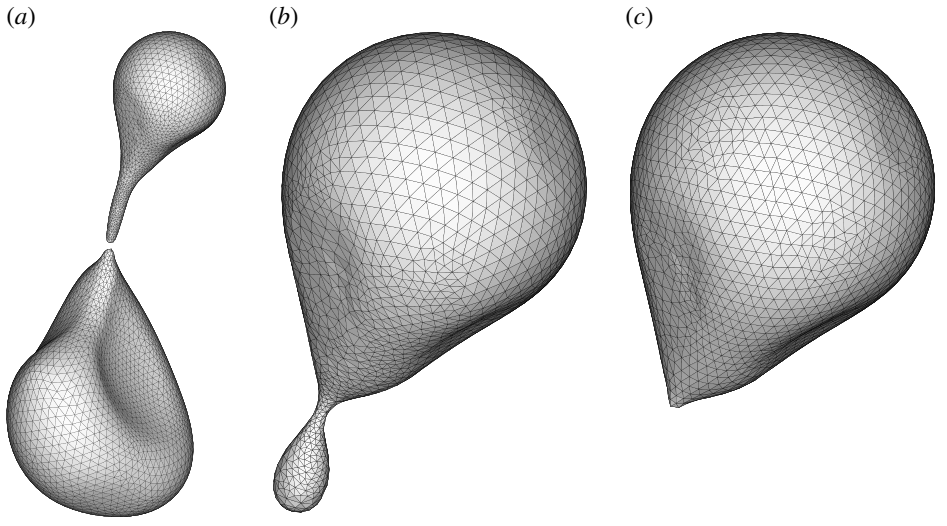


FIGURE 4. (*a*) Primary drop breakup followed by (*b*) secondary breakup of the top fragment, with a small satellite formation, neglected (*c*) in further simulation. Note that meshing on the fragments in (*a*) and (*c*) is built from scratch by swelling, unrelated to the parent resolution.

Unlike in figure 2, thin, long necks are observed prior to breakup in some of our simulations. In such cases, the termination criterion (ii) (see above) did not provide for close contact of fragments S_1, S_2. However, the neglected part of the parent drop neck was always $\approx 0.1\,\%$ of the parent drop volume, and did not have any appreciable effect on the volume fraction of the entire multidrop phase or global dynamics, even in simulations with multiple breakup. Expansion of fragments S_1, S_2 to near-contact is computationally more expensive in this case, and unnecessary in the present applications.

Owing to the lack of symmetries in the present problem, only binary breakups are possible. However, primary breakups are often followed by secondary breakups (figure 4). In case one of the bulbs at breakup is very small (less than $1\,\%$ of the secondary parent drop volume), it was neglected altogether to not slow down further simulation. A simple way to do so is by expanding fragment S_1 only inside the parent drop, until criterion (ii) is met; in this manner, meshing in figure 4(*c*) was generated. Such events were rare and, again, did not have a global effect.

5. Miscellaneous details of the methodology

5.1. *Control of surface overlapping*

If the problem was solved exactly (in the absence of singular molecular forces not considered herein), lubrication layers would prevent drop–solid and drop–drop contacts. Even if the critical squeezing conditions are reached, and some (or all) drops become trapped in the constrictions, there should still be some drop–solid and drop–drop clearance due to the pumping mechanism (Nemer 2003; Nemer *et al.* 2004) of the external flow pushing the fluid into the gaps. The existence of small, but non-zero lubrication gaps was demonstrated in high-resolution simulations of flow-induced single drop squeezing through a tight free-space cluster of two or three particles (Zinchenko & Davis 2006), both for supercritical and subcritical conditions.

https://doi.org/10.1017/jfm.2013.197 Published online by Cambridge University Press

In the present, much more demanding multidrop–multiparticle problem, elimination of *all* surface overlaps would require exorbitant resolution and prohibitive computational cost. Instead in paper I, an artificial geometric barrier, denoted by δ^{ds}_{min} herein, was imposed to prevent drop–solid contacts. Let $\mathscr{R}(\boldsymbol{y}) = \{\boldsymbol{x} : \boldsymbol{x} = \boldsymbol{y} + \nu \boldsymbol{n}(\boldsymbol{y}), \nu > 0\}$ be the ray emanating from a drop mesh node $\boldsymbol{y}$, and $\delta^{ds}(\boldsymbol{y})$ be the distance from $\boldsymbol{y}$ along $\mathscr{R}(\boldsymbol{y})$ to the nearest intersection point with solid surfaces. On each time step, all mesh nodes $\boldsymbol{y}$ entering the zone $\delta^{ds}(\boldsymbol{y}) < \delta^{ds}_{min}$ are pushed back along $-\boldsymbol{n}(\boldsymbol{y})$ to make $\delta^{ds}(\boldsymbol{y}) = \delta^{ds}_{min}$. This *ad hoc* procedure was successful and justified in sample calculations of paper I, because lubrication was 'almost resolved' and the above geometrical correction was required only for an extremely small portion of the total number of nodes on drops; the global results were found to be insensitive to the choice of δ^{ds}_{min}. The same remedy is used in the present calculations, with $\delta^{ds}_{min} = 0.009\widehat{a}$.

Small drop–drop overlaps were also observed in paper I, but were ignored altogether. This strategy was satisfactory in sample calculations of paper I, but not in the present work with many more systematic runs in a much wider time range; accumulation and growth of overlaps would eventually destroy the solution. So, prevention of drop–drop contacts was added to the present code. The principle is the same as for drop–solid contacts (see above), but with a different barrier $\delta^{dd}_{min} = 0.001\widehat{a}$. All nodes $\boldsymbol{y}$ on drop surfaces subject to geometrical drop–solid correction are now skipped. Instead of $\delta^{ds}(\boldsymbol{y})$, we work with clearance $\delta^{dd}(\boldsymbol{y})$, which is the distance from $\boldsymbol{y}$ along $\mathscr{R}(\boldsymbol{y})$ to the nearest intersection with drop surfaces. Unlike for $\delta^{ds}(\boldsymbol{y})$, the clearance $\delta^{dd}(\boldsymbol{y})$ cannot be calculated exactly. We first find the nearest intersection of $\mathscr{R}(\boldsymbol{y})$ with flat mesh triangles on drop surfaces. For the corresponding triangle, the vertex nearest to the intersection point is selected. Finally, the intersection of $\mathscr{R}(\boldsymbol{y})$ with the best local paraboloid constructed around this vertex is used to calculate $\delta^{dd}(\boldsymbol{y})$. Again, the drop–drop corrections are applied to a very small portion of nodes on drops, and were not observed to compromise the overall accuracy (§ 6).

5.2. *Time stepping, volume rescaling and smoothing*

The same empirical rule, as in paper I, is used herein for the time step, but with a smaller numerical constant $K_{\Delta t} \approx 6$ (versus 7.4) to provide stability in all cases. This rule, based on the capillary number, local mesh size and local curvatures, dictates generally a very small time step due to tight squeezing conditions and/or complex drop shapes. For this reason, only the simplest, Euler time marching scheme makes sense in the present problem (as was found in paper I), the time integration error being still less than triangulation effects.

As in paper I, a common shape-rescaling procedure is applied at each time step to keep the drop volumes constant and thereby reduce long-time cumulative errors; the rescaling effect disappears altogether in the limit of fine triangulations. Unlike in paper I, though, dynamical drop-shape smoothing was found to be unnecessary in the present work.

5.3. *Iterative method*

Since the solid-boundary condition is in the resistance formulation, simple iterations of the BI system $\boldsymbol{q} = \boldsymbol{A}\boldsymbol{q} + \boldsymbol{B}$ for the Hebeker density (§ 2.1) are divergent; a version of the GMRES technique is used instead. Namely, simple iterations $\boldsymbol{q}_{i+1} = \boldsymbol{A}\boldsymbol{q}_i + \boldsymbol{B}$ just form the base for the improved approximation $\boldsymbol{q}^{\rm imp}_{\nu} = \boldsymbol{q}_o + \sum \lambda_j (\boldsymbol{q}_j - \boldsymbol{q}_o)$, with $1 \leqslant j \leqslant \nu$ and parameters λ_j calculated for every ν to minimize the L_2-norm of the residual of $\boldsymbol{q}^{imp}_{\nu}$. If ν reaches 12 with $\boldsymbol{q}^{imp}_{\nu}$ still not converged, the process is restarted from $\boldsymbol{q}^{imp}_{\nu}$ as the new initial approximation $\boldsymbol{q}_o$. This GMRES version is often more economical

https://doi.org/10.1017/jfm.2013.197 Published online by Cambridge University Press

than the one used in paper I. Construction of the initial approximation $\boldsymbol{q}_o$ from the preceding time steps, and termination of iterations in this work follow the recipes from paper I. A typical number of BI iterations per time step is 6–9 in the simulations with tight squeezing and no breakup; it can be 2–2.5 times larger in the runs with more drop deformation and breakup, because of more frequent active mesh restructuring.

5.4. *Generation of solid-particle configurations*

An appropriate model used herein for solid-particle arrangement is a random packing of equisized spheres in mechanical equilibrium (against a confining pressure, if applied), with periodic boundaries. It is well-known from physical experiments (Scott & Kilgour 1969) that a large number of realistic frictional balls poured into a large vessel produce a packing between the limits of random 'loose' and close packing, and shrink to close packing only after a subsequent long shaking or vibration. The RCP limit, which is the densest state frictionless particles can be randomly packed into, is well-studied by simulations. Most methods to approach RCP are thermodynamical, molecular-dynamics-like or Monte Carlo, not seeking to generate mechanically equilibrium states, but exploiting instead an analogy of RCP with supercooled liquids (see Torquato 2002 and references therein). There are also mechanical, discrete-element (DEM) simulations assuming some particle softness (extremely small in practice). An entirely different RCP algorithm of Zinchenko (1994) is unique in that it produces mechanically equilibrium states for absolutely rigid spheres, with explicit calculation of contact forces (see also Zinchenko 1998). RCP is a well-defined limit, with the packing density (solid volume fraction) of $c_s = 0.637$ and an average coordination number of six.

However, we have found the RCP geometry to be too difficult for emulsion-flow simulations, at least for the emulsion concentrations and drop-to-particle size ratios considered herein. Instead, an opposite, but still physically interesting limit of RLP, corresponding to large interparticle friction, is assumed in the present paper. Experiments of Scott & Kilgour (1969) with nylon ground balls (static friction coefficient of 0.6) yield the packing density of $c_s \approx 0.575$. Onoda & Liniger (1990) observed very slow sedimentation of spheres in a viscous fluid to a packed state, to obtain $c_s = 0.555 \pm 0.005$, which is widely regarded as the RLP packing density; other experiments (Farrell, Martini & Menon 2010) claiming even lower densities were not as careful in eliminating finite-size effects. Available computer simulations of RLP for soft spheres by DEM or molecular-dynamics-like methods are scarce and too ambiguous to compare with the experiments of Scott & Kilgour (1969) and Onoda & Liniger (1990). These simulations rely on a large number of parameters (normal and tangential stiffness, restitution coefficient, Poisson ratio, etc.) and especially on artificial, kinetics-determined densification protocols. In particular, the results of Zhang & Makse (2005) were found to be quite sensitive to arbitrary compression rates. The simulations of Silbert (2010) do not approach the high-friction limit but point to significant underprediction of RLP density, if this limit could be reached.

Owing to severe challenges of emulsion flow simulations (a necessary very high resolution, with $O(10^4)$ boundary elements per surface, iterative BI solution on each time step, and a very large ($\sim 10^4$–10^5) total number of time steps in each run for reliable averaging), only packings with a modest number $\widehat{N}$ of solid spheres per cell could be afforded in the present work. In this limited range, we found an entirely new RLP simulation method to be beneficial and free from ambiguities inherent in other packing algorithms. This method, outlined in appendix B, is a generalization of Zinchenko's (1994) RCP algorithm. It is for absolutely rigid, absolutely rough

https://doi.org/10.1017/jfm.2013.197 Published online by Cambridge University Press

spheres, and is truly 'static' (kinetics-independent). Densification starts from a random configuration of non-touching spheres at volume fraction $c_o \ll 1$ and results in a perfect contact network of spheres in mechanical equilibrium (against the confining pressure, if applied) under the action of compressive normal and tangential contact forces. The average coordination number is close to four, as expected. There is no limitation in the algorithm on the magnitude of tangential forces. However, the analysis of our RLPs suggests that the RLP limit is a good approximation to realistic packing for friction coefficients as small as $O(1)$. Once the limit $c_o \to 0$ is taken to provide maximum randomness of the final packing, there are no free parameters whatsoever; values of $c_o = 0.15$ were found to suffice. With averaging over 100 realizations, we obtained packing densities $\langle c_s \rangle = 0.5081 \pm 0.0019$ and 0.5297 ± 0.0013 for $\widehat{N} = 50$ and 100, respectively. Linear extrapolation in $\widehat{N}^{-1}$ (due to periodic boundaries) suggests $c_s \approx 0.551$ at $\widehat{N} \to \infty$, in very good agreement with Onoda & Liniger's (1990) experiments.

For limited use in our emulsion flow simulations, 10 small packings with $\widehat{N} = 9$, densities c_s in the range 0.499–0.559 and average $\langle c_s \rangle = 0.526$ were generated. Medium-size packings ($\widehat{N} = 18$) included 9 realizations with densities $c_s = 0.508$–0.550 and average 0.529. Eight largest-size packings ($\widehat{N} = 36$) with $c_s = 0.521$–0.557 and average $\langle c_s \rangle = 0.535$ were also generated. In this RLP database, though, prepared at $c_o = 0.4$, the effect of c_o was overlooked, resulting in slightly higher densities compared with the true limit $c_o \to 0$; this drawback appears very minor.

In all RLP configurations selected for emulsion-flow simulations (see above), we slightly scale the particle radius by a factor of 0.9935 to make small gaps of $0.013\widehat{a}$ between formerly touching neighbours (all of the densities c_s reported in §§ 6 and 7 are after this shrinkage). This artificial shrinkage alleviates iterative convergence difficulties in the BI solution, but is expected to have only a small effect on the results. Moreover, the error introduced by shrinkage is partially compensated using the empirical single-phase Carman–Kozeny correlation for scaling the results in § 6. This scaling also helps to neutralize the effect of packing-density fluctuations inherent in our small-size RLP arrays.

5.5. *Generation of start-up drop configurations*

Each RLP configuration of $\widehat{N} = 9$, 18 or 36 solid spheres in a periodic cell is complemented by an initial random arrangement of $\widetilde{N}^o = 25$, 50 or 100 monodisperse drops, respectively. The drop-phase volume fraction in the entire space is fixed at 0.2. Thus, $\widetilde{N}^o/\widehat{N}$ is maintained at 25/9, while the emulsion concentration (in the space available to drops) fluctuates, being roughly 40 %. The equivalent non-deformed drop radius $\widetilde{a}^o$ for an initial arrangement is close to $\widehat{a}/2$; this value is much larger than a typical inner radius of interparticle constrictions, so drop squeezing requires significant deformation and can meet much resistance, depending on the capillary number. As the emulsion flows, the number $\widetilde{N}$ of drops in a periodic cell ($\widetilde{N} = \widetilde{N}^o$ initially) can grow due to breakups.

In this range of parameters, preparation of a start-up configuration requires drops to be deformed. To this end, the swelling technique of paper I is used. First, a configuration of $\widetilde{N}^o$ spherical drops in the interstitial space between the solids is generated by stochastic mixing, with gradual increase in the drop radii until this process halts (the attainable drop volumes still being well below the target values). Next, drops are allowed to swell with deformation but not reaching each other or

https://doi.org/10.1017/jfm.2013.197 Published online by Cambridge University Press

c_s	$\widehat{N}_\Delta = 8640$		11 520		24 000	
	Paper I	Present code	Paper I	Present code	Paper I	Mo & Sangani (1994)
0.4	21.15	21.24	21.17	21.24	21.20	21.24
0.45	27.92	28.08	27.97	28.08	28.03	28.09
0.5	36.72	37.00	36.80	37.01	36.91	37.00
0.5231	41.56	—	41.67	41.95	41.83	—
0.5236	—	42.04	—	42.07	—	42.1

TABLE 1. Non-dimensional drag F/F_o on a solid sphere for a single-phase flow through a simple cubic array. Multipole-accelerated BI solutions from paper I and the present code at various resolutions ($\widehat{N}_\Delta$) are compared with the purely multipole solution of Mo & Sangani (1994).

solid surfaces, until the target volumes for all drops are attained. This swelling is implemented as an artificial 'time-dependent' process, with the normal 'velocity' of surface expansion designed in a special way (paper I). However, systems of the largest size ($\widehat{N} = 36$, $\widetilde{N}^o = 100$) required generally a better mesh control scheme than in paper I to complete swelling. A combined, adaptive-mesh control strategy of § 3 was used instead without difficulties.

5.6. *Test for a single-phase flow through a simple cubic array*

Highly accurate multipole solutions for a single-phase Newtonian flow through a fixed simple cubic array of spheres ($\widehat{N} = 1$) in the whole range of particle volume fractions $c_s \leqslant \pi/6$ were obtained by Chapman & Higdon (1992) and Mo & Sangani (1994); the former work, being in perfect agreement with Mo & Sangani, even handles overlapping spheres $c_s > \pi/6$. The results are usually represented by the ratio F/F_o of the hydrodynamic force exerted on a bed particle to the Stokes drag $6\pi\mu\widehat{a}|\langle \boldsymbol{u}\rangle|$, where $\langle \boldsymbol{u}\rangle$ is the fluid velocity averaged over the entire space (with $\boldsymbol{u} = 0$ inside the solids). In paper I, very close agreement with the results of Mo & Sangani (1994) for dense simple cubic arrays was achieved, but only with a very large number $\widehat{N}_\Delta$ of triangular elements on the solid surface. Table 1 demonstrates much better convergence with the present code using the improved integration scheme over solid boundaries, as detailed in § 2.2 and appendix A. In the last row of table 1, we used the maximum packing density $\pi/6$ for non-overlapping spheres reduced by 0.001 % for the present code, just enough to alleviate numerical difficulties without any noticeable effect on the result F/F_o.

6. Emulsion flow through a randomly packed granular material

In what follows, it is helpful to redefine the velocity and time scales (cf. § 2.1) for an emulsion flow, based on the empirical Carman–Kozeny correlation for a single-phase Newtonian flow through a porous medium. Namely, we scale our continuous-phase (U_C) and drop-phase (U_D) velocities (in the direction opposite to the average pressure gradient $\langle \nabla p\rangle$) with

$$U_{CK} = \frac{|\langle \nabla p\rangle|\widehat{a}^2(1-c_s)^2}{45\mu c_s^2} \tag{6.1}$$

https://doi.org/10.1017/jfm.2013.197 Published online by Cambridge University Press

for each individual RLP configuration with particle volume fraction c_s; time is scaled with $\widehat{a}/U_{CK}$; in (6.1), U_{CK} is simply the dimensional average single-phase flow velocity over the interstitial space between the solid particles, as follows from the Carman–Kozeny correlation. The capillary number is defined as

$$\boldsymbol{Ca} = \frac{\mu U_{CK}}{\sigma}\,\frac{\widetilde{a}^o}{\widehat{a}}, \tag{6.2}$$

using the initial non-deformed radius $\widetilde{a}^o$ of all drops (i.e. prior to breakups, if any). The long-time averages of U_C and U_D, the main quantities of interest, should depend, in general, on both $\boldsymbol{Ca}$ and the size ratio $\widetilde{a}^o/\widehat{a}$ (although the present multidrop–multiparticle simulations are limited to $\widetilde{a}^o/\widehat{a} \approx 0.5$). Only for large enough $\boldsymbol{Ca}$, the long-time behaviour is expected to be insensitive to the initial drop size $\widetilde{a}^o$, once virtually all of the drops fragment repeatedly to the critical sizes with no further breakup. In this range, only $\mu U_{CK}/\sigma$, instead of $\boldsymbol{Ca}$ and $\widetilde{a}^o/\widehat{a}$, would be a significant parameter. However, our simulations, even with massive breakup, still do not approach this limit, as discussed in § 6.2. An additional quantity of interest (which can be extracted from our simulations but is not discussed here) would be the filtration velocity $U_C(1 - c_s - c_d) + U_D c_d$ for the whole emulsion.

6.1. *Tight squeezing, no breakup*

This case is characterized by small $\boldsymbol{Ca}$, when the drops move with high resistance and modest deformation through the material. Figure 5 presents snapshots of an emulsion flow ($\widetilde{N} = 100$ drops in a periodic cell) through a largest-size solid packing ($\widehat{N} = 36$ spheres in a periodic cell) of density $c_s = 0.521$ at capillary number $\boldsymbol{Ca} = 0.006$, with high surface resolution ($\widetilde{N}_\Delta = 6000$ triangular elements on a drop and $\widehat{N}_\Delta = 11\,520$ elements on a solid surface) and a total of 51 000 time steps. The entire simulation, among the most extensive in this work, required several months on a 3.2 GHz core. The average drop motion is roughly along the z-axis shown in figure 5; the last frame shows the drop phase only. The dimples on the drop surfaces seen in figure 5 are due to interactions with the solid spheres not included in the visualization. The initial, artificially made drop configuration (§ 5), with the emulsion concentration $c_{em} = 41.7\,\%$ in the available space, undergoes rapid changes as the drops start moving, with a smoothing effect on the drop shapes (figure 1). By the end of the simulation, each drop typically passes through several constrictions.

For the simulation from figure 5, the dynamics of the instantaneous continuous-phase and drop-phase velocities are presented in figure 6(*a*) (dashed and solid lines, respectively). As expected, the emulsion phases move more slowly through the packed bed than does a single fluid phase (well-described by the Carman–Kozeny correlation). A general observation (confirmed by all other simulations in this work) is that U_D experiences much stronger fluctuations and is, hence, more difficult to average than U_C, especially in the tight-squeezing regime. To monitor the quality of long-time averaging, we work with partial averages

$$\langle U_C\rangle_t = \frac{1}{t}\int_0^t U_C(\tau)\,\mathrm{d}\tau, \quad \langle U_D\rangle_t = \frac{1}{t}\int_0^t U_D(\tau)\,\mathrm{d}\tau. \tag{6.3}$$

For the simulation from figure 5, these quantities are displayed in figure 6(*b*). Convergence to the long-time limit $\langle U\rangle_\infty$ (denoted by $\langle U\rangle$, in what follows) is excellent for the continuous-phase velocity, but somewhat worse for U_D; still, the desired limit $\langle U_D\rangle$ is approached to within $\approx$1 %. Limited $\lambda = 1$ simulations in paper I

https://doi.org/10.1017/jfm.2013.197 Published online by Cambridge University Press

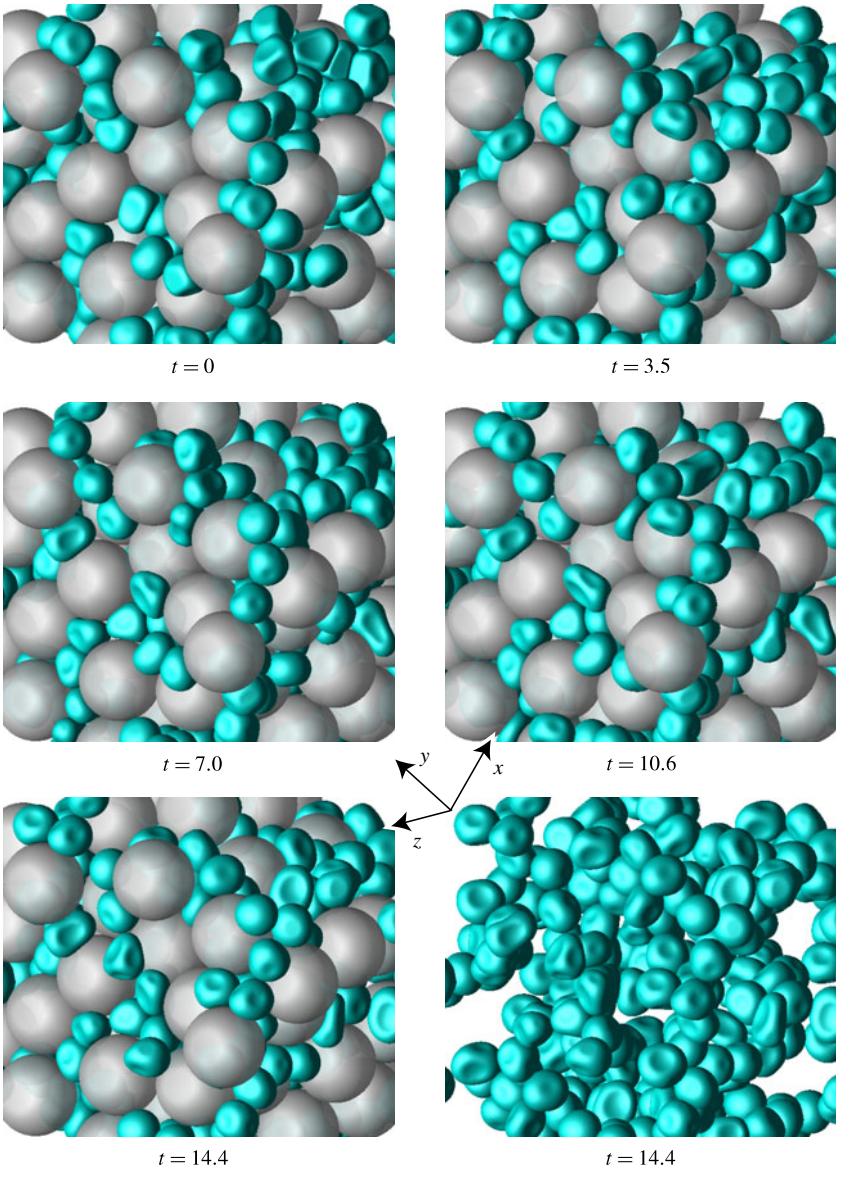


FIGURE 5. Snapshots of the emulsion tightly squeezing through a RLP of solid spheres at $\boldsymbol{Ca} = 0.006$; 100 drops (turquoise) and 36 particles (grey) in a periodic box; the box sides are along the Cartesian axes x, y, z; the average pressure antigradient is along the z-axis; 6000 triangular elements on each drop and 11 500 elements on each solid sphere are used. The last frame shows the drop phase only.

for a smaller system at $\boldsymbol{Ca} = 0.017$ (in the present definition (6.2)) suggested the possibility that the drop phase can move, on the average, faster than the continuous phase. A possible explanation (paper I) is that U_C includes volume averaging of the fluid velocity $\boldsymbol{u}$ outside the drops, with $\boldsymbol{u} \approx 0$ near the solid boundaries, and so $U_C < U_D$ is quite possible. Note that a similar hydrodynamic phenomenon, when red cells move faster than the surrounding fluid, is known for blood flows in capillaries

https://doi.org/10.1017/jfm.2013.197 Published online by Cambridge University Press

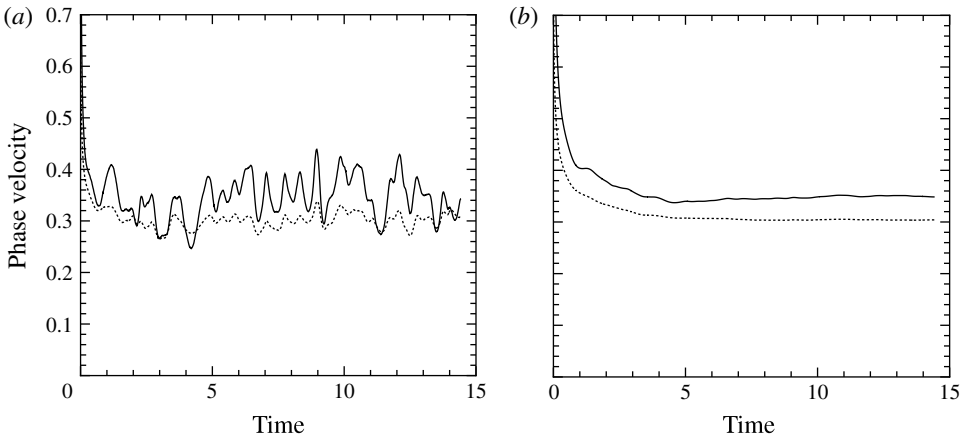


FIGURE 6. (a) Instantaneous and (b) partial time-averaged phase velocities for the simulation from figure 5. Dashed lines: continuous-phase velocity. Solid lines: drop-phase velocity.

(Secomb 1995). It is surprising, though, that in the present simulations the drop phase is observed, on the average, to travel faster than the continuous phase even for tight squeezing conditions $\boldsymbol{Ca} = 0.006$ (figure 6*b*) when the opposite trend could be expected. This seeming paradox is resolved in § 6.3.

Although the drops remain of compact shape and do not break in the tight squeezing regime, this case is numerically very challenging due to strong drop–solid lubrication and large statistical fluctuations, necessitating very high surface resolutions and a very large total number of time steps. The results exhibit undesirable dependence on the initial random configurations of drops, unless long-time averaging is made. Figure 7 presents the convergence analysis at $\boldsymbol{Ca} = 0.006$ for two smaller systems with: (i) $\widehat{N} = 9$, $c_s = 0.548$ complemented by $\widetilde{N} = 25$ drops; and (ii) $\widehat{N} = 18, c_s = 0.498$, $\widetilde{N} = 50$. The drop-surface resolution is fixed at $\widetilde{N}_\Delta = 6000$. The three runs for system (i) presented in figure 7(*a,b*) start from the same random drop configuration (prepared by swelling, § 5) and only differ in the particle-surface resolution $\widehat{N}_\Delta$. For the continuous-phase velocity (figure 7*a*), the long-time averages $\langle U_C\rangle$ with $\widehat{N}_\Delta = 11\,520$ and 15 360 (short-dashed and solid lines, respectively) are in excellent agreement, while the cruder resolution $\widehat{N}_\Delta = 8640$ (the long-dashed line) gives quite inaccurate $\langle U_C\rangle$, with a systematic error $\approx$4.5 %. For the corresponding drop-phase velocities $\langle U_D\rangle_t$ (figure 7*b*), the results with $\widehat{N}_\Delta = 11\,520$ and 15 360 still agree well in the limit $t \to \infty$, within 2 %. The $\widehat{N} = 8640$ results for $\langle U_D\rangle$, however, are still far from statistical convergence (even with 220 000 time steps used in the simulation) and cannot be trusted.

For system (ii), all three runs $\widehat{N}_\Delta = 8640$, 11 520 and 15 360 produce virtually the same long-time average continuous-phase velocity $\langle U_C\rangle$ (figure 7*c*), with excellent statistical convergence. For the long-time average drop-phase velocity $\langle U_D\rangle$ (figure 7*d*), the deviation between the results with $\widehat{N}_\Delta = 11\,520$ and 15 360 (short-dashed and solid lines, respectively) is still acceptable, about 2.5 %. The $\widehat{N}_\Delta = 8640$ results for $\langle U_D\rangle_t$, however, suffer again from insufficient statistical convergence, even after 130 000 time steps used in this simulation; so, the resolution effect on $\langle U_D\rangle$ at $\widehat{N}_\Delta = 8640$ could not

https://doi.org/10.1017/jfm.2013.197 Published online by Cambridge University Press

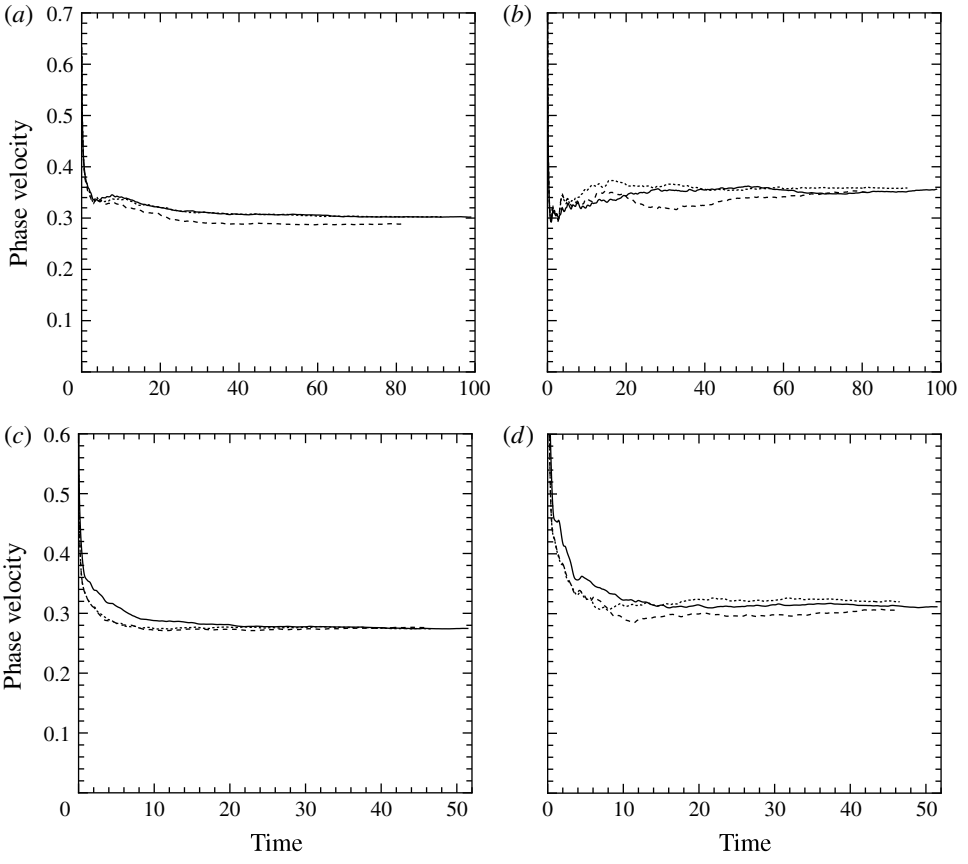


FIGURE 7. Convergence analysis for the time-averaged (*a,c*) continuous-phase velocities $\langle U_C\rangle_t$ and (*b,d*) drop-phase velocities $\langle U_D\rangle_t$ for two systems: (*a,b*) $\widehat{N} = 9$ particles, $\widetilde{N} = 25$ drops in a periodic cell; (c,d) $\widehat{N} = 18$, $\widetilde{N} = 50$. Long-dashed lines: $\widehat{N}_\Delta = 8640$ elements per solid surface; short-dashed lines: $\widehat{N}_\Delta = 11\,520$; solid lines: $\widehat{N}_\Delta = 15\,360$. Resolution $\widetilde{N}_\Delta = 6000$ per drop surface is used in all the runs.

be reliably assessed. In figure 7(*c,d*), the runs $\widehat{N}_\Delta = 8600$ and 11 500 start from the same random drop configuration. For $\widehat{N} = 15\,000$, though, we have chosen a different initial drop arrangement (using a different seed for random numbers in Monte Carlo generation of the drop configuration prior to swelling, see § 5 and paper I). So, the agreement between the solid and short-dashed lines in figure 7(*c,d*) at $t \to \infty$ also indicates independence of the results $\langle U_C\rangle$ and $\langle U_D\rangle$ from initial conditions, once the triangulation and statistical errors are eliminated. Using very high solid-surface resolutions in the present, tight-squeezing simulations is imperative not only as a matter of accuracy. With 'low' resolution $\widehat{N}_\Delta = 2160$, we could not obtain any results (even for less tight squeezing $\boldsymbol{Ca} = 0.009$); such runs invariably crash at short times due to numerical errors and associated catastrophic high-curvature development on some drop surfaces.

To probe the drop-surface resolution effect in tight-squeezing conditions, the $\widetilde{N}_\Delta = 6000$, $\widehat{N} = 11\,500$ run (represented by the short-dashed lines in figure 7*c,d*) was

https://doi.org/10.1017/jfm.2013.197 Published online by Cambridge University Press

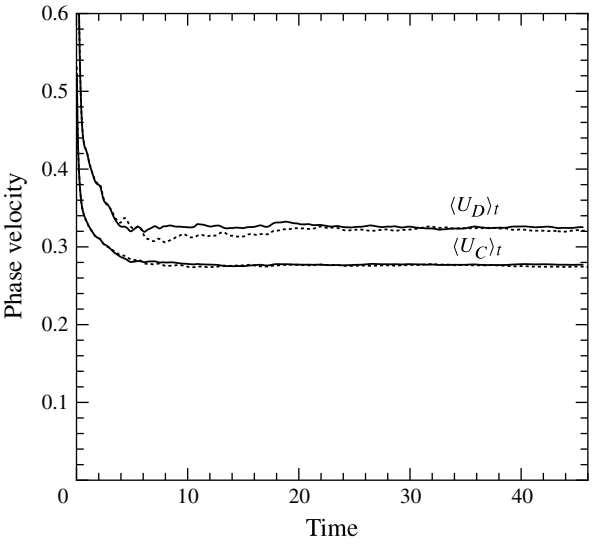


FIGURE 8. The effect of drop surface resolution on the time-averaged phase velocities in the tight-squeezing regime ($\boldsymbol{Ca} = 0.006$) for the system $\widehat{N} = 18$, $\widetilde{N} = 50$, $\widehat{N}_\Delta = 11\,520$. The short-dashed lines (taken from figure 7*c,d*) are for $\widetilde{N}_\Delta = 6000$ elements per drop surface; the solid lines are for $\widetilde{N}_\Delta = 3840$.

repeated using cruder resolution $\widetilde{N}_\Delta = 3840$. The effect is quite small (figure 8), being about 1 % for $\langle U_D\rangle$ and negligible for $\langle U_C\rangle$; unexpectedly, it is far more important to resolve solid surfaces than drop surfaces in the tight-squeezing regime.

All of the simulations for figures 5–8 employ geometric barriers, to keep drop-surface nodes a distance of at least $0.009\widehat{a}$ away from the solid spheres and a distance of at least $0.001\widehat{a}$ away from other drop surfaces, as detailed in § 5. However, only an extremely small portion of the drop surface nodes requires such corrections. For example, in the medium-resolution simulations ($\widehat{N}_\Delta = 11\,500$) for figure 7(*a,b*), only 17 nodes, on the average, out of total 75 000 on $\widetilde{S}_\alpha$, participate in the drop–solid distance correction at each time step. As the solid resolution $\widehat{N}_\Delta$ in figure 7(*a,b*) is increased from 8600 to 15 400, the average magnitude of the drop–solid distance correction per time step falls several fold. More nodes need the drop–drop distance correction (obviously, because of less lubrication between the drops than between the drops and solids); still, only about 0.2 % of the nodes on $\widetilde{S}_\alpha$ required such a correction at each time step in the $\widetilde{N}_\Delta = 3840$ calculation for figure 8. As the drop surface resolution is increased to $\widetilde{N}_\Delta = 6000$, the average drop–drop distance correction per time step falls more than two-fold. It is important to emphasize, as in paper I, that imposing the geometrical barriers, with negligible effect on the global quantities of interest ($\langle U_C\rangle$ and $\langle U_D\rangle$), is only acceptable because lubrication is 'almost resolved' in the present calculations due to high resolutions and advanced desingularization schemes.

As the capillary number is increased, making it easier for drops to squeeze, the solid surface resolution requirements become less severe. For $\boldsymbol{Ca} \geqslant 0.009$, it was sufficient to use $\widehat{N}_\Delta = 8640$.

https://doi.org/10.1017/jfm.2013.197 Published online by Cambridge University Press

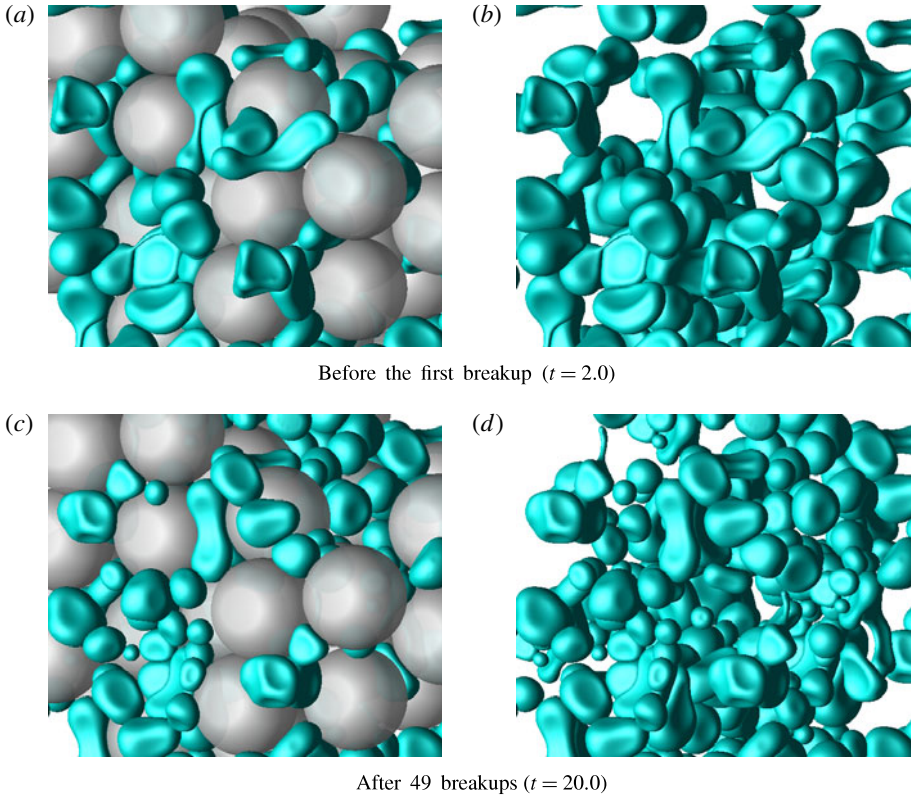


FIGURE 9. Snapshots of the $\boldsymbol{Ca} = 0.02$ emulsion flow through a RLP of solid spheres with multiple drop breakup; 18 particles (grey) with $c_s = 0.527$ and (initially) 50 drops (turquoise) in a periodic box; 6000 elements per primary drop/fragment and 8600 elements per solid surface. Left images: the drop and continuous phases. Right images: the drop phase only. The directions of Cartesian axes (not shown) are the same as in figure 5.

6.2. *Larger* $\boldsymbol{Ca}$*: massive drop breakup*

As the capillary number is increased to $\boldsymbol{Ca} = 0.02$, massive drop breakup is observed. Figure 9 gives an example of emulsion flow with initially $\widetilde{N}^o = 50$ drops through a RLP of $\widehat{N} = 18$ particles with solid volume fraction $c_s = 0.527$ (and emulsion concentration $c_{em} = 0.422$ in the available space). The top two snapshots are taken just before the first breakup, the bottom two after 49 breakups. The left images show both the particles and drops, while the right images include the drop phase only. The simulation was terminated after 62 breakups. Of all of these breakups, only 38 are primary breakups, so 12 drops still remain unfragmented by the end of the simulation (and, hence, the initial drop size $\widetilde{a}^o$ still affects the long-time behaviour at this $\boldsymbol{Ca} = 0.02$). In addition, this run included just a few cases of tip streaming from secondary drops, with insignificant satellites neglected in further simulation (as detailed in § 4). The whole run took 93 000 time steps; this very large number of steps is due to the high resolution ($\widetilde{N}_\Delta = 6000$ elements per drop surface) and significant time step reduction in the vicinity of each breakup, when high curvatures develop. Figure 10 shows examples of primary breakup in this simulation, with subsequent fragmentation (performed as detailed in § 4); the drop shapes are quite complex

https://doi.org/10.1017/jfm.2013.197 Published online by Cambridge University Press

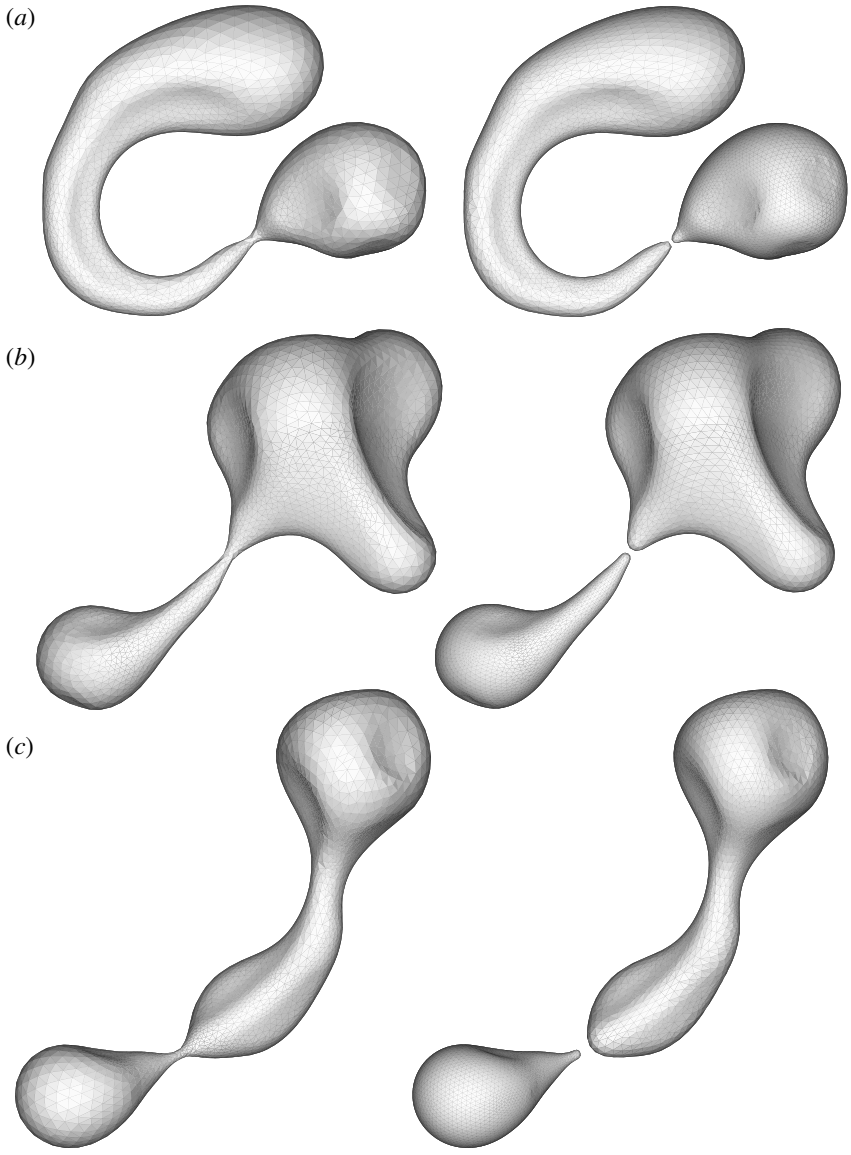


FIGURE 10. Three examples of primary drop breakup at $t = 2.922$, 2.925 and 14.65 (*a–c*, respectively, with a different view in each case) in the simulation from figure 9. The right images show fragmented and remeshed drop shapes after each breakup. At $t = 14.65$, the secondary breakup development is also seen.

at breakup, due to interaction with nearby solid particles. Each fragment is still discretized with 6000 elements (which is only a slightly non-optimal strategy, as it turns out).

The radius $\widetilde{a}$ of a deformed drop is defined as the radius of the spherical drop with the same volume. Figure 11 shows the evolution of the average drop radius (relative to the initial radius $\widetilde{a}^o$) due to breakups in the simulation from figure 9. The number of drops, although increased to 112 by breakups, was not sufficient to plot a smooth

https://doi.org/10.1017/jfm.2013.197 Published online by Cambridge University Press

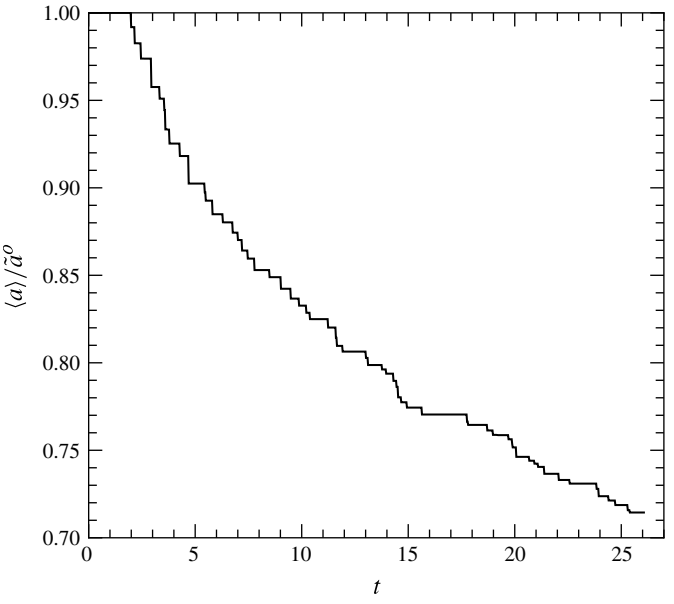


FIGURE 11. Evolution of the average drop radius (relative to the initial radius) due to breakups in the simulation from figure 9.

size distribution histogram. However, it is obvious from figure 11 that the average drop size is significantly reduced and continues to decrease (mostly due to secondary breakups), so the size distribution is still far from steady state. In this connection, it is particularly interesting to explore the effect of breakups on the phase velocities, the main quantities of interest. For the simulation from figure 9, the trajectories of the instantaneous phase velocities, U_C and U_D, are displayed in figure 12(*a*); the vertical bars denote all breakup moments, some (nearly) indistinguishable. As for the tight squeezing regime (§ 6.1), the drop-phase velocity U_D has much stronger dispersion than the continuous-phase velocity U_C. There are no noticeable jumps in $U_C(t)$ or $U_D(t)$ at breakup moments. It would be unnecessary, therefore, in our simulations to take each breakup to a more advanced stage, with a thinner neck, before fragmentation. Such a refinement would just complicate and slow down calculations significantly. Another justification comes from local, self-similar axisymmetrical solutions for neck thinning near breakup (see Eggers 1997 and references therein). These solutions predict the ultimate pinch-off to be reached in a finite time (with the neck radius becoming proportional to the time increment $t_{br} - t$ to breakup); so, the last stage with very small neck thickness is not critical for global breakup simulations.

For the instantaneous phase velocities from figure 12(*a*), the corresponding partial time averages $\langle U_C \rangle_t$ and $\langle U_D \rangle_t$ are presented in figure 12(*b*) by solid lines. Even though massive drop breakup is far from over and the drop-size distribution continues to evolve, a remarkable and unexpected conclusion from figure 12(*b*) is that U_C and U_D approach a statistical steady state much faster than does the size distribution. So, if determining the steady-state phase velocities $\langle U_C \rangle$ and $\langle U_D \rangle$ is the only goal, then the simulation can be limited to an initial stage, with a relatively small portion of breakups: a great simplification to the otherwise formidable problem.

https://doi.org/10.1017/jfm.2013.197 Published online by Cambridge University Press

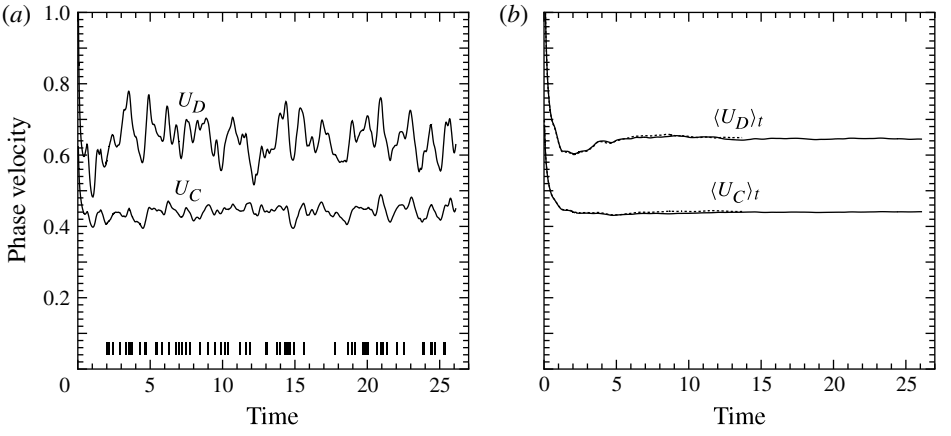


FIGURE 12. (a) Instantaneous and (b) partially time-averaged phase velocities for the simulation from figure 9 (solid lines); the breakup moments for this simulation are marked in (a) by vertical bars. The dashed lines in (b) are for a similar simulation, but with cruder drop surface resolution (3840 elements on each primary drop and fragment).

The dashed lines in figure 12(*b*) are for a similar simulation (starting from the same random initial configuration of drops), just using a cruder resolution $\widetilde{N}_\Delta = 3840$ on all primary drops and fragments. As in the other simulations (§ 6.1), convergence analysis for the instantaneous velocities $U_C(t)$ and $U_D(t)$ is not very useful in the present context, since the trajectories of U_C and U_D inevitably randomize after a short simulation time. More relevant, partial averages $\langle U_C\rangle_t$ and $\langle U_D\rangle_t$ in figure 12(*b*) show excellent convergence with respect to drop-surface resolution, as $t \to \infty$. Using even cruder resolutions than $\widetilde{N}_\Delta = 3840$, however, was observed to create difficulties with control of high surface curvatures, and was not pursued in our systematic runs. Note also that the neck thickness and the initial fragment-to-fragment distances at each breakup in the $\widetilde{N}_\Delta = 3840$ run are generally quite different from those for $\widetilde{N}_\Delta = 6000$. So, the convergence of the results in figure 12(*b*) is another indication that these details of drop fragmentation do not have any appreciable effect on the quantities of interest ($\langle U_C\rangle$ and $\langle U_D\rangle$) in our simulations.

In the massive-breakup regime, the steady-state drop-phase velocity is much larger than the continuous-phase velocity (figure 12*b*). To check the universality of this and other conclusions above, we studied the emulsion flow with initially $\widetilde{N}^o = 50$ drops through a different RLP of solid spheres with $c_s = 0.523$. Again, multiple breakups are observed, with the breakup moments marked in figure 13(*a*) by vertical bars. The instantaneous velocities $U_C(t)$ and $U_D(t)$ (figure 13*a*) do not reveal any systematic effects of drop breakup beyond the initial stage (after primary breakups are mostly completed). The corresponding partial averages (solid lines in figure 13*b*) show a very slight upward trend in U_D, necessitating larger times for averaging (compared with figure 12*b*), but this trend is not necessarily associated with breakups (cf. tight-squeezing simulations in § 6.1 without breakups). In any case, the long-time averages $\langle U_C\rangle$ and $\langle U_D\rangle$ can still be well-estimated from the initial stage of the simulation, when the process of massive drop breakup is still far from abating. It was particularly intriguing to explore the effect of the initial conditions by generating a different random drop configuration inside the granular material at $t = 0$, since it results in a

https://doi.org/10.1017/jfm.2013.197 Published online by Cambridge University Press

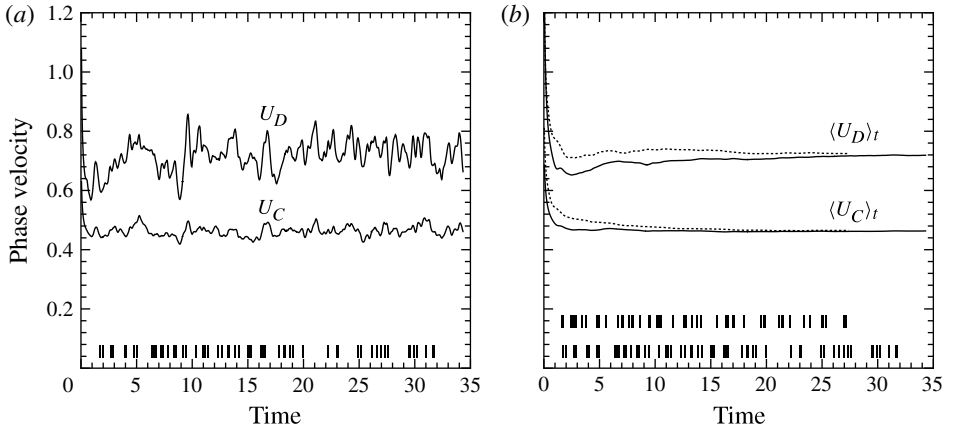


FIGURE 13. (a) Instantaneous and (b) partially time-averaged phase velocities for the $\boldsymbol{Ca} = 0.02$ emulsion flow of initially $\widetilde{N}^o = 50$ drops through a RLP of $\widehat{N} = 18$ solid spheres with $c_s = 0.523$ (the particle configuration different from that in figures 9–12). The solid lines and the lower rows of breakup moments in (a) and (b) correspond to one random choice of initial drop locations. The dashed lines and the upper row of breakup moments in (b) are for a different random set of initial drop locations.

totally different history of subsequent breakups from the onset, and the question is whether the same steady state for U_C and U_D can be reached. These additional results are shown in figure 13(*b*) for the partial averages by dashed lines, with breakup times in the top row of vertical bars. Again, the steady-state phase velocities can be well estimated from the initial stage when breakups are still far from over. More accurate results in the longer time range show virtually no effect of the initial conditions on $\langle U_C \rangle$ and $\langle U_D \rangle$.

6.3. *Ensemble- and time-averaged results for the phase permeabilities*

Figure 14(*a,b*) summarize our calculations of the long-time-averaged continuous-phase ($\langle U_C \rangle$) and drop-phase ($\langle U_D \rangle$) velocities for the emulsion flow through many RLPs. Ten RLPs of solid spheres were used for the smallest systems (open circles: $\widehat{N} = 9$ particles and (initially) $\widetilde{N}^o = 25$ drops in the periodic cell) for all the capillary numbers shown. Nine RLP arrays were employed for medium-size systems (plus symbols: $\widehat{N} = 18$, $\widetilde{N}^o = 50$), excluding $\boldsymbol{Ca} = 0.015$. Open diamonds in figure 14(*a,b*) are for the largest systems ($\widetilde{N}^o = 100$ drops) using eight RLP configurations with $\widehat{N} = 36$ spheres, at $\boldsymbol{Ca} = 0.006$ and 0.015 only. As discussed in § 5, the particle volume fraction varies somewhat in these packings (while the drop volume fraction in the entire space is fixed at 20 %), causing slight variations in the (initial) drop-to-particle size ratio $\widetilde{a}^o/\widehat{a}$ from packing-to-packing, and more significant variations of the emulsion concentration c_{em} in the available space between the solids. For small, medium-size and largest systems, the average size ratio $\widetilde{a}^o/\widehat{a}$ is 0.519, 0.518, and 0.516, respectively; the average emulsion concentration c_{em} is 0.414, 0.416 and 0.421, respectively. At $\boldsymbol{Ca} = 0.006$ and 0.009, drop breakup was never observed (so that $\widetilde{a}^o = \widetilde{a}$); only very rare, isolated breakups were encountered at $\boldsymbol{Ca} = 0.012$, but massive breakups occurred in the simulations with $\boldsymbol{Ca} = 0.02$ (which, remarkably, did not preclude time averaging). As discussed in §§ 6.1 and 6.2, the total number of time

https://doi.org/10.1017/jfm.2013.197 Published online by Cambridge University Press

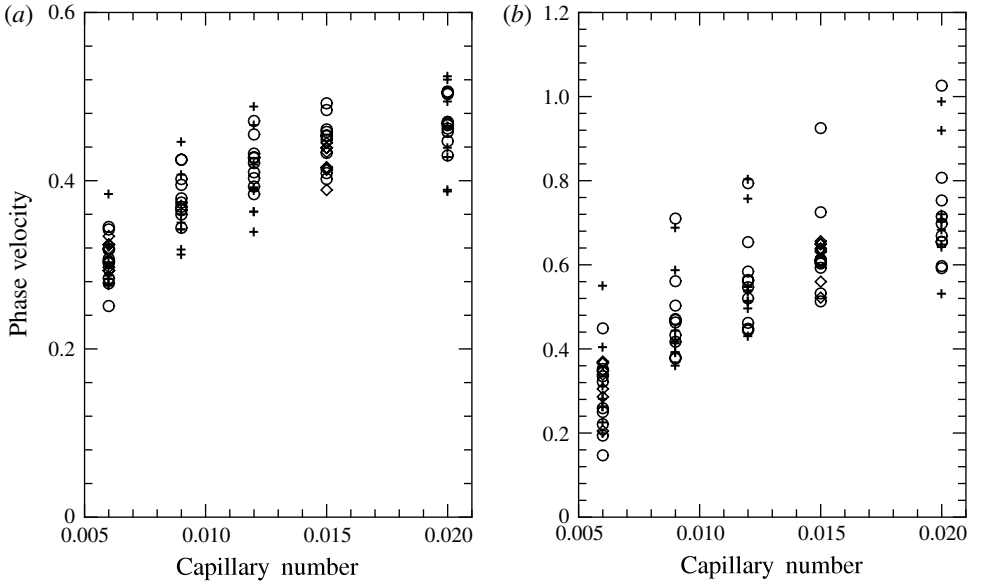


FIGURE 14. Long-time averages of (a) continuous-phase and (b) drop-phase velocities for the emulsion flow through different RLPs of a granular material. Open circles: $\widehat{N} = 9$ particles and (initially) $\widetilde{N}^o = 25$ drops in a periodic cell. Plus symbols: $\widehat{N} = 18$, $\widetilde{N}^o = 50$. Open diamonds: $\widehat{N} = 36$, $\widetilde{N}^o = 100$. The (initial) drop-to-particle size ratio is $\approx$0.5, and emulsion concentration in the available space is $\approx$40 %.

steps and the surface resolution (especially on solid spheres for tight squeezing) had to be very high in each run for figure 14, contributing to the difficult challenge of such simulations.

Another severe difficulty, apparent from figure 14(*a,b*), is a very large dispersion of the phase velocities, especially $\langle U_D \rangle$, for individual runs, necessitating additional, ensemble averaging over many RLP configurations to obtain meaningful results. Instead of fixing the drop-phase volume fraction in the entire space, a possibly better strategy could be fixing the emulsion concentration c_{em} in the available space between solid particles, in order to reduce the dispersion. This option, though, was not pursued in our simulations, and the degree of improvement it can provide is unclear. Difficulties with ensemble averaging still could not be avoided. For example, one medium-size particle packing ($\widehat{N} = 18$), with the volume fraction $c_s = 0.540$, produced $\langle U_C \rangle = 0.39$, $\langle U_D \rangle = 0.55$ at $\boldsymbol{Ca} = 0.006$, and $\langle U_C \rangle = 0.52$, $\langle U_D \rangle = 0.99$ at $\boldsymbol{Ca} = 0.02$. A different medium-size packing, with nearly the same particle volume fraction $c_s = 0.527$, yields, nevertheless, very different results: $\langle U_C \rangle = 0.31$, $\langle U_D \rangle = 0.29$ at $\boldsymbol{Ca} = 0.006$ and $\langle U_C \rangle = 0.44$, $\langle U_D \rangle = 0.65$ at $\boldsymbol{Ca} = 0.02$. So, even at the same emulsion concentration $c_{em} = c_d/(1 - c_s)$, the particle arrangement can have a strong effect on the drop-phase velocity $\langle U_D \rangle$, for the system sizes that we have been able to simulate.

The results of ensemble averaging ($\langle \overline{U}_C \rangle$, $\langle \overline{U}_D \rangle$) of the continuous and drop-phase velocities from figure 14 are shown in figure 15(*a,b*) for three system sizes. Although some statistical errors are still present in figure 15, the ensemble-averaged results are much better-behaved than those for individual packings, have a reasonably

https://doi.org/10.1017/jfm.2013.197 Published online by Cambridge University Press

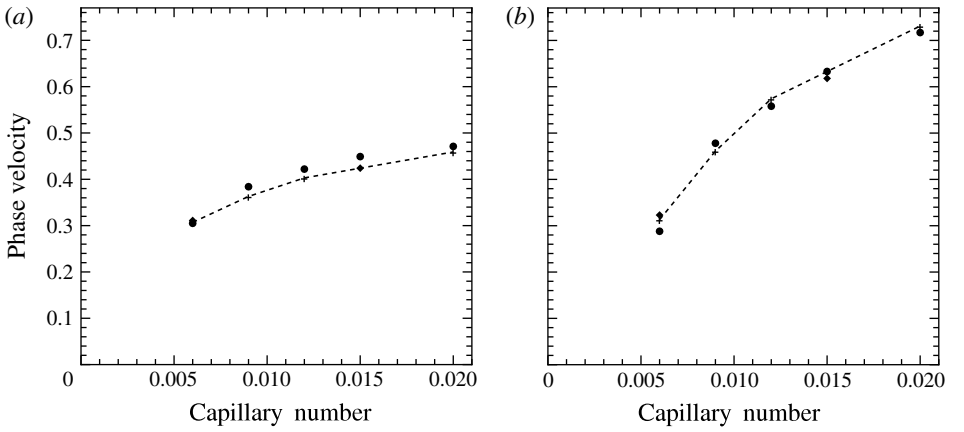


FIGURE 15. Ensemble and long-time averages of (a) continuous-phase and (b) drop-phase velocities for the emulsion flow through RLPs of spheres, at the initial drop-to-particle size ratio of ≈0.52 and the emulsion concentration of 41–42 %. Three system sizes: $\widehat{N} = 9$, $\widetilde{N}^o = 25$ (solid circles), $\widehat{N} = 18$, $\widetilde{N}^o = 50$ (plus symbols) and $\widehat{N} = 36$, $\widetilde{N}^o = 100$ (solid diamonds).

weak dependence on the system size and clearly show the physical trends of the phase velocities. Side-by-side comparison between figure 15(*a,b*) shows that strongly deformable drops ($\boldsymbol{Ca} = 0.02$) move, on the average, much faster than the continuous phase. As $\boldsymbol{Ca}$ is reduced and the tight squeezing regime is approached, though, the drop-phase velocity falls rapidly and approaches the continuous-phase velocity at $\boldsymbol{Ca} = 0.006$. Further decrease in the capillary number would finally make the drops travel slower than the continuous phase. This range, however, would be extremely difficult to simulate with confidence in the present problem, due to severe convergence difficulties and exorbitant computational costs. At any rate, the results in figure 15(*b*) point to the existence of the critical capillary number $\boldsymbol{Ca}_{crit}$ (believed to be 0.003–0.004 in the large-size limit $\widehat{N}$, $\widetilde{N}^o \to \infty$), at which the drop-phase flow effectively stops, $\langle \overline{U}_D \rangle = 0$. No such critical threshold exists for the continuous-phase velocity $\langle \overline{U}_C \rangle$ (cf. figure 15*a,b*); obviously, when the drops are trapped in the pores, the continuous phase still has room to flow around the drops. The fact that the drops do not move slower than the suspending fluid until $\boldsymbol{Ca}_{crit}$ is closely approached, may be due to $\lambda = 1$ in the present calculations. Simulations of paper I for the flow of $\lambda = 4$ drops through one small-size packing of solid spheres showed, in contrast, that the drops, on the average, can move slower than the suspending fluid even away from the tight-squeezing regime, with much less numerical difficulty.

Another observation from our analysis, which is quite unexpected and may be practically useful, is that the capillary number to characterize the steady-state permeabilities in the emulsion flows with multiple drop breakups, should be based on the initial drop size (or size distribution) prior to breakups, not on the subsequent (and complex) evolution of the size distribution.

7. Single-drop migration through a packed granular material

In addition to the flow of a concentrated emulsion ($c_{em} \sim 40\,\%$) through a granular material with finite drop-to-particle size ratios $\widetilde{a}^o/\widehat{a} \sim 0.5$ considered in § 6, it is

https://doi.org/10.1017/jfm.2013.197 Published online by Cambridge University Press

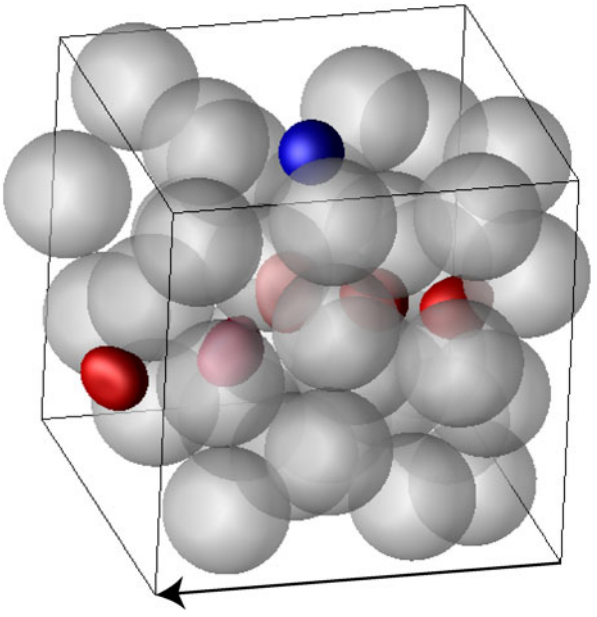


FIGURE 16. Single-drop migration through a RLP of 36 particles (grey) in a periodic cell (shown as a box) with $c_s = 0.536$, drop-to-particle size ratio of 0.512 and capillary number $\boldsymbol{Ca} = 0.015$. The arrow shows the average pressure antigradient direction. The initial drop location is coloured blue. The red images are the drop positions along the attractor ('optimal path') attained at large times.

interesting to explore the opposite limit of low emulsion concentrations (and still the same size ratios, so that the emulsion cannot be treated as effectively single phase). With the present code, a straightforward way to approach this limit is by considering just $\widetilde{N} = 1$ drop in the periodic cell (provided there are no breakups, see below). To delineate deep distinctions between the two cases, we consider herein the flow through just one RLP configuration of $\widehat{N} = 36$ solid spheres with $c_s = 0.536$ and mostly the size ratio of $\widetilde{a}^o/\widehat{a} = 0.512$, producing a dilute emulsion concentration of $c_{em} = 0.43\,\%$ at $\widetilde{N} = 1$ in the available space. The $\boldsymbol{Ca} = 0.015$ simulation is presented in figure 16, with the corresponding drop-phase velocity trajectory in figure 17(*a*); the continuous-phase velocity (not shown) is almost unaffected by the presence of the drop and stays very close to 1.11. Only the particles with centres in the periodic box $[0, 1)^3$ are shown in figure 16; the direction of $-\langle\boldsymbol{\nabla} p\rangle$ (i.e. of the average drop motion) is marked by an arrow; the initial drop position (at $t = 0$) is coloured blue. At $t > 0$, the drop first squeezes with high resistance and low velocity, but eventually finds a much easier way ('optimal path') to move through the material, and the drop velocity attains a time-periodic regime (figure 17*a*). This optimal path is a narrow channel roughly along $\langle\boldsymbol{\nabla} p\rangle$, between the solid particles; the drop periodically leaves the channel through the side of the periodic box, only to enter it through the other side. The drop positions along the optimal path are shown as red-coloured images in figure 16, at time moments designated by solid circles in figure 17(*a*); the initial drop position is quite away from the optimal path.

For comparison, figure 17(*b*) presents the drop-phase velocity trajectory for the flow of a concentrated emulsion ($\widetilde{N} = 100$ drops initially, $c_{em} = 43\,\%$) through the same

https://doi.org/10.1017/jfm.2013.197 Published online by Cambridge University Press

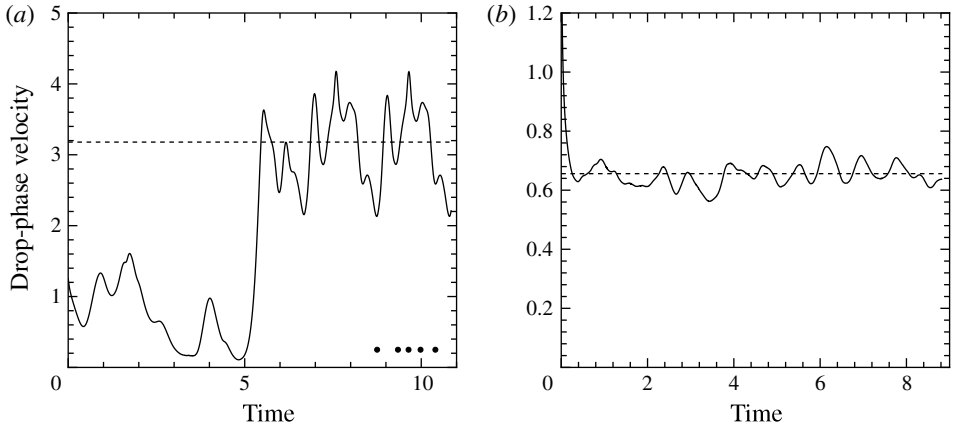


FIGURE 17. Comparison between the drop-phase velocity trajectories $U_D(t)$ for (a) single-drop motion (from figure 16) and (b) concentrated emulsion flow (100 drops in a cell) through the same packing of 36 particles at the same $\boldsymbol{Ca} = 0.015$ and size ratio of 0.512. The dashed lines are for long-time averages. The time moments marked with circles in (a) correspond to the drop locations in figure 16 (shown in red) along the optimal path.

particle packing, and at the same values of $\boldsymbol{Ca}$ and $\widetilde{a}^o/\widehat{a}$; the run in figure 17($b$) is one of those used for ensemble averaging in figure 15. The first distinction between figure 17(a,b) is that the velocity trajectory reaches a periodic regime for the dilute case, but remains stochastic for the concentrated emulsion in a similar time range. Second, solitary drops travelling through a granular material are much less prone to breakup than the drops in a concentrated emulsion flow (at the same $\boldsymbol{Ca}$ and $\widetilde{a}^o/\widehat{a}$). Indeed, in the simulation for figures 16 and 17(a), the drop does not break at all and remains compact, while in the run for figure 17(b) 12 breakups were encountered. Finally, solitary drops move, on average, several times faster than the drops in the concentrated emulsion do (cf. the dashed lines in figure 17a,b). The obvious explanation is that the concentrated emulsion as a whole acts like a more viscous fluid (even though the concept of treating the emulsion as an effective medium is generally deficient for finite size ratios $\widetilde{a}/\widehat{a}$).

It is understandable that the existence of the optimal path and the time-periodic regime in our $\widetilde{N} = 1$ simulation is due to the periodic boundary conditions imposed on the random packing of solid particles. Presumably, for $\widetilde{N} = 1$ and much larger particle packings (hundreds or thousands of spheres, with the same size ratio $\widetilde{a}/\widehat{a}$), the long-time periodic regime would still exist, but the period T would be far too large to be reached in any feasible simulations. Under such conditions, the system trajectory should look stochastic on much smaller time scales $t \ll T$, with an appropriate interval $[0, t]$ for averaging. The present work offers a more economical alternative, with time averaging over the full period of motion, T, for small and moderate-size random packings (provided that additional ensemble averaging over different bed realizations is made). It is unlikely that using much larger $\widehat{N}$, as described above, could have a strong effect on the results, owing to the absence of long-range correlations.

The simulation in figures 16 and 17(a) was repeated for different $\boldsymbol{Ca}$, and in each case the periodic regime was found to be unique, i.e. independent of the initial conditions. In figure 18(a) for $\boldsymbol{Ca} = 0.006$, the short-dashed line is for a favourable initial drop location, so the periodic regime (shown by the bold line) is reached

https://doi.org/10.1017/jfm.2013.197 Published online by Cambridge University Press

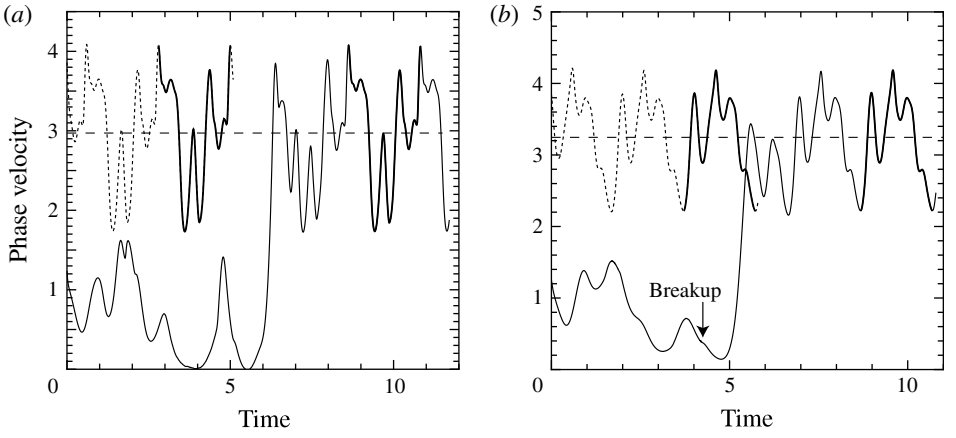


FIGURE 18. The velocity of a single drop with size ratio $\widetilde{a}^o/\widehat{a} = 0.512$ travelling through the packing of 36 solid particles (figure 16) at (*a*) $\boldsymbol{Ca} = 0.006$ and (*b*) $\boldsymbol{Ca} = 0.02$. The short-dashed lines are for a favourable initial drop location, with a quick approach to the periodic cycle (marked bold). The thin solid lines are for unfavourable initial conditions. Averages over the periodic cycle are represented by long-dashed lines. In (*b*), the approach to the periodic regime from the unfavourable initial location is accompanied by a satellite drop formation.

quickly. For a different, unfavourable initial location (the thin solid line), the drop goes through two stages of very tight squeezing, with the velocity U_D decreasing to nearly zero values, until it eventually finds the optimal path with the periodic $U_D(t)$. The two periodic regimes, marked bold in figure 18(*a*), are virtually indistinguishable to within an insignificant time shift. Ergodic difficulties should be expected, though, for sufficiently small $\boldsymbol{Ca} < 0.006$ when the drop could be trapped starting from unfavourable initial conditions; this case is not addressed herein.

For $\boldsymbol{Ca} = 0.02$ (figure 18*b*), the short-dashed line corresponds, again, to the favourable initial drop location, with the periodic regime (the bold line) quickly attained. The run from the unfavourable initial location (the thin solid line), though, is complicated by drop breakup with a satellite formation (figure 19). The satellite volume is only 1 % of that for the parent drop, so the satellite drop was safely discarded to complete this $\widetilde{N} = 1$ calculation, until the optimal path is found. The two established periodic regimes in figure 18(*b*) (bold lines) are indistinguishable, to within a time shift. So, in a broad range of parameters, with or without breakup, the long-time periodic regime is found to be insensitive to the initial conditions. Note also that the insignificant volume of the satellite drop in figure 19 is another indication that drops are much more prone to breakup in the concentrated emulsion flow; indeed, at this $\boldsymbol{Ca} = 0.02$, massive drop breakup (with fragments typically of comparable volumes) was observed in § 6.2.

Unlike for concentrated emulsions (§ 6.3), the time-averaged velocity $\langle U_D \rangle$ for solitary drops is a weak function of the capillary number. As $\boldsymbol{Ca}$ is increased from 0.006 to 0.02, $\langle U_D \rangle$ rises only by 9 % (figure 18*a,b*).

The size ratio $\widetilde{a}^o/\widehat{a}$ has a stronger effect on the behaviour of solitary drops, which we studied at $\boldsymbol{Ca} = 0.02$. When $\widetilde{a}^o/\widehat{a}$ is halved, the periodic regime is still reached (without breakup), but after much longer relaxation, and it has much wider dispersion for $\widetilde{a}/\widehat{a} = 0.256$ (figure 20) than for $\widetilde{a}^o/\widehat{a} = 0.512$ (figure 18*b*). For $\widetilde{a}^o/\widehat{a} = 0.512$,

https://doi.org/10.1017/jfm.2013.197 Published online by Cambridge University Press

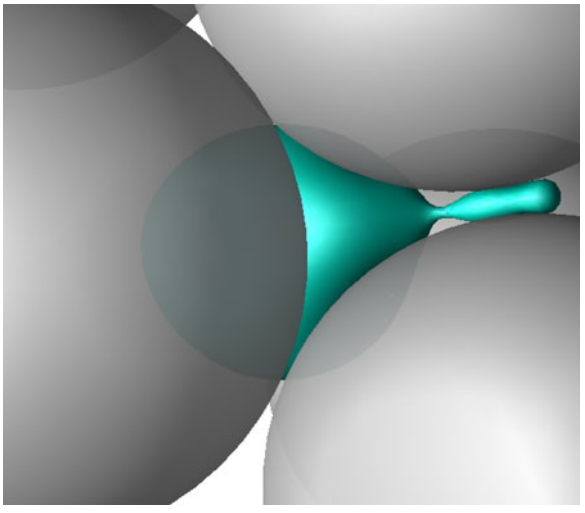


FIGURE 19. Satellite drop formation in the run from figure 18(*b*), starting from the unfavourable initial drop location.

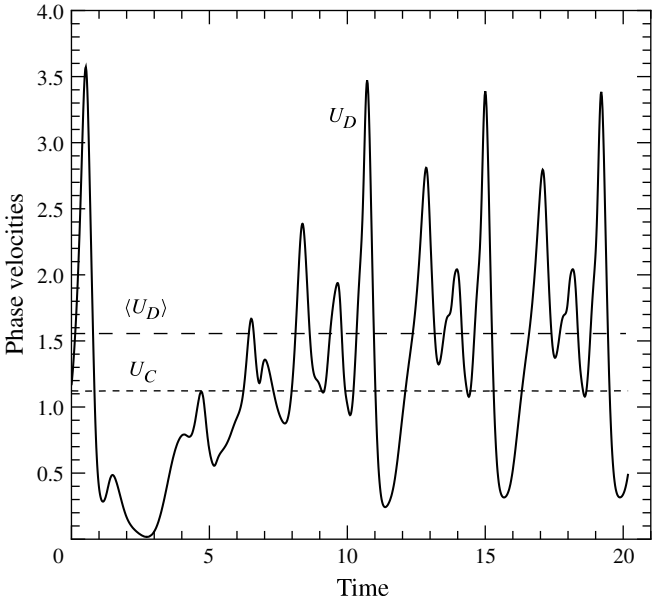


FIGURE 20. Phase velocities for a single-drop motion through the particle packing of figure 16 at $\boldsymbol{Ca} = 0.02$ and small size ratio $\widetilde{a}^o/\widehat{a} = 0.256$. The long-dashed line is for the average drop velocity. The short-dashed line is for the carrier fluid (almost unaffected by the drop).

the drop phase moves, on the average, 2.94 times faster than the continuous phase (figure 18*b*); when $\widetilde{a}/\widehat{a} = 0.256$, the ratio of the velocities $\langle U_D \rangle / U_C$ decreases to 1.39. There is a wide range of parameters, therefore, where large solitary drops travel more efficiently through the granular material than small drops do.

https://doi.org/10.1017/jfm.2013.197 Published online by Cambridge University Press

As $\widetilde{a}/\widehat{a} \to 0$, the drop is able to sweep the entire interstitial space between the solid particles in one periodic cycle, and time averaging of the drop velocity becomes equivalent to volume averaging of the local fluid velocity (for pure liquid) over the interstitial space. This is the way to approach the expected limit $\langle U_D \rangle = U_C$ as $\widetilde{a}/\widehat{a} \to 0$.

8. Conclusions

Pressure-driven, low-Reynolds-number flow of highly concentrated emulsions of deformable drops through a randomly-packed granular material has been studied from first principles by rigorous three-dimensional multidrop–multiparticle simulations. This problem is relevant to many processes in nature and engineering, including oil recovery from underground reservoirs. The drops are comparable in size with the granular particles (and, hence, much larger than the pores of the interstitial space), so the emulsion cannot be treated as a single phase. The drop-phase permeability is different from that for the carrier fluid; squeezing requires significant drop deformation and can meet much resistance, depending on the capillary number. For subcritical conditions, drops may be trapped in the pores by capillary forces. The process is also severely complicated by the possibility of multiple drop breakups. The granular material skeleton is realistically modelled as RLP of many frictional particles in a periodic box in mechanical equilibrium (against the confining pressure, if applied). A novel, isotropic algorithm developed herein for RLP assumes absolutely rigid, absolutely rough monodisperse spheres, has no free parameters, and produces results in attractive agreement with the experiments of Onoda & Liniger (1990), when extrapolated to large systems.

Very challenging flow simulations for many deformable drops squeezing through the network of solid spheres are performed by a multipole-accelerated BI algorithm, with two-orders-of-magnitude gain over the standard BI coding at each time step to facilitate such calculations. The flow code is a significant extension of the algorithm originally developed for this problem in paper I. The major improvement is a robust mesh control scheme for drop surface triangulations. This scheme is a combination of 'passive mesh stabilization', active mesh restructuring and topological mesh transformations (node reconnections only), with new forms of 'kinetic' and 'potential' mesh-energy functions moderately adaptive to local curvature. The mesh control is complemented by a novel drop fragmentation algorithm to continue simulations after each breakup. A unique feature of this algorithm is flexible (and logically simple) control of fragment resolutions, since the meshes on fragments are built from scratch, with no relation to the parent drop meshing. These mesh tools have allowed for reliable long-time simulations, with drops passing the constrictions multiple times and drop shapes of virtually any complexity encountered in the emulsion flow through a randomly packed granular material; a total of several hundred primary and secondary drop breakups were simulated. Among other significant improvements to the code is the new integration scheme over spherical solid surfaces with unstructured triangulations, which greatly improves the accuracy for the continuous-phase permeability. Still, an individual run may take up to $O(10^5)$ time steps for reliable averaging of the phase permeabilities. Another difficulty is very fine discretizations ($N_\Delta \geqslant O(10^4)$ triangular elements per surface) required to sufficiently resolve lubrication effects (especially in the tight squeezing regime) and high-curvature details for drops near breakup. Owing to these severe challenges, the present simulations are for systems of moderate size (up to 36 solid spheres and,

https://doi.org/10.1017/jfm.2013.197 Published online by Cambridge University Press

initially, 100 deformable drops in a periodic cell), with the drops of the same viscosity as the carrier fluid ($\lambda = 1$). Unlike for purely multidrop systems, the case $\lambda = 1$ in the present problem still requires BI iterations (for the Hebeker density on the solids) at each time step, but these iterations are now decoupled from drop–solid interactions; the resulting gain (versus the general case $\lambda \neq 1$) is several-fold and facilitated systematic results reported in this paper.

Using this algorithm, the non-dimensional instantaneous and long-time-averaged velocities (permeabilities) of the drop phase (U_D) and continuous phase (U_C) were studied for initially monodisperse emulsions with drop-to-particle size ratio $\widetilde{a}^o/\widehat{a} \approx 0.51$–$0.52$ and emulsion concentration $c_{em} \approx 0.41$–0.42 in the available space, for flows through many different packings of solid spheres. The velocity scale here is the average single-phase velocity U_{CK} over the interstitial space predicted by the semi-empirical Carman–Kozeny correlation for individual packings. The capillary number $\boldsymbol{Ca} = (\mu U_{CK}/\sigma)(\widetilde{a}^o/\widehat{a})$ is based on the viscosity μ, surface tension σ and initial size ratio $\widetilde{a}^o/\widehat{a}$; a constant average pressure gradient is assumed.

In the tight-squeezing regime with $\boldsymbol{Ca} \sim 0.006$, the drops travel with high resistance and only modest deformation; no breakups are observed. This case, though, is particularly difficult because of large drop-phase velocity fluctuations, necessitating very large simulation times for averaging, and because of stringent, high-resolution requirements for the particle surfaces. Upon convergence, the average drop-phase and continuous-phase velocities are found to be practically independent from the initial drop locations inside the granular material. In this range, with $\boldsymbol{Ca} \sim 0.006$, the average drop-phase velocity is typically comparable with that of the continuous phase.

Drop breakups are still not observed for $\boldsymbol{Ca} = 0.009$ and only rare, isolated breakups are encountered for $\boldsymbol{Ca} = 0.012$–0.015. In contrast, for $\boldsymbol{Ca} = 0.02$, the emulsion drops are prone to frequent fragmentation; some runs with $\widehat{N} = 18$ granular particles and initially $\widetilde{N} = 50$ drops in a periodic cell were continued to observe ~60 primary and secondary breakups, the fragmentation process still being far from over in these runs. Most interestingly and unexpectedly, the drop-phase and continuous-phase velocities approach the statistical steady state much faster, so that only an initial, relatively small portion of breakups needs to be simulated to obtain the average phase permeabilities, which is a great simplification. For different initial drop configurations inside the granular material, the subsequent histories of drop breakup are entirely different; however, this difference in the initial conditions was found to have no appreciable effect on the steady-state phase velocities. While our methodology successfully predicts the steady-state phase velocities based on the initial drop size $\widetilde{a}^o$ (through the capillary number $\boldsymbol{Ca}$ and size ratio), it would be unproductive, instead, to try correlating these velocities with the true steady-state, hard-to-obtain size distribution; such correlation would likely involve an unlimited number of parameters due to polydispersity of the final state. For large enough $\boldsymbol{Ca}$, the long-time behaviour is expected to become insensitive to the initial drop size $\widetilde{a}^o$, once virtually all of the drops break repeatedly to the critical sizes, with no further fragmentation. In this regime, $\mu U_{CK}/\sigma$ would be a substantial controlling parameter, to replace $\boldsymbol{Ca}$ and size ratio $\widetilde{a}^o/\widehat{a}$. However, our simulations, even with massive breakup, still do not approach this limit.

Using the Carman–Kozeny velocity scale U_{CK}, with its sensitivity to the particle volume fraction of individual packings, for non-dimensionalization is very important to reduce the dispersion of the results for different realizations of a granular material. However, the non-dimensional time-averaged phase velocities (especially U_D) are

https://doi.org/10.1017/jfm.2013.197 Published online by Cambridge University Press

still strongly dependent on individual packings, so additional ensemble averaging is imperative for meaningful results. Our phase velocities, averaged over ∼10 packings for each system size, do not show any strong effects of the number of particles and drops used in the simulations, and they clearly demonstrate the physical trends with the variation of the capillary number. Strongly deformable drops ($\boldsymbol{Ca} = 0.02$) move, on average, much faster than does the continuous phase. As $\boldsymbol{Ca}$ is reduced, though, this trend is quickly reversed, and the average drop-phase velocity approaches that of the continuous phase. Our results point to the existence of the critical capillary number $\boldsymbol{Ca}_{crit}$ (believed to be 0.003–0.004, independent of the system size) at which the drop-phase flow effectively stops due to drop blockage in the pores by capillary forces. No such threshold exists for the carrier fluid, since it still has room to flow around the drops when the latter are trapped. The fact that the drops do not move slower than the continuous phase until $\boldsymbol{Ca}_{crit}$ is closely approached is likely due to matching viscosities ($\lambda = 1$) in the present simulations. Reliable simulations near $\boldsymbol{Ca}_{crit}$, though, would be prohibitive in the present problem due to severe convergence difficulties.

To probe the effects of the emulsion concentration, we compared the flow of a concentrated ($c_{em} = 43\,\%$) and very dilute ($c_{em} = 0.43\,\%$) emulsions through one packing of 36 spheres in a periodic box, at the same drop-to-particle size ratio $\widetilde{a}^o/\widehat{a} \approx 0.51$ and capillary numbers. The dilute case is simply achieved using one drop in a periodic box. The first deep distinction is that the system trajectory is stochastic for the concentrated emulsion, while the single-drop motion quickly attains a time-periodic regime, with the drop moving in a narrow, slightly curved periodic channel ('optimal path') roughly along the average pressure antigradient. This periodic regime and the optimal path are found to be independent of the initial drop location. Second, solitary drops travelling through a RLP are much less prone to breakup than the concentrated emulsion drops: even for $\boldsymbol{Ca} = 0.02$, only an insignificant breakup, with a tiny satellite formation, was observed for a single drop, while the concentrated emulsion drops are subject to massive fragmentation at this capillary number. The average permeability of solitary drops is a weak function of $\boldsymbol{Ca}$ and is, at least, several times larger than the concentrated emulsion permeability. Finally, single deformable drops with size ratio $\widetilde{a}^o/\widehat{a} = 0.51$ are found to travel much more efficiently than small drops ($\widetilde{a}^o/\widehat{a} = 0.26$) do. Although the single-drop periodic regime is clearly an artifact due to periodic boundary conditions imposed on a random particle packing, it makes sense as an approximation for time averaging in much larger particle packings, where the drop motion would be truly stochastic. Of course, in beds of small-to-moderate size, time averaging must be complemented by ensemble averaging for more accurate results, which we have not yet attempted for single-drop motion.

In future work, we expect being able to explore single-drop motion through a randomly packed granular material in much greater detail. Obviously, when a single drop is surrounded by a large number of solid particles, the BI solution (Hebeker density) in the solid nodes needs to be iterated every time step only in the vicinity of the drop, and less frequently for other solid nodes. Although a correct and efficient implementation of this principle is non-trivial and was not included in the present work, it is expected to additionally speed up simulations, at least several fold, and would allow for larger particle packings to be considered. The $\lambda = 1$ restriction can be lifted at almost no extra cost in this case. It will also be intriguing to explore the effects of the particle packing type (RLP versus RCP) on drop migration through a granular material.

https://doi.org/10.1017/jfm.2013.197 Published online by Cambridge University Press

Acknowledgements

This work was supported by NSF Grant No. CBET 1064132.

Appendix A. Improved integration schemes over a spherical surface with unstructured triangulation

To simplify the notation, and without a loss of generality, we assume here that the sphere S has the unit radius and is centred at the global coordinate origin $\boldsymbol{O}$. Consider a geodesic mesh triangle $\Delta_{sph} \in S$ with vertices $\boldsymbol{x}^{i_1}$, $\boldsymbol{x}^{i_2}$, $\boldsymbol{x}^{i_3}$ and the right orientation; the path $(\boldsymbol{x}^{i_1}, \boldsymbol{x}^{i_2}, \boldsymbol{x}^{i_3}, \boldsymbol{x}^{i_1})$ is seen clockwise from the origin $\boldsymbol{O}$; each side of the triangle is an arc of a circumference centred at $\boldsymbol{O}$. The centre $\overline{\boldsymbol{x}} \in S$ of the triangle Δ_{sph} is defined by the unit director of $\boldsymbol{x}^{i_1} + \boldsymbol{x}^{i_2} + \boldsymbol{x}^{i_3}$. Let (x', y', z') be a local coordinate system centred at $\overline{\boldsymbol{x}}$, with the z'-axis along $\overline{\boldsymbol{x}}$ and x', y' in the plane tangent to the sphere S at $\overline{\boldsymbol{x}}$; $\boldsymbol{e}'_1$ and $\boldsymbol{e}'_2$ are the basis vectors of x' and y' axes, respectively; this coordinate system is defined to within an arbitrary rotation about $\overline{\boldsymbol{x}}$.

The integrand $\varphi(\boldsymbol{x})$ is approximated within Δ_{sph} as a linear function $Ax' + By' + C$ fitting $\varphi(\boldsymbol{x})$ in the vertices, which yields

$$\begin{pmatrix} A \\ B \\ C \end{pmatrix} = T \begin{pmatrix} \varphi(\boldsymbol{x}^{i_1}) \\ \varphi(\boldsymbol{x}^{i_2}) \\ \varphi(\boldsymbol{x}^{i_3}) \end{pmatrix}, \quad T = \begin{pmatrix} (x^{i_1})' & (y^{i_1})' & 1 \\ (x^{i_2})' & (y^{i_2})' & 1 \\ (x^{i_3})' & (y^{i_3})' & 1 \end{pmatrix}^{-1}. \tag{A 1}$$

The linear form, conveniently written as $\boldsymbol{n} \cdot (A\boldsymbol{e}'_1 + B\boldsymbol{e}'_2) + C$, where $\boldsymbol{n}(\boldsymbol{x}) = \boldsymbol{x}$ is the outward unit normal on S, is integrated exactly over Δ_{sph} using

$$S_\Delta^{sph} = \int_{\Delta_{sph}} \mathrm{d}S = \alpha + \beta + \gamma - \pi \tag{A 2}$$

and

$$\boldsymbol{P} = \int_{\Delta_{\mathrm{sph}}} \boldsymbol{n}\, \mathrm{d}S = \sum_{k=1}^{3} \frac{1}{2} \frac{\psi_k}{\sin \psi_k} (\boldsymbol{x}^{i_k} \times \boldsymbol{x}^{i_{k+1}}). \tag{A 3}$$

In (A 2), the right-hand side is the well-known expression for the spherical triangle area through the sum $\alpha + \beta + \gamma$ of its internal angles. In (A 3), ψ_k is the angle between the vectors $\boldsymbol{x}^{i_k}$ and $\boldsymbol{x}^{i_{k+1}}$; i_4 is identified with i_1. An easy way to derive (A 3) is to integrate instead over the side surface of the body angle $\boldsymbol{O}\boldsymbol{x}^{i_1}\boldsymbol{x}^{i_2}\boldsymbol{x}^{i_3}$, with the minus sign. Introducing the array $m_1 = \boldsymbol{P} \cdot \boldsymbol{e}'_1$, $m_2 = \boldsymbol{P} \cdot \boldsymbol{e}'_2$, $m_3 = S_\Delta^{sph}$, the mesh triangle contribution is approximated as

$$\int_{\Delta_{sph}} \varphi(\boldsymbol{x})\, \mathrm{d}S \approx \sum_{j=1}^{3} \sum_{k=1}^{3} m_j T_{jk} \varphi(\boldsymbol{x}^{i_k}), \tag{A 4}$$

the result being independent of arbitrary rotation of axes x', y' around $\overline{\boldsymbol{x}}$. Summing up all contributions (A 4) yields an economical form (2.11), with reassignment of triangle contributions to vertices; obviously, the area elements ΔS_j are calculated once for the entire simulation.

We have also tested an alternative, high-order integration scheme, when $\varphi(\boldsymbol{x})$ is approximated as a quadratic function of x', y' within Δ_{sph}, fitting the values of φ in the triangle vertices $\boldsymbol{x}^{i_1}$, $\boldsymbol{x}^{i_2}$, $\boldsymbol{x}^{i_3}$ and three more mesh vertices around Δ_{sph}. In addition to (A 2) and (A 3), the diadic $\boldsymbol{nn}$ needs to be integrated over Δ_{sph}, which can still be

https://doi.org/10.1017/jfm.2013.197 Published online by Cambridge University Press

done analytically using the Gauss theorem and integrating instead over the side surface of the body angle. This approach yields another quadrature of the type (2.11), with superb accuracy for general smooth functions $\varphi(\boldsymbol{x})$, but had to be abandoned in the present problem as less robust.

Appendix B. RLP algorithm

We seek a random, isotropic mechanically equilibrium contact network of $N \gg 1$ absolutely rigid, cohesionless spheres S_α of radius a with centres $\boldsymbol{x}^1, \ldots, \boldsymbol{x}^N$ in the box $[0, 1)^3$ and triply periodic continuation into all space with periods 1, 1, 1. In the case of frictionless particles, the purely geometrical RCP algorithm of Zinchenko (1994) acts as follows. Let the system initially form a network with $3N - 3$ independent contacts (and each sphere having at least three neighbours). Let $\boldsymbol{x}_{\alpha\beta} = \boldsymbol{x}^\beta - \boldsymbol{x}^\alpha + \boldsymbol{k}_{\alpha\beta}$ be the 'minimal vector' drawn from $\boldsymbol{x}^\alpha = (x^\alpha,\ y^\alpha,\ z^\alpha)$ to the centre of the periodic image of S_β nearest to $\boldsymbol{x}^\alpha$, with a suitable integer displacement $\boldsymbol{k}_{\alpha\beta}$. The geometric relations $\boldsymbol{x}_{\alpha\beta}^2 = (2a)^2$ for all independent contact pairs $(\alpha_k, \beta_k)(k = 1, 2, \ldots, 3N-3)$ form $3N-3$ nonlinear equations for $3N$ unknowns x^α, y^α, z^α and, in principle, determine the positions $\boldsymbol{x}^\alpha$ as unique functions of the radius a, to within an insignificant translation of the whole network. Differentiation of these geometric constraints yields a system of differential equations of densification

$$\frac{\mathrm{d}\boldsymbol{x}^\alpha}{\mathrm{d}a} = \boldsymbol{V}_\alpha(\boldsymbol{x}^1, \ldots, \boldsymbol{x}^N, a), \tag{B 1}$$

with $\boldsymbol{V}_\alpha$ determined from $\boldsymbol{x}_{\alpha_k,\beta_k} \cdot (\boldsymbol{V}_{\beta_k} - \boldsymbol{V}_{\alpha_k}) = 4a$ (to within an additive constant). This system is solved numerically, thus allowing the spheres to swell while keeping all of the existing contacts, until a new contact $k = 3N - 2$ occurs. At this moment, adding the new contact constraint makes the system for $\boldsymbol{V}_\alpha$ overdetermined, so one of the existing bonds $k = k^* \leqslant 3N - 3$ has to be broken to continue densification. The bond exclusion rule in Zinchenko (1994) is to first calculate the extremal point $(\boldsymbol{V}_1^*, \ldots, \boldsymbol{V}_N^*)$, which minimizes the function

$$F(\boldsymbol{V}_1, \ldots, \boldsymbol{V}_N) = \sum_{k=1}^{3N-2} [\boldsymbol{x}_{\alpha_k,\beta_k} \cdot (\boldsymbol{V}_{\beta_k} - \boldsymbol{V}_{\alpha_k}) - 4a]^2 \tag{B 2}$$

through the solution of the linear system

$$\sum_{\beta \in \mathscr{A}_\alpha} [4a - \boldsymbol{x}_{\alpha\beta} \cdot (\boldsymbol{V}_\beta^* - \boldsymbol{V}_\alpha^*)]\boldsymbol{x}_{\alpha\beta} = 0, \quad \alpha = 1, 2, \ldots, N \tag{B 3}$$

(where $\mathscr{A}_\alpha$ is the set of neighbours in contact with particle S_α in the triply periodic network). The bond $k = k^*$ to exclude is the one with maximum $\boldsymbol{x}_{\alpha_k,\beta_k} \cdot (\boldsymbol{V}_{\beta_k}^* - \boldsymbol{V}_{\alpha_k}^*)$. Note that (B 3) curiously have the form of mechanical balances for each particle under the action of normal contact forces $N_{\alpha\beta} \sim 4a - \boldsymbol{x}_{\alpha\beta} \cdot (\boldsymbol{V}_\beta^* - \boldsymbol{V}_\alpha^*)$, so the bond exclusion rule above simply eliminates the contact with the most negative reaction $N_{\alpha\beta}$. It was rigorously proved (Zinchenko 1994) that excluding the bond $k = k^*$, with the new contact $k = 3N - 2$ added, does result in separation $(\boldsymbol{x}_{\alpha_k,\beta_k} \cdot (\boldsymbol{V}_{\beta_k} - \boldsymbol{V}_{\alpha_k}) > 4a)$ of the contact $k = k^*$, so densification can be continued until the new contact occurs and so on. The algorithm terminates when, upon a new contact formation, there are no negative (i.e. unphysical) contact forces $4a - \boldsymbol{x}_{\alpha\beta} \cdot (\boldsymbol{V}_\beta^* - \boldsymbol{V}_\alpha^*)$. A modification of this scheme is used to generate an initial network with $3N - 3$ independent contacts from a random dilute configuration of non-touching spheres. At this stage, the system

https://doi.org/10.1017/jfm.2013.197 Published online by Cambridge University Press

of equations for $\boldsymbol{V}_\alpha$ is underdetermined, and some randomness is introduced into the solution, but different strategies do not lead to appreciably different results for the final RCP state. This algorithm is essentially 'static' (i.e. containing no densification rate) and gave results in excellent agreement with experimental data, both for the packing density and structure (Zinchenko 1994).

Generalization of this approach for the opposite case of absolutely rough, rigid spheres is non-trivial. We also start from a low-concentration random system of non-touching spheres with volume fraction c_o (prepared by the Monte Carlo method), but, in densification, we additionally seek to retain no-slip between contacting pairs (α_k, β_k), so the algorithm operates with both translational and rotational displacements. Let the surface points $\boldsymbol{x} \in S_\alpha$ undergo a displacement $[\boldsymbol{V}_\alpha + 2\boldsymbol{\Omega}_\alpha \times (\boldsymbol{x} - \boldsymbol{x}^\alpha)]\Delta a$ in the densification interval $(a, a + \Delta a)$. No-slip for the contact pairs (α_k, β_k) requires

$$\boldsymbol{V}_{\beta_k} - \boldsymbol{V}_{\alpha_k} - (\boldsymbol{\Omega}_{\alpha_k} + \boldsymbol{\Omega}_{\beta_k}) \times \boldsymbol{x}_{\alpha_k,\beta_k} = 2\boldsymbol{n}_{\alpha_k,\beta_k} \tag{B 4}$$

(where $\boldsymbol{n}_{\alpha\beta}$ is the unit director of $\boldsymbol{x}_{\alpha\beta}$), which constitutes a system of equations for $\boldsymbol{V}_1, \ldots, \boldsymbol{V}_N$ and $\boldsymbol{\Omega}_1, \ldots, \boldsymbol{\Omega}_N$ to solve at each densification step and then advance the particle centres $\boldsymbol{x}^\alpha$ to the new positions $\boldsymbol{x}^\alpha + \boldsymbol{V}_\alpha \Delta a$, with the new sphere radius $a + \Delta a$. The system (B 4) is solved by CG iterations. An initial approximation is chosen randomly (which has an effect on the early densification stage with a small number $M \ll 2N$ of independent contacts, when the system (B 4) is strongly underdetermined, but no significant effect on the statistics of the final RLP configurations). When a new contact $(\alpha_{M+1}, \beta_{M+1})$ occurs, we first solve the minimization problem for the function

$$F(\boldsymbol{V}_1, \ldots, \boldsymbol{V}_N, \boldsymbol{\Omega}_1, \ldots, \boldsymbol{\Omega}_N) = \sum_{k=1}^{M+1} \left[\boldsymbol{V}_{\beta_k} - \boldsymbol{V}_{\alpha_k} - (\boldsymbol{\Omega}_{\alpha_k} + \boldsymbol{\Omega}_{\beta_k}) \times \boldsymbol{x}_{\alpha_k,\beta_k} - 2\boldsymbol{n}_{\alpha_k,\beta_k}\right]^2 \to \min \tag{B 5}$$

by CG iterations. If $\min F = 0$, all of the (B 4) are still satisfied, and densification (B 1) is continued until the new contact occurs. If, however, $\min F \neq 0$, the solution of (B 5) provides non-trivial mechanical force and torque balances $\partial F/\partial \boldsymbol{V}_\alpha = \partial F/\partial \boldsymbol{\Omega}_\alpha = 0$ for each particle, namely,

$$\sum_{\beta \in \mathscr{A}_\alpha} \boldsymbol{F}_{\alpha\beta} = 0, \quad \sum_{\beta \in \mathscr{A}_\alpha} \boldsymbol{x}_{\alpha\beta} \times \boldsymbol{F}_{\alpha\beta} = 0, \tag{B 6}$$

with 'contact forces'

$$\boldsymbol{F}_{\alpha\beta} = \boldsymbol{V}_\beta - \boldsymbol{V}_\alpha - (\boldsymbol{\Omega}_\alpha + \boldsymbol{\Omega}_\beta) \times \boldsymbol{x}_{\alpha\beta} - 2\boldsymbol{n}_{\alpha\beta}. \tag{B 7}$$

In this case, the algorithm strategy to continue densification consists of several successive stages done recursively, when necessary.

(*a*) Define all bonds (α_k, β_k), $k \leqslant M + 1$ either as non-slippery (denoted $k \in \mathscr{B}_{ns}$) for non-negative normal reactions $4a - \boldsymbol{x}_{\alpha_k,\beta_k} \cdot (\boldsymbol{V}_{\beta_k} - \boldsymbol{V}_{\alpha_k})$, or as slippery ($k \in \mathscr{B}_s$) otherwise.

(*b*) Solve the minimization problem for $F_1(\boldsymbol{V}_1, \ldots, \boldsymbol{V}_N, \boldsymbol{\Omega}_1, \ldots, \boldsymbol{\Omega}_N)$:

$$F_1 = \sum_{k \in \mathscr{B}_{ns}} [\boldsymbol{V}_{\beta_k} - \boldsymbol{V}_{\alpha_k} - (\boldsymbol{\Omega}_{\alpha_k} + \boldsymbol{\Omega}_{\beta_k}) \times \boldsymbol{x}_{\alpha_k,\beta_k} - 2\boldsymbol{n}_{\alpha_k,\beta_k}]^2 + \sum_{k \in \mathscr{B}_s} [(\boldsymbol{V}_{\beta_k} - \boldsymbol{V}_{\alpha_k}) \cdot \boldsymbol{n}_{\alpha_k,\beta_k} - 2]^2 \to \min. \tag{B 8}$$

https://doi.org/10.1017/jfm.2013.197 Published online by Cambridge University Press

(*c*) If $\min F_1 = 0$, use the solution of (B 8) to continue densification $\boldsymbol{x}^{\alpha}_{\rm new} = \boldsymbol{x}^{\alpha} + \boldsymbol{V}^{\alpha}\Delta a$.

(*d*) If $\min F_1 \neq 0$, find a bond $k = k^* \leqslant M$ to be removed. To this end, search through all contact pairs (α_k, β_k), $k \leqslant M$, with particles α_k and β_k each having, at least, four neighbours, and find the bond $k = k^*$ with the most negative normal reaction $2 - (\boldsymbol{V}_{\beta_k} - \boldsymbol{V}_{\alpha_k}) \cdot \boldsymbol{n}_{\alpha_k,\beta_k}$ among such pairs. In rare cases, such a bond does not exist until one or two recursions of steps (*a*)–(*d*) are made.

(*e*) With the bond $k = k^*$ removed and the total number of contacts updated ($M \to M - 1$), return to (*a*). Usually, one recursion is enough to get $\min F_1 = 0$.

Note that the exit from these stages at (*c*) provides the slippery and non-slippery bonds, and the minimizing function (B 8) for all further densification, until a new contact $k = M + 1$ is detected. At that moment, all bonds (α_k, β_k) are declared non-slippery, and we return to minimization (B 5). The algorithm terminates when there are no negative normal reactions $2 - (\boldsymbol{V}_{\beta_k} - \boldsymbol{V}_{\alpha_k}) \cdot \boldsymbol{n}_{\alpha_k,\beta_k}$ in (B 6) and (B 7), or (more often) in the non-trivial mechanical balances $\partial F_1/\partial \boldsymbol{V}_{\alpha} = \partial F_1/\partial \boldsymbol{\Omega}_{\alpha} = 0$. It is important to emphasize that there are no slippery contacts in this final RLP state, but, instead, a very small portion of unloaded contacts ($\boldsymbol{F}_{\alpha\beta} = \boldsymbol{0}$). Once the number of contacts approaches $2N$ in the course of densification, it stays very close to this value until RLP is reached. So, introduction of slippery contacts at the intermediate stage is a purely technical tool allowing *rough* particles to reach perfect mechanical equilibrium, and should not be viewed as shifting the results toward RCP (where the number of contacts is $\approx 3N$). Except in exclusive cases, each particle has, at least, three contacting neighbours in our RLP configurations, due to the requirements in step (*d*).

Technical implementation of this basic version of the algorithm, suitable for small-to-moderate systems ($N \leqslant O(100)$) is simple, but requires some caution. The choice of a variable densification step Δa follows Zinchenko (1994), so does the detection of new contacts in the Euler stepping scheme through the solution of a quadratic equation. It is normal that the contact pairs (α_k, β_k) become (very slightly) non-touching in the course of densification, and should still be regarded as bonded. On the other hand, to exclude the (very rare) possibility of numerical overlapping between bonded particles, it helps to introduce a perturbation in (B 5) and (B 7) and (B 8), replacing 2 with $\Lambda_k = \delta + 4a/|\boldsymbol{x}_{\alpha_k,\beta_k}| \approx 2$; typically, $\delta \sim 10^{-7}$–10^{-8}. The densification equations are solved with compatible accuracy

$$\begin{aligned} &|\boldsymbol{V}_{\beta_k} - \boldsymbol{V}_{\alpha_k} - (\boldsymbol{\Omega}_{\alpha_k} + \boldsymbol{\Omega}_{\beta_k}) \times \boldsymbol{x}_{\alpha_k,\beta_k} - \Lambda_k \boldsymbol{n}_{\alpha_k,\beta_k}| < \delta \quad \text{for } k \in \mathscr{B}_{ns}, \\ &|(\boldsymbol{V}_{\beta_k} - \boldsymbol{V}_{\alpha_k}) \cdot \boldsymbol{n}_{\alpha_k,\beta_k} - \Lambda_k| < \delta \quad \text{for } k \in \mathscr{B}_{s}, \end{aligned} \tag{B 9}$$

unless it is detected in the course of CG iterations that the corresponding function F (or F_1) has a pronounced non-zero minimum. Unlike for RCP (Zinchenko 1994), we do not have a rigorous mathematical theory for this RLP algorithm. Removal of the bond $k = k^*$ in step (d)) usually results in subsequent separation of the contact pair $(\alpha_{k^*}, \beta_{k^*})$, but not always. A successful empirical remedy is to limit the search of bonds in step (d)) by an additional constraint $|\boldsymbol{x}_{\alpha_k,\beta_k}|/(2a) > 1 + O(10^{-14}$–$10^{-15})$; the precise threshold here is unimportant. Such a threshold precludes a pair of particles reattached after an unsuccessful separation from immediate subsequent separation and the process takes a different trajectory. With these modifications, the algorithm is reliable and was used to generate 200 RLP configurations with $N = 50$ or 100 from different initial random packings of non-touching spheres with density $c_o = 0.15$ (§ 5). In just a few runs, the algorithm stalled, but it was always possible to complete the RLP generation by slightly varying the δ parameter.

https://doi.org/10.1017/jfm.2013.197 Published online by Cambridge University Press

The algorithm performance severely degrades, if it meets a 'singular point', with abnormally high values for some vectors $\boldsymbol{V}_\alpha$, resulting in extremely small densification steps Δa. The same difficulty was observed for the RCP algorithm (Zinchenko 1994) but not resolved. A successful remedy found here is simple. If a large number (100) of densification steps Δa do not result in a new contact and $\max|\boldsymbol{V}_\alpha|$ reaches abnormally high values ($\geqslant 10^5$), then we find the closest pair (α, β) among unbonded particles and add it to the list of contact pairs (α_k, β_k); even though S_α, S_β are non-touching, in practice they are extremely close in this operation. This remedy, applied in exclusive cases only, does not have a statistical effect on the final RCP configurations, but introduces a sufficient perturbation to the contact network to return $|\boldsymbol{V}_\alpha|$ to normal values $\sim 10^2$–10^3.

REFERENCES

BAZHLEKOV, I. B., ANDERSON, P. D. & MEIJER, H. E. H. 2004 Nonsingular boundary integral method for deformable drops in viscous flows. *Phys. Fluids* **16**, 1064–1081.

CHHABRA, R. P. & SRINIVAS, B. K. 1991 Non-Newtonian (purely viscous) fluid flow through packed beds: effect of particle shape. *Powder Tech.* **67**, 15–19.

CHAPMAN, A. M. & HIGDON, J. J. L. 1992 Oscillatory Stokes flow in periodic porous media. *Phys. Fluids* A **4**, 2099–2116.

COBOS, S., CARVALHO, M. S. & ALVARADO, V. 2009 Flow of oil–water emulsions through a constricted capillary. *Intl J. Multiphase Flow* **35**, 507–515.

CRISTINI, V., BŁAWZDZIEWICZ, J. & LOEWENBERG, M. 1998 Drop breakup in three-dimensional viscous flows. *Phys. Fluids* **10**, 1781–1783.

CRISTINI, V., BŁAWZDZIEWICZ, J. & LOEWENBERG, M. 2001 An adaptive mesh algorithm for evolving surfaces: simulations of drop breakup and coalescence. *J. Comput. Phys.* **168**, 445–463.

CRISTINI, V., BŁAWZDZIEWICZ, J., LOEWENBERG, M. & COLLINS, L. R. 2003 Breakup in stochastic Stokes flows: sub-Kolmogorov drops in isotropic turbulence. *J. Fluid Mech.* **492**, 231–250.

DUPIN, M. M., HALLIDAY, I., CARE, C. M., ALBOUL, L. & MUNN, L. L. 2007 Modelling the flow of dense suspensions of deformable particles in three dimensions. *Phys. Rev.* E **75**, 066707.

EGGERS, J. 1997 Nonlinear dynamics and breakup of free-surface flows. *Rev. Mod. Phys.* **69**, 865–929.

FARRELL, G. R., MARTINI, K. M. & MENON, N. 2010 Loose packings of frictional spheres. *Soft Matt.* **6**, 2925–2930.

GRAHAM, D. R. & HIGDON, J. J. L. 2000*a* Oscillatory flow of droplets in capillary tubes. Part 1. Straight tubes. *J. Fluid Mech.* **425**, 31–53.

GRAHAM, D. R. & HIGDON, J. J. L. 2000*b* Oscillatory flow of droplets in capillary tubes. Part 2. Constricted tubes. *J. Fluid Mech.* **425**, 55–77.

GUILLEN, V R., CARVALHO, M. S. & ALVARADO, V. 2012 Pore scale and macroscopic displacement mechanisms in emulsion flooding. *Transp. Porous Med.* **94**, 197–206.

HASIMOTO, H. 1959 On the periodic fundamental solutions of the Stokes equations and their application to viscous flow past a cubic array of spheres. *J. Fluid Mech.* **5**, 317–328.

HEBEKER, F.-K. 1986 Efficient boundary element methods for three-dimensional exterior viscous flow. *Numer. Meth. PDE* **2**, 273–297.

HERNÁNDEZ-ORTIZ, J. P., DE PABLO, J. J. & GRAHAM, M. D. 2007 Fast computation of many-particle hydrodynamic and electrostatic interactions in a confined geometry. *Phys. Rev. Lett.* **98**, 140602.

HOCKNEY, R. W. & EASTWOOD, J. W. 1981 *Computer Simulation Using Particles*. McGraw-Hill.

JAISWAL, A. K., SUNDARARAJAN, T. & CHHABRA, R. P. 1993 Slow non-Newtonian flow through packed beds: effect of zero shear viscosity. *Can. J. Chem. Engng* **71**, 646–651.

https://doi.org/10.1017/jfm.2013.197 Published online by Cambridge University Press

KIM, S. & KARILLA, S. 1991 *Microhydrodynamics: Principles and Selected Aplications*. Butterworth-Heinemann.

KOZICKI, W. 2001 Viscoeleastic flow in packed beds or porous media. *Can. J. Chem. Eng.* **79**, 124–131.

LADD, A. J. C. 1990 Hydrodynamic transport coefficients of random dispersions of hard spheres. *J. Chem. Phys.* **93**, 3484–3494.

LOEWENBERG, M. 1998 Numerical simulation of concentrated emulsion flows. *Trans. ASME: J. Fluids Engng* **120**, 824–832.

LOEWENBERG, M. & HINCH, E. J. 1996 Numerical simulation of a concentrated emulsion in shear flow. *J. Fluid Mech.* **321**, 395–419.

MACMECCAN, R. M., CLAUSEN, J. R., NEITZEL, G. P. & AIDUN, C. K. 2009 Simulating deformable particle suspensions using a coupled lattice–Boltzmann and finite-element method. *J. Fluid Mech.* **618**, 13–39.

MO, G. & SANGANI, A. S. 1994 A method for computing Stokes flow interactions among spherical objects and its application to suspensions of drops and porous particles. *Phys. Fluids* **6**, 1637–1652.

NEMER, M. 2003 Near-contact motion of liquid drops in emulsions and foams. PhD thesis, Yale University, USA.

NEMER, M. B., CHEN, X., PAPADOPOULOS, D. H., BŁAWZDZIEWICZ, J. & LOEWENBERG, M. 2004 Hindered and enhanced coalescence of drops in Stokes flow. *Phys. Rev. Lett.* **92**, 114501.

ONODA, G. Y. & LINIGER, E. G. 1990 Random loose packings of uniform sheres and the dilatancy onset. *Phys. Rev. Lett.* **64**, 2727–2730.

PIRI, M. & BLUNT, M. J. 2005 Three-dimensional mixed-wet random pore-scale network modelling of two- and three-phase flow in porous media. I. Model description. *Phys. Rev.* E **71**, 026301.

POWER, H. & MIRANDA, G. 1987 Second kind integral equation formulation of Stokes flow past a particle of arbitrary shape. *SIAM J. Appl. Maths* **47**, 689–698.

PRANAY, P., HENRÍQUEZ-RIVERA, R. G. & GRAHAM, M. D. 2012 Depletion layer formation in suspensions of elastic capsules in Newtonian and viscoelastic fluids. *Phys. Fluids* **24**, 061902.

QUAN, S., LOU, J. & SCHMIDT, D. P. 2009*a* Modelling merging and breakup in the moving mesh interface tracking method for multiphase flow simulations. *J. Comput. Phys.* **228**, 2660–2675.

QUAN, S. & SCHMIDT, D. P. 2007 A moving mesh interface tracking method for three-dimensional incompressible two-phase flows. *J. Comput. Phys.* **221**, 761–780.

QUAN, S., SCHMIDT, D. P., HUA, J. & LOU, J. 2009*b* A numerical study of the relaxation and breakup of an elongated drop in a viscous liquid. *J. Fluid Mech.* **640**, 235–264.

RALLISON, J. M. 1981 A numerical study of the deformation and burst of a viscous drop in general shear flows. *J. Fluid Mech.* **109**, 465–482.

ROMERO, M. I. & CARVALHO, M. S. 2011 Experiments and network model of flow of oil-water emulsion in porous media. *Phys. Rev. E* **84**, 046305.

SANGANI, A. S. & ACRIVOS, A. 1982 Slow flow through a periodic array of spheres. *Intl J. Multiphase Flow* **8**, 343–360.

SANGANI, A. S. & MO, G. 1996 An $O(N)$ algorithm for Stokes and Laplace interactions of particles. *Phys. Fluids* **8**, 1990–2010.

SCOTT, G. D. & KILGOUR, D. M. 1969 The density of random close packing of spheres. *Brit. J. Appl. Phys. Ser. 2* **2**, 863–866.

SECOMB, T. W. 1995 Mechanics of blood flow in the microcirculation. In *Biological Fluid Dynamics* (ed. C. P. Ellington & T. J. Pedley). pp. 305–321.

SEO, J. H., LELE, S. K. & TRYGGVASON, G. 2010 Investigation and modelling of bubble–bubble interaction effect in homogeneous bubbly flows. *Phys. Fluids* **22**, 063302.

SILBERT, L. E. 2010 Jamming of frictional spheres and random loose packing. *Soft Matt.* **6**, 2918–2924.

THOMAS, S., ESMAEELI, A. & TRYGGVASON, G. 2010 Multiscale computations of thin films in multiphase flows. *Intl J. Multiphase Flow* **36**, 71–77.

https://doi.org/10.1017/jfm.2013.197 Published online by Cambridge University Press

THOMPSON, K. E. & FOGLER, H. S. 1997 Modelling flow in disordered packed beds from pore-scale fluid mechanics. *AIChE J.* **43**, 1377–1389.

TORQUATO, S. 2002 *Random Heterogeneous Materials: Microstructure and Macroscopic Properties*. Springer.

TRYGGVASON, G., BUNNER, B., ESMAEELI, A., JURIC, D., AL-RAWAHI, N., TAUBER, W., HAN, J., NAS, S. & JAN, Y.-J. 2001 A front-tracking method for the computations of multiphase flow. *J. Comput. Phys.* **169**, 708–759.

UNVERDI, S. O. & TRYGGVASON, G. 1992 A front-tracking method for viscous, incompressible, multi-fluid flows. *J. Comput. Phys.* **100**, 25–37.

ZHANG, H. P. & MAKSE, H. A. 2005 Jamming transition in emulsions and granular materials. *Phys. Rev.* E **72**, 011301.

ZHU, J. & SATISH, M. G. 1992 Non-Newtonian effects on the drag of creeping flow through packed beds. *Intl J. Multiphase Flow* **18**, 765–777.

ZICK, A. A. & HOMSY, G. M. 1982 Stokes flow through periodic arrays of spheres. *J. Fluid Mech.* **115**, 13–26.

ZINCHENKO, A. Z. 1994 Algorithm for random close packing of spheres with periodic boundary conditions. *J. Comput. Phys.* **114**, 298–307.

ZINCHENKO, A. Z. 1998 Effective conductivity of loaded granular materials by numerical simulation. *Phil. Trans. R. Soc. Lond.* A **356**, 2953–2998.

ZINCHENKO, A. Z. & DAVIS, R. H. 2000 An efficient algorithm for hydrodynamical interaction of many deformable drops. *J. Comput. Phys.* **157**, 539–587.

ZINCHENKO, A. Z. & DAVIS, R. H. 2002 Shear flow of highly concentrated emulsions of deformable drops by numerical simulations. *J. Fluid Mech.* **455**, 21–62.

ZINCHENKO, A. Z. & DAVIS, R. H. 2003 Large-scale simulations of concentrated emulsion flows. *Phil. Trans. R. Soc. Lond.* A **361**, 813–845.

ZINCHENKO, A. Z. & DAVIS, R. H. 2005 A multipole-accelerated algorithm for close interaction of slightly deformable drops. *J. Comput. Phys.* **207**, 695–735.

ZINCHENKO, A. Z. & DAVIS, R. H. 2006 A boundary-integral study of a drop squeezing through interparticle constrictions. *J. Fluid Mech.* **564**, 227–266.

ZINCHENKO, A. Z. & DAVIS, R. H. 2008*a* Algorithm for direct numerical simulation of emulsion flow through a granular material. *J. Comput. Phys.* **227**, 7841–7888.

ZINCHENKO, A. Z. & DAVIS, R. H. 2008*b* Squeezing of a periodic emulsion through a cubic lattice of spheres. *Phys. Fluids* **20**, 040803.

ZINCHENKO, A. Z., ROTHER, M. A. & DAVIS, R. H. 1997 A novel boundary-integral algorithm for viscous interaction of deformable drops. *Phys. Fluids* **9**, 1493–1511.

https://doi.org/10.1017/jfm.2013.197 Published online by Cambridge University Press